Mission-Integrated Synthesis/Design Optimization of Aerospace Systems under Transient Conditions

Peter Carl Weise

Thesis submitted to the Faculty of the
Virginia Polytechnic Institute and State University
in partial fulfillment of the requirements for the degree of

Master of Science
In
Mechanical Engineering

Michael R. von Spakovsky, Chair
Walter F. O'Brien
Alan A. Kornhauser

August 8, 2012
Blacksburg, Virginia

Keywords: surrogate modeling, optimization, design of experiments, aerospace

Mission-Integrated Synthesis/Design Optimization of Aerospace Systems under Transient Conditions

By Peter Carl Weise

Abstract

The equations governing the thermodynamic behavior of a military aircraft have been implemented by the Air Force Research Lab (AFRL) and other Integrated Vehicle Energy Technology Demonstration (INVENT) contributors into a cohesive, adaptable, dynamic aircraft simulation program in Mathworks' Simulink®. The resulting model known as the "Tip-to-tail" model meets the design specifications set forth by the INVENT program. The system consists of six intimately linked subsystems that include a propulsion subsystem (PS), air vehicle subsystem (AVS), robust electrical power subsystem (REPS), high power electric actuation subsystem (HPEAS), advanced power and thermal management subsystem (APTMS), and a fuel thermal management subsystem (FTMS). The model's governing equations are augmented with experimental data and supported by defined physical parameters.

In order to address the problems associated with the additional power and thermal loads for in more electric aircraft (MEA), this research utilizes exergy analysis and mission-integrated synthesis/design optimization to investigate the potential for improvement in tip-to-tail design/performance. Additionally, this thesis describes the development and integration of higher fidelity transient heat exchanger models for use in the tip-to-tail.

Finally, the change in performance due to the integration of new heat exchanger models developed here is presented. Additionally, this thesis discusses the results obtained by performing mission-integrated synthesis/design optimization on the tip-to-tail using heat exchanger design parameters as decision variables. These results show that the performance of the tip-to-thermal management subsystems improves significantly due to the integration of the heat exchanger models. These results also show improvements in vehicle performance due to the mission-integrated optimization.

Acknowledgments

This thesis is an accumulation of the research completed over the past two years, and would assuredly have been impossible if not for the assistance of many people. I would like to thank my advisor, Dr. Michael von Spakovsky, for allowing me to come to Virginia Tech and conduct this research. Many thanks to Dr. Walter O'Brien and Dr. Al Kornhauser for serving on my committee and for the insight they have given. Furthermore, I would like to thank Dr. Rory Roberts and Dr. Mitch Wolff of Wright State University for their guidance and insight regarding the tip-to-tail model, model integration, and Simulink.

Special thanks to Grant Gvozdich for his assistance in the development of the heat exchanger model used in this work, for his tolerance of my occasional ignorance, and for his support and friendship over the past two years.

Thanks to the U.S. Air Force Research Lab and Dr. Kirk Yerkes for sponsoring my work and allowing me to continue it over the past two summers at Wright-Patterson Air Force Base.

I would especially like to thank Dr. David Riggins of the Missouri University of Science and Technology for his support in the implementation of the vehicle exergy balance equation and for his assistance in the augmentation of the balance equation to facilitate the use of an arbitrary reference condition.

Thanks to Christopher Marley, Jonathan Sheldon, Dan Decker, David Woodburn, Tony Camarano, Jayme Carper, Scott Eastbourn and all the other students I interacted with at the air force base for the enlightening conversations and assistance in solving problems.

I have been blessed in that the list of family and friends who have contributed to my success is a long one. Thanks to Jordan Schmitz for his friendship, understanding, and the occasional distractions from work the kept me sane. Thanks to everyone from 8-mile and the Coop for memories and lasting friendship.

Most of all, I would like to thank my parents, Steve and Stephanie, my wife, Jessica, and my brother, Joel, for their unwavering support and love. This work is dedicated to you.

Peter Carl Weise

Table of Contents

List of Figures

List of Tables

Nomenclature

ACA	Air Cooled Avionics
AFRL	Air Force Research Laboratory
AFS-A	Airframe Subsystem - Aerodynamics
AMRAAM	Advanced Medium-Range Air-to-Air Missile
ANOVA	Analysis of Variance
APTMS	Adaptive Power and Thermal Management Subsystem
AVS	Aircraft Vehicle Subsystem Avionics
BCM/BCA	Best Cruise Mach Number/Best Cruise Altitude
CHS	Central hydraulic subsystem
CFD	Computational Fluid Dynamics
DEWS	Directed Energy Weapons Subsystem
DOE	Design of Experiments
DX8	Design Expert 8
ECS	Environmental Control Subsystem
EMA	Electro-mechanical Actuator
EOA	Energy Optimized Aircraft
ES	Electrical subsystem
ESG	Electric Starter Generator
FADEC	Full-authority digital engine controller
FCS	Flight Controls Subsystem
FLS	Fuel Loop Subsystem
FTMS	Fuel Thermal Management Subsystem
HPC	High Pressure Compressor
HPEAS	High Power Electrical Actuation Subsystem
HPS	High Pressure Shaft
HPT	High Pressure Turbine
HPTMS	High Performance Thermal Management Subsystem
ICC	Inverter Converter Controller Unit
ILGO	Iterative Local-Global Optimization

IPP	Integrated Power Package
INVENT	Integrated Vehicle Energy Technology
LCA	Liquid Cooled Avionics
LPS	Low Pressure Shaft
LPT	Low Pressure Turbine
LRS	Long Range Strike
MEA	More Electric Aircraft
MRIP	Modeling Requirements and Implementation Plan
NTU	Number of Thermal Units
OLS	Oil Loop Subsystem
PS	Propulsion Subsystem
PTMSC/ICC	Power and Thermal Management System Controller / Inverter Converter Controller
REPS	Robust Electrical Power Subsystem
SBAO	Surrogate Based Analysis and Optimization
SQP	Sequential Quadratic Programming
SSL	Solid State Laser
TMS	Thermal Management Subsystem
T2T	Tip-to-tail
VC/PAOS	Vapor Compression/Polyalfaolephin Loop Subsystem

List of Symbols

A_c	Cross-sectional area (m^2)
A_s	Surface area (m^2)
b	Plate gap thickness (m)
c_p	Specific heat ($J/kg\text{-}K$)
C_{min}	Minimum heat capacity (J/K)
C_{max}	Maximum heat capacity (J/K)
C^*	Heat capacity ratio
C_D	Drag coefficient
C_L	Lift coefficient
D	Drag force (N)
D_h	Hydraulic diameter (m)
f	Friction factor
$F_{x(flight)}$	Net force in the direction of flight (N)
g	Acceleration of gravity (m/s^2)
G	Mass velocity (kg/m^2s)
H	Fin channel height (m)
h	Mass specific enthalpy (J/kg)
H	Enthalpy (J)
$\dot{H}$	Enthalpy flow rate *(W)*
H^*	Net exergy in and out of the control volume (J)
j	Colburn coefficient
k	Thermal conductivity ($W/m\text{-}K$)
l	Fin strip length (m)
L	Length (m)
L	Lift force (N)
m	Mass (kg)
m_{hx}	Mass of heat exchanger (kg)
m_s	Mass of one side of heat exchanger (kg)
$\dot{m}$	Flow rate (kg/s)
M	Mach number
Ntu	Number of thermal units
Nu	Nusselt number
P	Pressure (Pa)
$P_{Dynamic}$	Dynamic pressure (Pa)
Pr	Prandtl number
Q_{max}	Maximum heat transfer (W)
Re	Reynolds number
s	Fin channel width (m)
S_{wing}	Wing planform area (m^2)
$\dot{S}_{gen}$	Entropy generation rate (J/K)
t	Plate thickness (m)
t_f	Fin thickness (m)
T	Thrust (N)
T_{Fluid}	Fluid temperature *(K)*
T_{HX}	Mass temperature *(K)*
T_i	Ambient/inlet temperature (K)
u	Velocity (m/s)
V	Volume (m^3)
V_{hx}	Volume of heat exchanger (m^3)
W	Weight (N)
X	Exergy destruction (J)
$\dot{X}$	Exergy destruction rate (W)

Greek

α	Angle of attack (Deg)
α	Non-dimensional aspect ratio
β	Surface area density (m^2/m^3)
γ	Non-dimensional aspect ratio
δ	Non-dimensional aspect ratio
σ	Porosity (m^3/m^3)
Δh	Change in altitude (m)
Δt	Time step (s)
Δx	Distance traveled (m)
ΔP	Pressure drop
ε	Effectiveness
ν	Dynamic Viscosity (m^2/s)
ρ	Density (kg/m^3)

Chapter 1 - Introduction

The development of advanced sensors, directed energy weapons (DEWs) and electro-mechanical actuators have stimulated research into the feasibility of integrating these technologies into military vehicles. These innovative technologies, while considerably expanding the capabilities of aerospace systems, generate significant power and thermal loads. As future military aircraft, as well as those already in service (through retrofitting), continue to trend towards the design of a more electric aircraft (MEA) [1,2] the need to address the accumulating power and thermal loads becomes critical. Current work by the U.S. Air Force Research Laboratory (AFRL), through the Integrated Vehicle Energy Technology Demonstration (INVENT) Program, is addressing these issues through thermodynamic modeling, simulation, analysis and optimization.

The equations governing the thermodynamic behavior of a military aircraft have been implemented by the AFRL and other INVENT contributors into a cohesive, adaptable, dynamic aircraft simulation program in Mathwork's Simulink®.[3] The resulting model known as the "Tip-to-tail" model meets the design specifications set forth by the INVENT program. The system consists of six intimately linked subsystems that include a propulsion subsystem (PS), air vehicle subsystem (AVS), robust electrical power subsystem (REPS), high power electric actuation subsystem (HPEAS), advanced power & thermal management subsystem (APTMS), and a fuel thermal management subsystem (FTMS). The model's governing equations are augmented with experimental data and supported by defined physical parameters.

To run a flight simulation, the tip-to-tail model requires a mission profile, which includes the instantaneous altitude and Mach number. Using these, the PS and AVS subsystems generate power and thermal loads to meet the performance requirements. The REPS and HPEAS simulate thermal loads from other aircraft components; and as a result of these loads, the APTMS and FTMS accept and reject energy via heat exchangers and heat sinks throughout the aircraft to maintain the necessary operating conditions.

Past work by Gvozdich[4] has shown that the tip-to-tail cannot support a DEW without additions (e.g., phase-change storage) to the FTMS due to large thermal transient effects and thermodynamic inefficiencies. Furthermore, the desire to decrease engine inlet area to reduce

radar signature represents decreased airflow for managing thermal loads. Effectively, the available heat sinks in military aircraft are required to remove more heat with less mass.

Gvozdich[4] has addresses some of these thermal issues. In this research, both exergy analysis and mission-integrated synthesis/design optimization are utilized to investigate the potential for further improvement in tip-to-tail design/performance. As part of this work, this thesis describes the development and integration of higher fidelity transient heat exchanger models for use in tip-to-tail synthesis/design optimization.

1.1 Historical Background

1.1.1 INVENT Program

The United States Air Force Research Lab (AFRL) started the Integrated Vehicle Energy Technology Demonstration (INVENT), tasking it with the mission of "*increasing the war fighting capabilities of existing, evolving, and future aircraft,*" as outlined by the INVENT Modeling Requirements and Implementation Plan (MRIP).[5,a] More specifically, the INVENT program is intended to create a virtual environment in which to model, simulate, analyze, and optimize a high-performance aircraft and deliver a model of an Energy Optimized Aircraft (EOA).[4] As defined by the INVENT program, an EOA "*is an aircraft that is optimized for broad capabilities while maximizing energy utilization (aircraft and ground support) with the minimum complexity system architecture.*"[6,b]

As a first step in this process, the AFRL, Wright State University, and Georgia Tech, in 2010, developed the first version of the thermal tip-to-tail model. This model was unique compared to previous models in that it included fully dynamic thermal models for the entire aircraft. Additionally, the model was non-proprietary, allowing for the distribution of the model to assorted research groups throughout the AFRL, academia, and industry. This model, however, was plagued by painfully slow run times, essentially eliminating the capability of performing any significant trade studies or optimization. Careful examination of the model led to the conclusion that slow simulation run times were a result of the high-fidelity engine model. Work by Wright

[a] This quote is taken from material that is declared a work of the U.S. Government and is not subject to copyright protection in the United States.
[b] This quote is taken from material that is declared a work of the U.S. Government and is not subject to copyright protection in the United States.

State University yielded a replacement engine model that ran significantly faster but without significant losses in fidelity.[7]

The resultant Simulink® model, shown in Figure 1.1, contains six intimately linked subsystems that include a PS (engine), AVS, REPS, HPEAS, APTMS, and FTMS. The model developed by Wright State University and Georgia Tech is termed the thermal tip-to-tail model. This tip-to-tail model contains transient thermodynamic energy balances and heat transfer relationships, supplemented by empirical data. However, electrical loads are simulated using a tabulated, time-dependent load profile. Current work on the development of dynamic generator and actuator models is being done by the INVENT program in collaboration with the University of Central Florida. These electrical models will be combined with the thermal tip-to-tail to create a total tip-to-tail aircraft model.

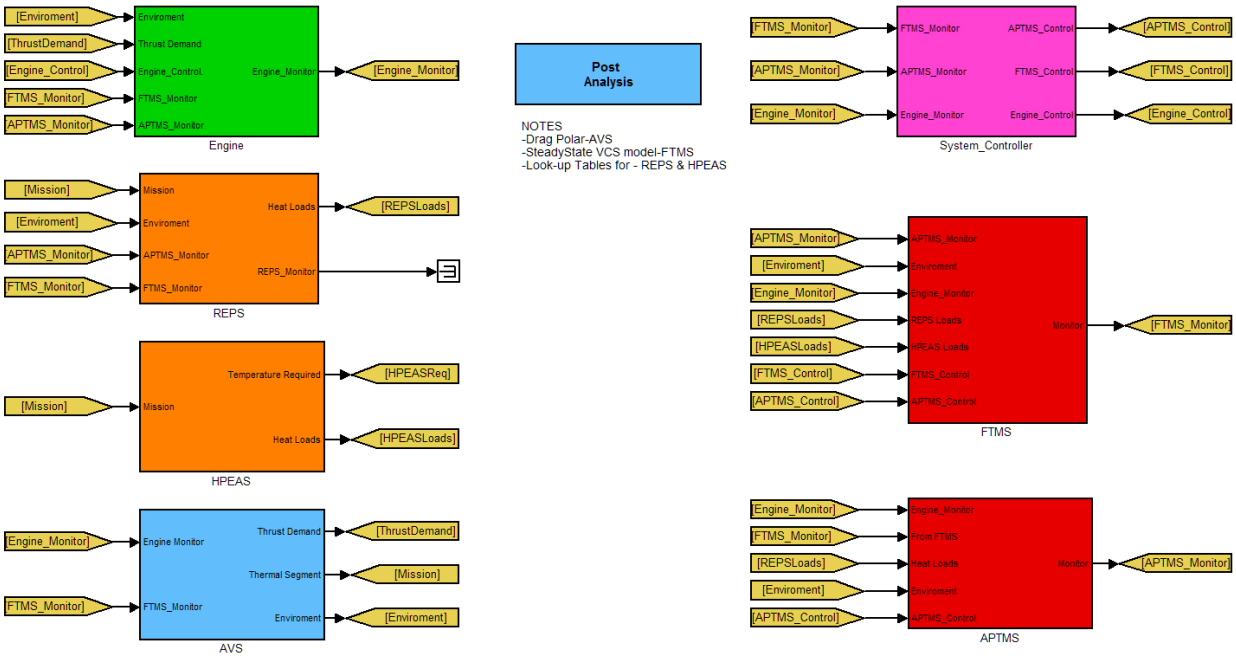

Figure 1.1. Aircraft systems forming the INVENT tip-to-tail model.

The schematic in Figure 1.1 of the subsystems modeled in the tip-to-tail shows that the AVS model accepts inputs of altitude and Mach number and uses this information to calculate a thrust requirement. This thrust requirement gets sent to the system controller, which contains proportional-integral (PI) controllers that vary fuel flow rate to the engine in order to match the thrust requirement.

Many subsystems in the tip-to-tail generate heat loads, including the HPEAS, REPS, directed energy weapons subsystem (DEWS; not shown here but included in the work of Gvozdich[4]), onboard avionics, pumps and compressors. The FTMS and APTMS contain heat exchangers that use fuel, ram or bleed air, and secondary (closed-loop) water or Polyalfaolephin (PAO) loops to manage these loads. Again, the system controller uses PI controllers to manage the flow rates in order to effectively manage heat loads. Many other complex interactions take place in the tip-to-tail that will be explored in further detail in Chapter 3.

1.1.2 More Electric Aircraft

From examination of the past and proposed future designs of military and commercial aircraft, it is clear that aircraft are trending towards the concept of a more electric aircraft (MEA). A MEA is characterized by the electric or electro-mechanical transmission of power as opposed to purely mechanical power transmission. Examples of this trend include the transition from hydraulic governance of aircraft control surfaces to the "fly-by-wire" systems found in most modern aircraft and the use of electric generators driven by jet engine shaft power as opposed to an air turbine driven by bleed air.

In recent decades, the invention and development of advanced sensors, DEWs, electro-mechanical actuators (EMAs), and composite materials has stimulated research into the feasibility of integrating these technologies into military vehicles. As aircraft designers abandon hydraulic systems in favor of EMAs, abandon traditional weapons systems for advanced weapons systems like the DEWS, abandon metallic materials in favor of composites, add advanced sensors for use in reconnaissance and combat, and reduce ram air inlet areas, many thermal management issues arise that are unique to modern aircraft.

Using EMAs instead of hydraulic actuators increases aircraft reliability, simplifies the process of adding redundancy to the aircraft in case of failure, and reduces the weight of the flight actuation system. However, vibrations and transient effects can cause heating within the actuation subsystem and without hydraulic fluid which can be used as a heat sink, an alternative cooling subsystem must be used which adds complexity to the aircraft.

Traditional military aircraft weapons (e.g., missiles and guns) have high reliability and sufficient destructive force for most situations. However, a major drawback to these types of weapons is their inherent lack of precision. Significant advances have been made in recent

decades with the advent of laser guided and heat seeking missiles but these still do not compare to the accuracy attainable with a laser. As such, DEWs are useful in disabling but not destroying enemy vehicles and are often seen as the future of fighting aircraft. Issues with DEWs include weight and size, as well as high inefficiencies producing significant, localized heat loads. A typical solid-state (SSL) laser will peak at an efficiency of 25%. This means that under ideal conditions, a SSL with a 100 kW output will generate 300 kW of heat. Implementation of a transient DEW model into the tip-to-tail has shown the thermal management subsystem (TMS) is incapable of managing this heat load unless augmented by a secondary TMS solution, such as thermal storage.[4]

A final contributor to thermal management issues is the fact that aircraft designers are using composite materials to create the aircraft external airframe. Using composite materials is advantageous in that control over material properties is enhanced, they are typically lighter than their metallic counterparts, and they allow for better minimization of the aircrafts radar signature. However, as far as thermal management is concerned, composite materials are problematic because they tend to be better insulators than conductors, thereby trapping heat within the aircraft, rather than rejecting it to the environment.

As future military aircraft, as well as those already in service (through retrofitting), continue to trend towards the design of a more electric aircraft (MEA)[1,2] the need to address the accumulating power and thermal loads becomes critical. Current work by the AFRL, through the INVENT Program, is addressing these issues through thermodynamic modeling, simulation, analysis, and optimization.

1.2 Problem Description

1.2.1 Thermal Issues in Modern Aircraft

As discussed in the preceding section, there are several contributing factors to an increased thermal load on the FTMS and APTMS:

- Heat producing electrical equipment (EMAs, sensors, DEWs)
- Additional mass due to this equipment
- Reduced ram air inlet area
- Reduced ability to reject heat to the environment through the aircraft skin

As the severity of these contributing factors grows, the need for a mission-integrated synthesis/design optimization becomes imperative.

The AFRL tip-to-tail is a platform with which one can analyze the effects on performance of various technologies without having to perform costly physical experiments. Additionally, the tip-to-tail mode can be used to explore the use of exergy analysis in aircraft synthesis/design and, thus, prove the benefits of using exergy destruction as a common optimization metric, as opposed to other, non-unifying performance metric (e.g. coefficients of performance, efficiencies, effectiveness, drag, etc.).

In order to support increased power demands, the size of power subsystems found in modern aircraft are nearly an order of magnitude larger than the last generation of military aircraft.[8] The responsibility of managing these loads is given entirely to the FTMS and APTMS subsystems. The APTMS uses bleed air streams off the engine, ram air heat exchangers, and secondary PAO cooling loops to manage heat loads from the HPEAS and REPS as well as the onboard avionics and the integrated power pack (IPP). Bleed air from the compressor is used to cool the cockpit, while bleed air from the fan is used to cool the avionics through a secondary PAO cooling loop. These two bleed streams are combined to cool the integrated power pack (IPP), which provides electrical power to the aircraft. Figure 1.2 shows a schematic of the APTMS with a DEWS integrated between two heat exchangers.

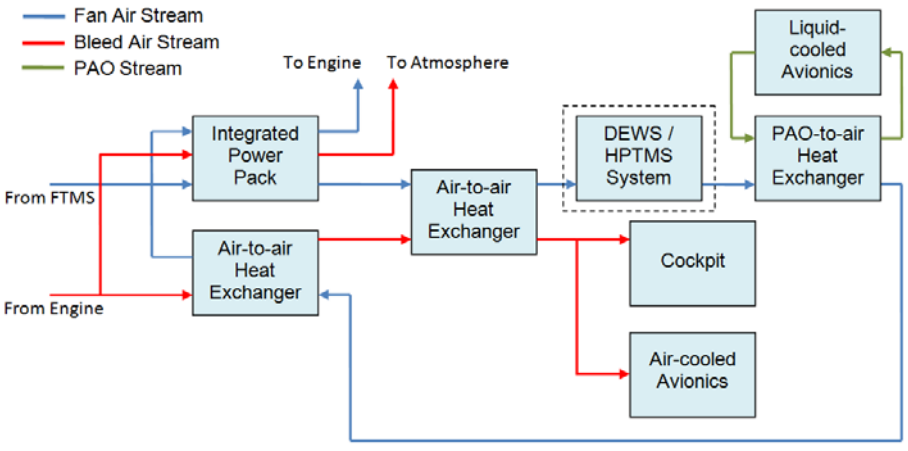

Figure 1.2. Schematic of the INVENT tip-to-tail APTMS.[4]
Gvozdich, G., Modeling the Effects of Transient High Energy Weapon Subsystems on High-Performance Aerospace Subsystems, M.S. Thesis, adviser: M. R. von Spakovsky, Department of Mechanical Engineering, Virginia Tech, Blacksburg, VA, 2011. Used with the permission of Grant G. Gvozdich, 2012.

The FTMS uses bleed air, PAO, oil, and fuel to manage thermal loads. Within the FTMS, fuel is the principal coolant for the PAO loop used to cool bleed air sent to the APTMS and oil from the engine oil pumps. Additionally, fuel is used to manage heat loads from the DEWS and electric starter generator (ESG). However, for the purposes of this thesis work, the DEWS has been turned off and plays no significant role in the performance of the aircraft. Controllers integrated into the FTMS ensure that the fuel temperature stays below the vaporization temperature of JP-8 fuel, typically around 138°F.[8] A schematic of the FTMS can be found in Figure 1.3.

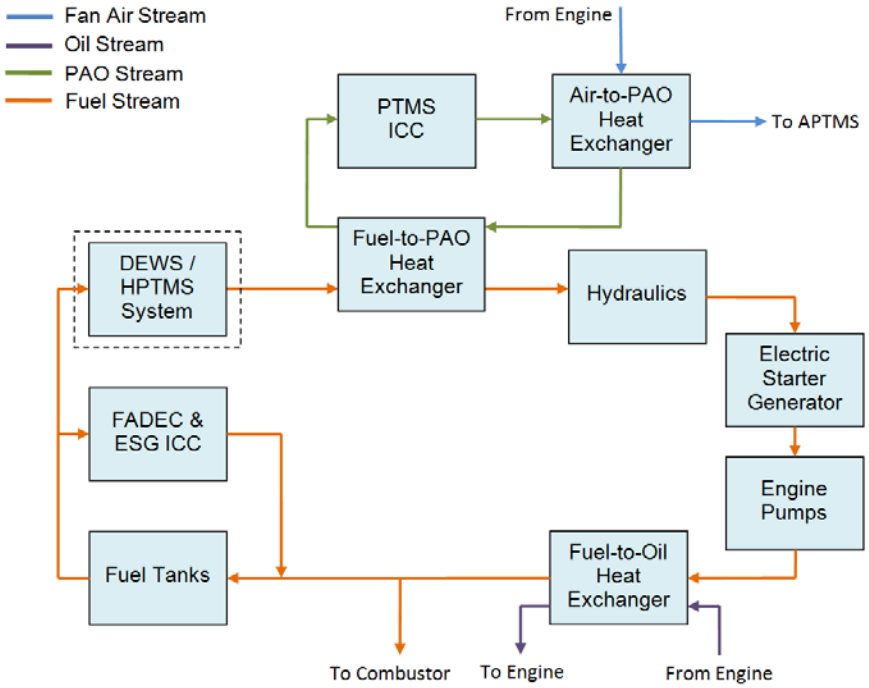

Figure 1.3. Schematic of the INVENT tip-to-tail FTMS.[4]
Gvozdich, G., Modeling the Effects of Transient High Energy Weapon Subsystems on High-Performance Aerospace Subsystems, M.S. Thesis, adviser: M. R. von Spakovsky, Department of Mechanical Engineering, Virginia Tech, Blacksburg, VA, 2011. Used with the permission of Grant G. Gvozdich, 2012.

1.2.2 Simulation of a Mission

The mission profile for the tip-to-tail, shown in Figure 1.4 and Table 1.1, is defined by time dependent altitudes and Mach numbers. As the simulation progresses through time, the altitudes and Mach numbers are sent to the AVS. Using these inputs, the drag-polar model (described in

Section 3.1) implemented in the AVS calculates the thrust demand, which gets sent to an engine controller that varies fuel flow to the engines in the tip-to-tail. Air properties over the entire mission are based on the International Standard Atmosphere tables. The fuel in the aircraft's tanks is at ambient temperature at the start of the mission.

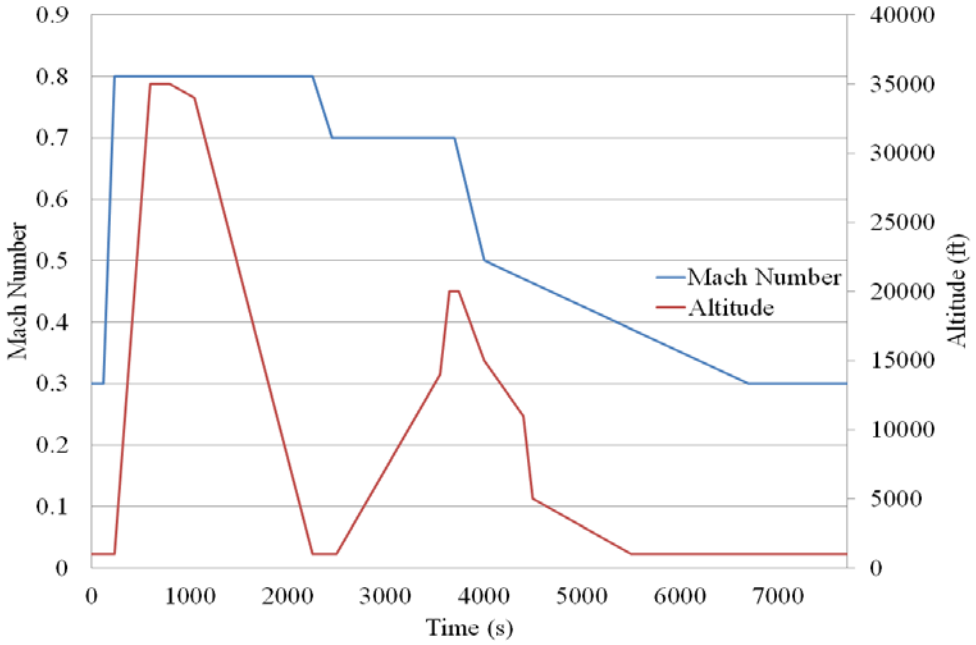

Figure 1.4 INVENT tip-to-tail mission profile.

Table 1.1 INVENT tip-to-tail mission profile in detail.

Mission Segment	Descripton	Duration (s)	Starting Mach Number	Ending Mach Number	Starting Altitude [ft]	Ending Altitude [ft]
1	Subsonic Acceleration	78	0	0.8	1,000	1,000
2	Transonic Climb	405	0.8	0.8	1,000	35,000
3	Transonic Cruise	517	0.8	0.8	35,000	35,000
4	Transonic Descent	500	0.8	0.8	35,000	30,000
5	Subsonic Deceleration/ Descent 1	500	0.8	0.7	30,000	20,333
6	Subsonic Descent 1	1000	0.7	0.7	20,333	1,000
7	Subsonic Cruise 1	250	0.7	0.7	1,000	1,000
8	Subsonic Climb	454	0.7	0.7	1,000	20,000

Mission Segment	Descripton	Duration (s)	Starting Mach Number	Ending Mach Number	Starting Altitude [ft]	Ending Altitude [ft]
9	Subsonic Deceleration	296	0.7	0.5	20,000	20,000
10	Subsonic Deceleration / Descent 2	1500	0.5	0.45	20,000	11,000
11	Subsonic Descent 2	1200	0.45	0.45	11,000	2,000
12	Subsonic Cruise 2	1000	0.45	0.45	2,000	2,000

1.2.3 Optimization and Computational Issues

There are several issues impeding the ability to perform successful large-scale optimization with the tip-to-tail model. At present, this model takes approximately 4-5 minutes (in Matlab® Simulink's® accelerator mode) to complete a single simulation on a quad core Intel i7-2600k overclocked to 4.5Ghz. This lengthy simulation time imposes strict limits on the scope of the optimization problem. Even using efficient optimization algorithms, guaranteeing convergence to a global optimum requires the completion of approximately 2^N simulations, where N is the number id degrees of freedom (DOF) or decision variables. While statistical methods such as design of experiments (DoE) can decrease this quantity significantly, unless simulation time can be reduced by over an order of magnitude, large scale optimization of the tip-to-tail will be impractical even if the code parallelization and faster processors become available.

The second issue hindering the optimization of the tip-to-tail model as initially developed is the set of transient heat exchanger models found in the tip-to-tail model provided by the AFRL. These heat exchanger models, while correctly implemented, are insufficient for the purposes of optimization for several reasons: the correlations used to determine the heat transfer coefficients are not applicable to the physical system and there are no correlations linking the physical (geometric) parameters of a compact heat exchanger (e.g., mass, volume, etc.) to its performance. By leaving these issues unresolved, successful optimization of the tip-to-tail is not possible due to the fact that the numerous heat exchangers in the tip-to-tail add mass to the system and play a critical role in the overall thermodynamic performance of the system.

1.3 Advantage of Using Exergy a Common Metric

The exergy or available energy of a system A is defined with respect to reservoir R as the largest amount of energy that can be transferred to a weight out of a composite system of the system A and the reservoir R in a weight process that starts with system A in state A_1, with values $(n)'$ and $(\beta)'$, and ends with system A in mutual stable equilibrium with R and in a state with values $(n)''$ and $(\beta)''$.[9] Effectively, available energy can be described as the potential of a system to do work, with respect to some environment or reservoir.

In highly coupled and complex systems, it can be challenging to identify where internal losses occur and how significant the losses are when only mass, energy, and momentum balances are used. These balances do not incorporate the concept that energy has a both a quantity and quality associated with it. Thus, heat interactions and work interactions are treated as equally valuable, yet heat interactions carry entropy, while work interactions do not. As a consequence, energy balances cannot capture internal system losses that occur as a result of irreversibilities due to chemical reactions, friction, heat transfer, expansions, contractions, etc.

However, exergy balances incorporate both energy and entropy balances. By implementing exergy balances within each component of the system, and using a common reference state, it is possible to determine not only the location, but also the magnitude of internal losses. Thus, total exergy destruction can be used as the single-unifying metric of loss and efficiency throughout and across an aircraft. In design challenges where the goal is to make a system that performs a task using the least amount of energy possible, exergy destruction minimization can be used as an objective function within an optimization problem. The solution to the optimization problem will be the set of parameters that not only minimizes internal losses, thereby ensuring an "energy optimized" system, but also ensures that the system is feasible, i.e., does not violate the Second Law of Thermodynamics. The use of exergy as a metric and objective function as a well as other metrics such as fuel minimization as objectives functions is discussed in Chapter 2. In this thesis work both exergy destruction and fuel minimization are used in the mission integrated results presented in Chapter 5.

1.4 Thesis Objectives

The purpose of this research is to use mission-integrated synthesis/design optimization to find the set of parameters that optimize the performance of the INVENT tip-to-tail model of a military long-range strike aircraft. Surrogate based analysis and optimization (SBAO) is employed to minimize the number of simulations required and to lessen the impact of long simulation times. The INVENT tip-to-tail and heat exchanger models described in this thesis work are conceptual in nature. The tip-to-tail model is intended to describe a generic aircraft and, thus, any data utilized in the model is generic in nature and not representative of any particular aircraft or aircraft subsystem. Thus, the results presented as part of this thesis work are also conceptual in nature.

The first objective in accomplishing this goal is to develop transient heat exchanger models using thermodynamic balances, heat transfer models, and semi-empirical correlations which tie heat exchanger geometry to performance. These heat exchanger models will contain first and second law balance equations, ensuring that no second law violations occur. Once model equations have been developed, they will be implemented in Matlab® Simulink® environment to ensure compatibility with the current tip-to-tail model. Heat exchanger models will be validated using the published literature and integrated into the tip-to-tail model – replacing all current heat exchanger models.

The second objective of this research is to demonstrate the efficacy of SBAO in finding the set of parameters that optimizes to a global optimum. This will initially be demonstrated with the optimization of the newly developed heat exchanger model by finding the set of parameters, subject to a set of constraints, which minimizes exergy destruction. This optimum set of parameters will be compared to results found using gradient based, genetic algorithm, and pattern search optimization techniques.

The third objective is to implement a set of system as well as component level exergy balance equations into the tip-to-tail model. Exergy balance equations, as described in section 1.3, are useful in determining where internal irreversibilities occur in the system. Exergy balances will be implemented for the total vehicle (including the wake), the engine, the airframe, and any heat exchanger models integrated into the tip-to-tail model. Using data from the exergy

analysis, an itemization of internal irreversibilities will be created as a way to map out where the significant losses occur in the tip-to-tail model.

The fourth objective is to perform mission-integrated synthesis /design optimization on the tip-to-tail model, using exergy destruction and fuel minimization as objective functions. Optimization of the tip-to-tail will be performed using the Design Explorer algorithm provided by Phoenix Integration's ModelCenter® software.

Chapter 2 - Literature Review

Within the aerospace community, mission-integrated vehicle optimization has emerged as an important part of the design process. This chapter explores the various strategies and techniques used to explore design spaces, optimize vehicles, and measure performance.

2.1 Modeling, Analysis, and Optimization of Aerospace Systems

Modern aircraft are complex systems, consisting of many unique subsystems that are intimately linked through various subsystem interactions. Modeling each subsystem as well as the interactions existing between them is a challenging objective, often resulting in a very complex model, especially if transient effects are also included in the model. Simulations of such systems are typically computationally expensive; and, consequently, system optimization can be extremely computationally and financially expensive. In order to reduce run time for both the simulation and optimizations processes, it is important to not only have an efficiently written simulation code but an efficient optimization algorithm as well. This section is an exploration of past work involving the modeling and synthesis/design optimization of aerospace systems. Several key ideas are addressed, including the concept of using exergy destruction minimization as an optimization objective function.

2.1.1 Mission-Integrated Synthesis/Design Optimization of Fighter Aircraft Systems

Muñoz[10], Muñoz and von Spakovsky[11,12,13], and von Spakovsky[14,15] developed an Iterative Local-Global Optimization (ILGO) decomposition strategy which they applied to the optimization of a supersonic fighter aircraft. ILGO is used to break a complex optimization problem into a set of simpler, subsystem level optimization problems in a manner similar to that of a variety of local-global optimization strategies described in the literature (e.g., see Sobieszczanski-Sobieski[16,17]). Associated with each of the subsystem problems is an Optimum Response Surface (ORS), which when combined results in a system-level ORS which when explored leads to the global system optimum. Each subsystem ORS defines the optimum set of subsystem synthesis/design parameter values relative to a set coupling functions that describe the

relationships or interactions between each subsystem. In LGO these subsystem ORSs are used as surrogates in the system level optimization problem, thus significantly simplifying the size of each optimization problem which must be solved. Unfortunately, this comes at the expense of a significantly increased computational burden since in effect one is left with a set of nested optimizations, i.e., a set of subsystem optimizations within an overall system level optimization. In other words, one must construct the entire system-level ORS to search for the global optimum.

ILGO in contrast imbeds all system-level information within each subsystem problem, eliminating the nesting and, thus, the need to construct the system-level ORS, which is iteratively searched using only local gradient information. In this way ILGO not only simplifies each optimization problem but significantly reduces the overall computational burden.

The aircraft model optimized is comprised of a propulsion subsystem (PS), environmental controls subsystem (ECS), airframe subsystem-aerodynamics (AFS-A), expendable and permanent payload subsystems (EPAY and PPAY), and an equipment group (EG). The model equations governing the behavior of each subsystem were adapted from Mattingly et al.[18] and Mattingly[19]. The aircraft is flown over a mission consisting of fourteen unique mission segments, described schematically in Figure 2.1. Using the 154 local/global synthesis/design variables and operational decision variables, the optimization problem is formulated and solved for their optimum values, subject to a set of constraints, using three unique objective functions:

- Minimization of gross total take-off weight
- Minimization of total fuel consumption
- Minimize of gross total aircraft cost

Convergence results from the gross take-off weight minimization problem are found in Figure 2.2. As can be seen, after four ILGO iterations, the optimizer reaches an optimal solution of 10,364 kg. From Figure 2.3 it is clear that there is a strong, highly linear relationship between gross take-off weight for the vehicle and fuel consumption so that a vehicle optimized for minimum gross take-off weight is simultaneously optimized for minimum fuel consumption. In fact, these authors show that the optimum set of decision variable values determined from the optimization is the same for all three objective functions. The optimal costs and weights associated with the aircraft can be found in Table 2.1.

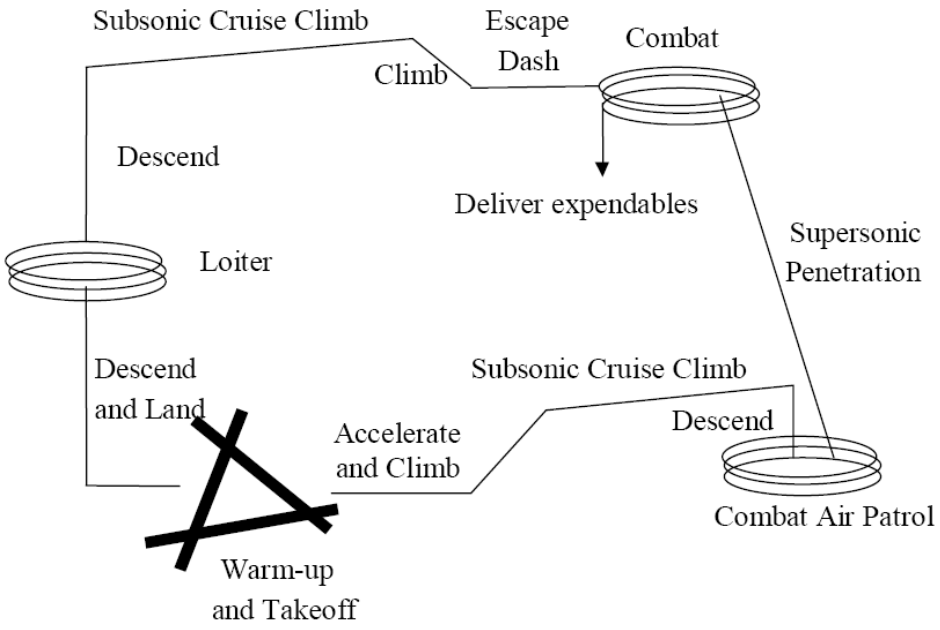

Figure 2.1. Mission profile by phase or leg.[34]
Anderson, J. D., 1984, Aircraft Performance and Design, New York: McGraw-Hill. Used under fair use, 2012.

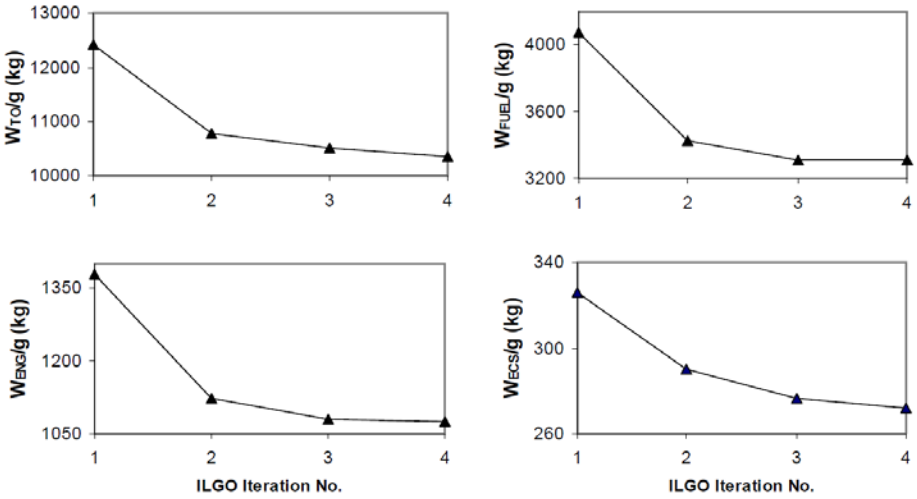

Figure 2.2. ILGO evolution and convergence of the gross take-off weight, fuel, AFS-A, PS weights.[20]
Rancruel, D. F., *A Decomposition Strategy Based on Thermoeconomic Isolation Applied to the Optimal Synthesis/Design and Operation of an Advanced Fighter Aircraft System*, M.S. Thesis: adviser: M. R. von Spakovsky, Department of Mechanical Engineering, Virginia Polytechnic Institute and State University, Blacksburg, VA, 2003. Used with permission of D. F. Rancruel, 2012.

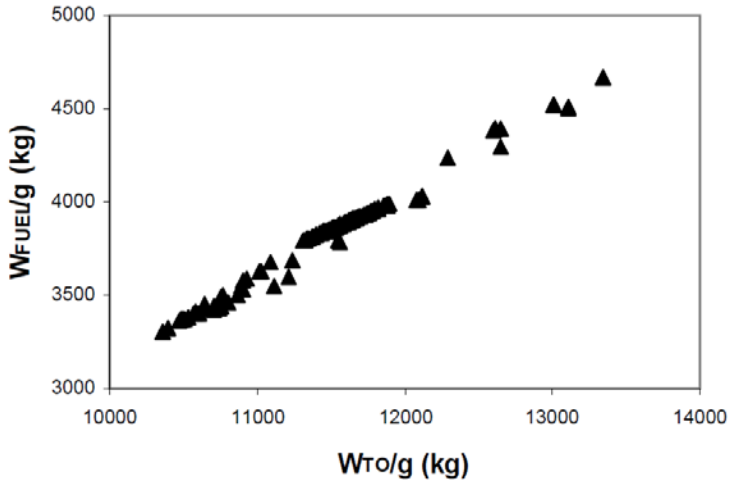

Figure 2.3. Fuel weight versus gross take-off weight corresponding to feasible solutions obtained at different iterations of the overall (system level) optimization.[23]
Rancruel, D. F., von Spakovsky, M. R., 2004, *Advanced Fighter Aircraft Sub-systems Optimal Synthesis/Design and Operation: Airframe Integration Using a Thermoeconomic Approach*, 10th AIAA/ISSMO Multi-disciplinary Analysis and Optimization Conference, Aug. 30 - Sept. 1, Albany, New York, vol. 6: pp. 3403-3415. Used under fair use, 2012.

Table 2.1. Optimum weights and costs; the latter are given in thousands of 1999 dollars; 8000 flight hours and a fuel price of \$0.02/lb_m are assumed.[23]
Rancruel, D. F., von Spakovsky, M. R., 2004, *Advanced Fighter Aircraft Sub-systems Optimal Synthesis/Design and Operation: Airframe Integration Using a Thermoeconomic Approach*, 10th AIAA/ISSMO Multi-disciplinary Analysis and Optimization Conference, Aug. 30 - Sept. 1, Albany, New York, vol. 6: pp. 3403-3415. Used under fair use, 2012.

$W_{TO/g}$ (kg)	**10364**	**Fuel cost**	7778
$W_{FUEL/g}$ (kg)	3308	**ECS cost**	541
$W_{SS/g}$ (kg)	4526	**PS cost**	5642
$W_{ENG/g}$ (kg)	1075	**AFS-A cost**	14140
$W_{ECS/g}$ (kg)	272		
$W_{E/PPAY-EG/g}$ (kg)	1183		

A more comprehensive optimization of an advanced fighter aircraft system can be found in the work of Rancruel[20], Rancruel and von Spakovsky[21,22,23], and von Spakovsky[14,15], who utilize the methods outlined by Muñoz and von Spakovsky.[11,12,13] The aircraft model is comprised of a

PS, ECS, AFS-A, vapor-compression/PAO subsystem (VC/PAOS), and a fuel loop subsystem (FLS). The aircraft is flown over the same mission as in Figure 2.1.

Convergence results from the gross take-off weight minimization problem are found in Figure 2.4. As can be seen, after seven ILGO iterations the optimizer reaches an optimal solution of 10,180 kg. The optimization problem posed by Rancruel and von Spakovsky uses 493 local/global synthesis/design and operational decision variables, as opposed to the 154 used in the problem of Muñoz and von Spakovsky. However, the improvement in total gross take-off weight is only 184 kg, Nonetheless, the larger number of degrees of freedom and additional subsystems results in a much more detailed system, subsystem, and component optimum. Furthermore, as seen in Table 2.2, allowing for AFS-A degrees of freedom and including additional subsystems results in a lighter vehicle with a larger (by 783kg) payload as well as the maintenance, throughout the entire mission (see Figure 2.5), of the fuel temperature below the vaporization temperature.

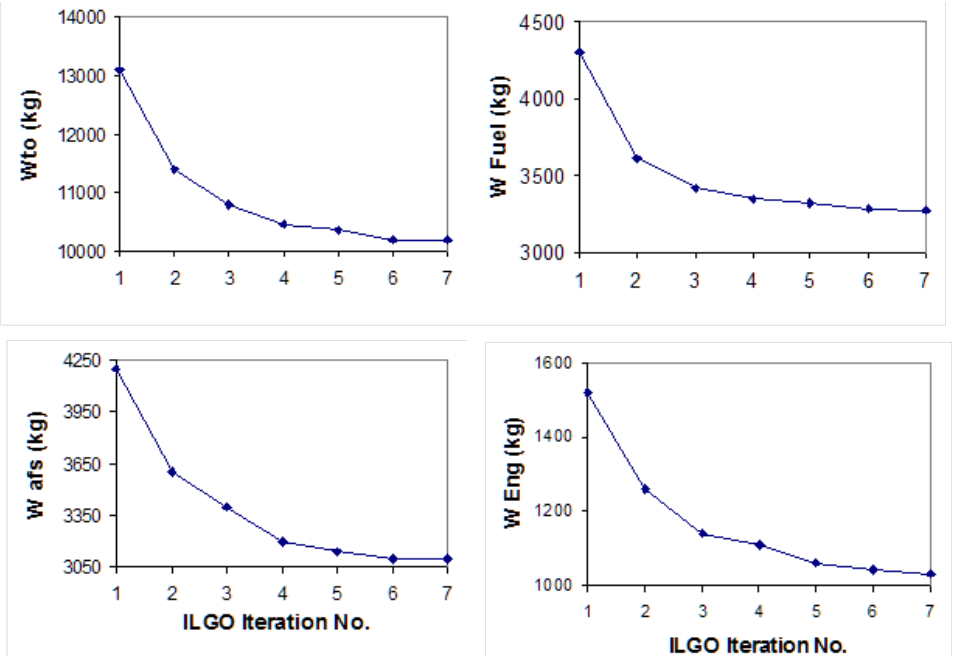

Figure 2.4. Evolution of the take-off gross weight, fuel weight, AFS weight, and PS weight at different points of the iterative local-global optimization (ILGO) approach.[20]

Rancruel, D. F., *A Decomposition Strategy Based on Thermoeconomic Isolation Applied to the Optimal Synthesis/Design and Operation of an Advanced Fighter Aircraft System*, M.S. Thesis: adviser: M. R. von Spakovsky, Department of Mechanical Engineering, Virginia Polytechnic Institute and State University, Blacksburg, VA, 2003. Used with the permission of D. F. Rancruel, 2012.

Table 2.2. PS, FLS, VC/PAOS, AFS-A, and ECS optimum masses for the case with AFS-A DOF.[20]

Rancruel, D. F., *A Decomposition Strategy Based on Thermoeconomic Isolation Applied to the Optimal Synthesis/Design and Operation of an Advanced Fighter Aircraft System*, M.S. Thesis: adviser: M. R. von Spakovsky, Department of Mechanical Engineering, Virginia Polytechnic Institute and State University, Blacksburg, VA, 2003. Used with the permission of D. F. Rancruel, 2012.

$W_{TO/g}$ (kg)	10180
$W_{FUEL/g}$ (kg)	3270
$W_{EMPTY/g}$ (kg)	3855
$W_{PAYLOAD/g}$ (kg)	1210
$W_{EG/g}$ (kg)	756
$W_{ECS/g}$ (kg)	260
$W_{FLS/g}$ (kg)	320
$W_{ENG/g}$ (kg)	1032
$W_{VC/PAOS/g}$ (kg)	232

$W_{AFS/g}$ (kg)	3100
Wing	998.4
Tail	193.3
Fuselage	1076.6
Main Landing Gear	432.5
Nose Landing Gear	117.8
Engine Mounts	25.7
Firewall	40.7
Engine Section	14.4
Air Induction	199.4

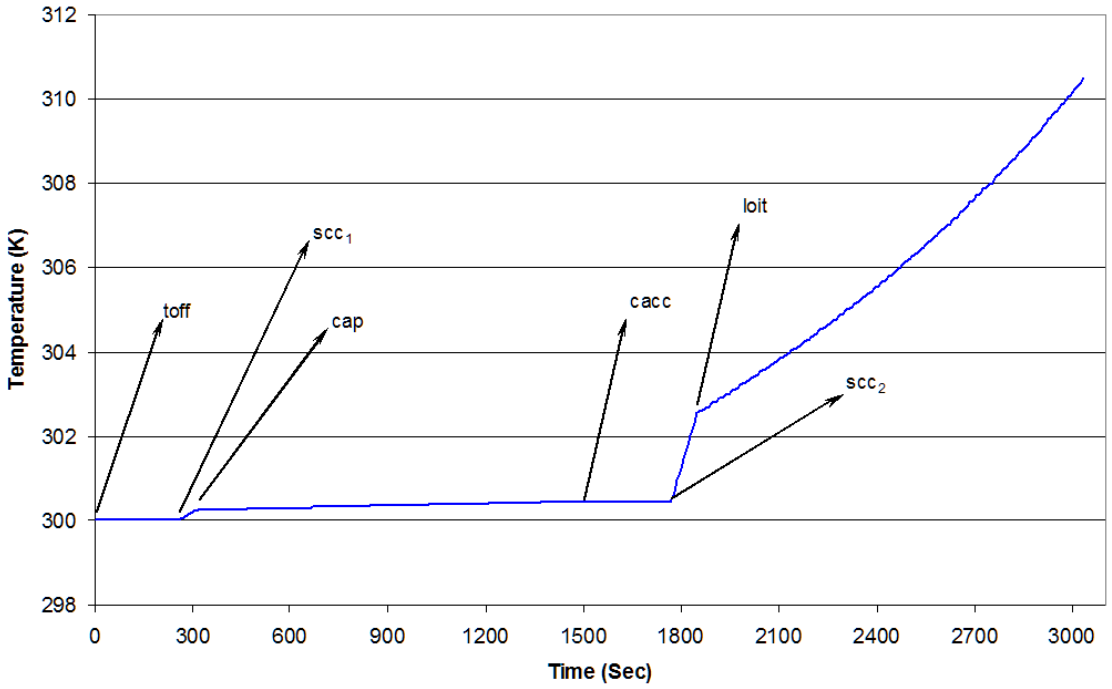

Figure 2.5. Fuel tank temperature versus time.[20]

Rancruel, D. F., *A Decomposition Strategy Based on Thermoeconomic Isolation Applied to the Optimal Synthesis/Design and Operation of an Advanced Fighter Aircraft System*, M.S. Thesis: adviser: M. R. von Spakovsky, Department of Mechanical Engineering, Virginia Polytechnic Institute and State University, Blacksburg, VA, 2003. Used with the permission of D. F. Rancruel, 2012.

2.1.2 Exergy Analysis for the Mission-Integrated Synthesis/Design Optimization of a Hypersonic Vehicle

In work on hypersonic vehicle optimization, Markel[24] and von Spakovsky[15] show that an exergy based objective function performs well when compared to typical optimization objective functions and can yield superior solutions. In the author's work, energy and exergy balances, augmented by semi-empirical correlations, are implemented to develop the model equations governing the behavior of the hypersonic vehicle. The model, represented schematically in Figure 2.6, consists of two subsystems, a PS and an AFS-A. The PS consists of three primary components: the inlet/isolator, combustor, and nozzle/afterbody. The model is flown through a three-segment mission described in Table 2.3. The optimization problem is formulated using seven synthesis/design variables and three objectives, i.e.,

- Maximize thrust efficiency
- Minimize the rate of exergy destruction plus the rate of fuel exergy loss
- Minimize rate of exergy destruction
-

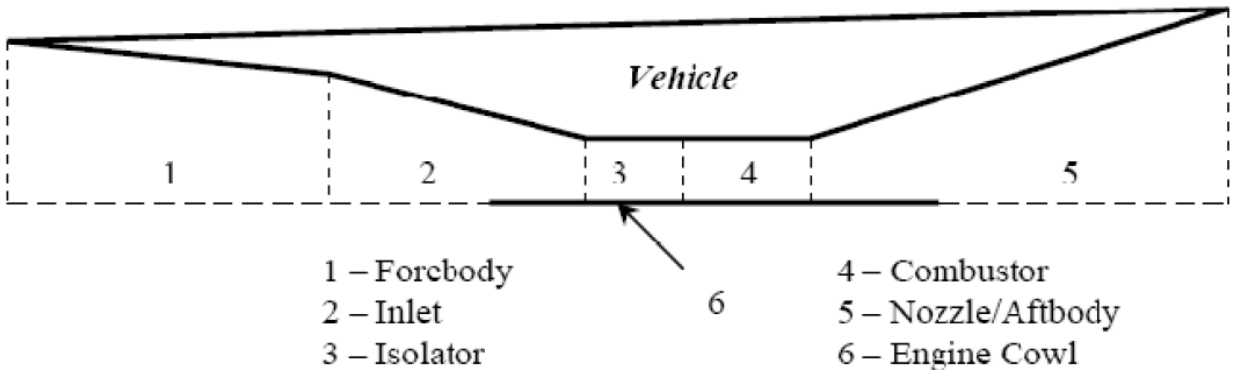

Figure 2.6. Hypersonic vehicle configuration.[24]
Markel, K. C., *Exergy Methods for the Generic Analysis and Optimization of Hypersonic Vehicle Concepts*, M.S. Thesis, adviser: M. R. von Spakovsky, Department of Mechanical Engineering, Virginia Tech, Blacksburg, VA, 2005. Used under fair use, 2012.

Table 2.3. Partial mission specifications.[24]
Markel, K. C., *Exergy Methods for the Generic Analysis and Optimization of Hypersonic Vehicle Concepts*, M.S. Thesis, adviser: M. R. von Spakovsky, Department of Mechanical Engineering, Virginia Tech, Blacksburg, VA, 2005. Used under fair use, 2012.

Segment	Description
0	Mach 8 cruise for 1000 nm
1	Accelerate and climb from Mach 8 to Mach 10, t < 90s
2	Mach 10 cruise for 100 nm

Optimal design decision variable (see Figure 2.7) results for the three different objectives are found in Table 2.4 and show that the vehicle optimized for minimum rate of exergy destruction plus rate of exergy fuel loss is more slender than that optimized for maximum thrust efficiency, with a larger inlet and smaller nozzle. Since the lengths of both vehicles are the same, the former has a smaller volume and consequently a smaller empty mass. Optimal results for the operational decision variables, i.e., the angle of attack (α) in degrees and the wing planform area (S_{wing}) in m^2, are given in Table 2.5 for the three mission segments of the partial scram jet mission. Details about the exergy analysis done for this vehicle appear in Markel[24] and von Spakovsky.[15]

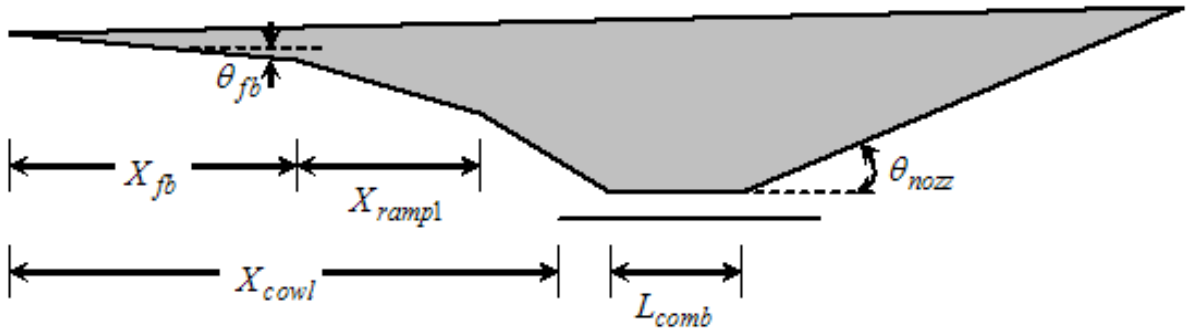

Figure 2.7. Hypersonic vehicle design decision variables.[15]
von Spakovsky, M. R., 2011, *Chapter 10 - MIS/DO Applied to High Performance Aerospace Vehicles*, Exergy Analysis and Design Optimization for Aerospace Vehicles and Systems, editors: Camberos J. and Moorhouse D., AIAA book series. Used under fair use, 2012.

Table 2.4. Optimal design decision variable values for the partial mission.[24]
Markel, K. C., *Exergy Methods for the Generic Analysis and Optimization of Hypersonic Vehicle Concepts*, M.S. Thesis, adviser: M. R. von Spakovsky, Department of Mechanical Engineering, Virginia Tech, Blacksburg, VA, 2005. Used under fair use, 2012.

Objective Function	X_{fb}	X_{cowl}	X_{ramp1}	θ_{fb}	θ_{nozz}	L_{comb}	$\%_{cowl}$
η_0	8.4371	13.186	3.2913	1.2179	15.835	0.6385	0.0010
$\dot{X}_{des}$	8.5021	13.667	2.7605	1.0017	15.889	0.5067	0.0115
$\dot{X}_{des}+\dot{X}_{fuel\ loss}$	8.8604	13.959	3.2978	1.0176	14.106	0.8240	0.1610

Table 2.5. Optimal operational decision variable values for the partial mission.[24]
Markel, K. C., *Exergy Methods for the Generic Analysis and Optimization of Hypersonic Vehicle Concepts*, M.S. Thesis, adviser: M. R. von Spakovsky, Department of Mechanical Engineering, Virginia Tech, Blacksburg, VA, 2005. Used under fair use, 2012.

Objective Function	α			S_{wing}		
	0	1	2	0	1	2
η_0	1.7724	1.2	0.9	7.2033	5.7615	9.3670
$\dot{E}x_{des}$	1.4453	0.8	0.8	7.6983	9.2350	0.4869
$\dot{E}x_{des}+\dot{E}x_{fuel_{loss}}$	1.1933	0.4	0.3	0.7908	3.2372	0.5065

Brewer[25], Brewer, Markel and von Spakovsky[26], and von Spakovsky[15] performed a similar analysis and mission-integrated optimization using a more detailed mission profile and a larger set of synthesis/design variables. The vehicle model used is the same as that of Markel. The mission profile used is given in Figure 2.8. Two of the same three objectives, except on a non-rate basis, are used, namely, maximize thrust efficiency and minimize exergy destruction plus fuel exergy loss. A third objective is to minimize fuel consumption. Three separate optimizations with each objective are made using a genetic algorithm to ensure that a global optimum is reached. Optimal results for each objective are found in Table 2.6.

As can be seen from these results, the second and the third objectives produce very similar optimal solutions with optimizations fun one being the best for all three objectives. This is expected due to the fact that the primary source of available energy in an aircraft is the fuel. What is lacking with the second objective, however, is a detailed map of where the greatest internal losses due to irreversibilities occur, something which is a natural consequence of the third objective optimization.

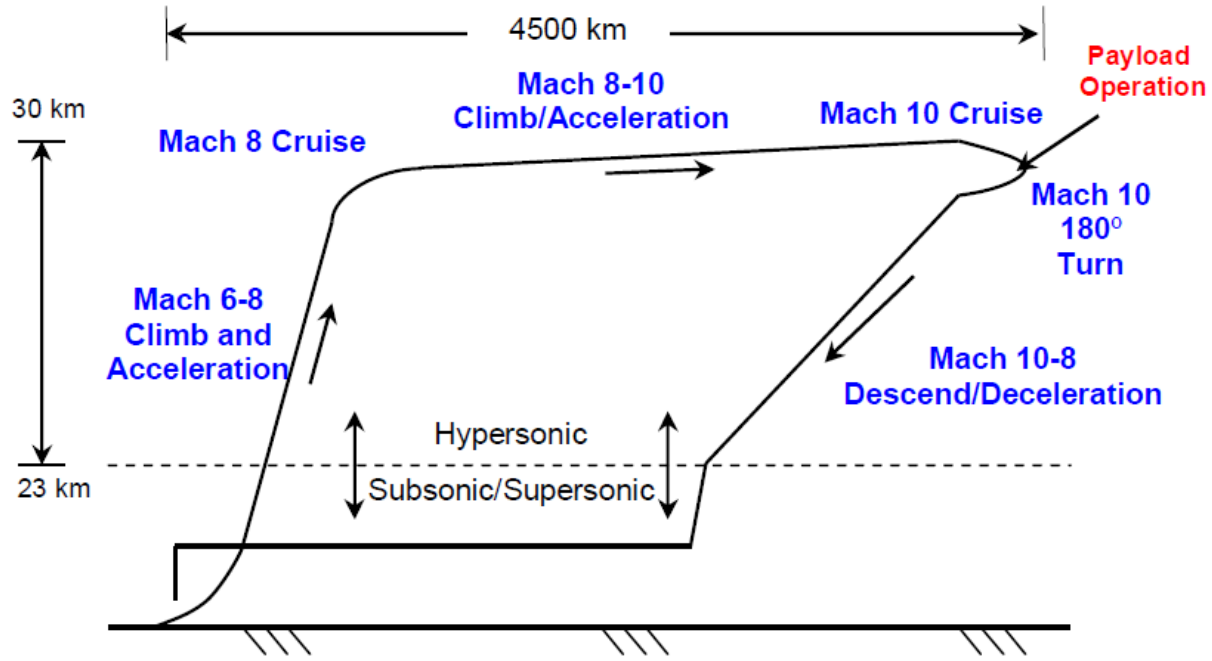

Figure 2.8. Total scramjet vehicle mission.

Table 2.6. Optimal objective function results.

Objective Function	**Max. Thrust Efficiency**			**Min. Fuel Mass**			**Min. Exergy Destroyed + Fuel Exergy Lost**		
Run	**1**	**2**	**3**	**1**	**2**	**3**	**1**	**2**	**3**
Thrust Efficiency [%]	**34.52**	34.48	32.97	29.38	26.40	26.41	28.76	29.89	26.57
Fuel Mass [kg]	1911	1911	2227	**1717**	1720	1744	1732	1797	1801
Exergy Destruction [GJ]	153.7	151.1	166.2	145.2	139.3	140.2	**140.0**	142.3	143.1

Table 2.7. Single-segment optimized vehicle mission-level performance.[25]
Brewer, K. M., *Exergy Methods for the Mission-Level Analysis and Optimization of Generic Hypersonic Vehicles*, M.S. Thesis, adviser: M. R. von Spakovsky, Department of Mechanical Engineering, Virginia Polytechnic Institute and State University, Blacksburg, VA, 2006. Used with the permission of K. M. Brewer, 2012.

Vehicle Opt. Segment	Angle of Attack [°]	Failure Segment	Where	Reason
1	Completed Mission			
2	$\alpha \leq 2.0$	1	Comb.	$M < 1$
	$\alpha > 2.0$	1	Inlet	Shock-on-lip
3	$\alpha \leq 1.7$	1	Comb.	$M < 1$
	$\alpha > 1.7$	1	Inlet	Shock-on-lip
4	$\alpha \leq 1.9$	1	Comb.	$M < 1$
	$\alpha > 1.9$	1	Inlet	$M < 2.2$
5	$\alpha \leq 2.0$	1	Comb.	$M < 1$
	$\alpha > 2.0$	1	Inlet	$M < 2.2$
6	$\alpha \leq 1.8$	1	Airframe	$S_{wing} > S_{wing,\,max}$
	$\alpha > 1.8$	1	Inlet	Shock-on-lip

This work furthermore shows the importance of mission-integrated optimization. As seen inTable **2.7**, single-segment optimizations are carried out using the exergy objective and the resulting six optimal vehicles are flown over the entire mission. Only optimal vehicle one is able to complete the entire mission. However, this optimal vehicle is compared with that resulting from the mission-integrated optimization, it is obvious as seen in Figure 2.9, that the former does not perform nearly as well as the latter, i.e., the single-segment optimized vehicle consumes 1877kg of mass over the entire mission as compared to 1732kg, an 8.4% increase.

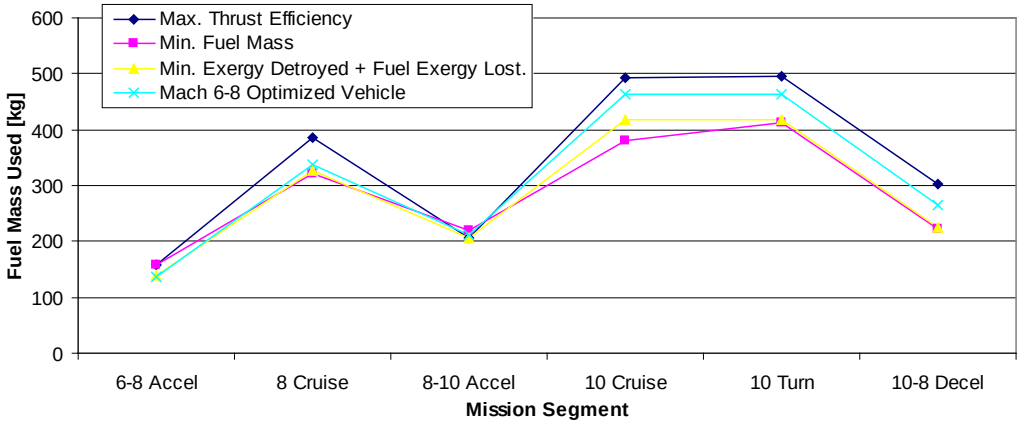

Figure 2.9. Fuel mass consumed by the Mach 6 to Mach 8 single-segment optimized vehicle as compared to the mission-level optimized vehicles.

2.1.3 Exergy Analysis for High-Performance Aircraft System Optimization

Periannan[27], Periannan, von Spakovsky, and Moorhouse[28], and von Spakovsky[14] investigate how using exergy-based objective functions, rather than energy-based objective functions, alters the optimal design of a fighter aircraft system. The optimization decision variables are those for an aircraft system composed of a PS, ECS, and AFS-A. These subsystems are modeled in a fashion similar to the models implemented by the authors in section 2.1.1. The five optimization objectives used are:

1. Minimize the gross takeoff weight
2. Minimize the exergy destruction in the PS and ECS plus the exergy of the unburned fuel lost out the back end of the PS.
3. Minimize the exergy destruction in the PS, ECS, and AFS-A plus the exergy of the unburned fuel lost out the back end of the PS.
4. Maximize of the energy-based thrust efficiency.
5. Maximize of the exergy-based thermodynamic effectiveness.

The optimization problem is formulated using 16 synthesis/design decision variables, i.e., degrees of freedom (DOF) (11 from the ECS, 4 from the PS, 1 from the AFS-A) and solved using a gradient-based algorithm. To ensure that the algorithm does converge to local optima, a variety of significantly different initial starting points are used. Optimal results for objectives 1, 2, 3, and 4 are found in Figure 2.10, Figure 2.11, and Figure 2.12. Objective 5 was not included due to the fact that it is conceptually the same as objective 3. As can be seen, with DOF included for each subsystem, objective 3 consistently gives better results for gross takeoff weight, fuel consumption, and exergy destruction and loss. In particular, a comparison between the energy-based objective (objective 1) and the exergy based objective (objective 3) show that the latter requires 5.8% less fuel consumption. This seems to confirm the superiority of the exergy-based approach not only in terms of the detailed information provided on the location and magnitudes of the inefficiencies present, but also in terms of the optimality of the solution.

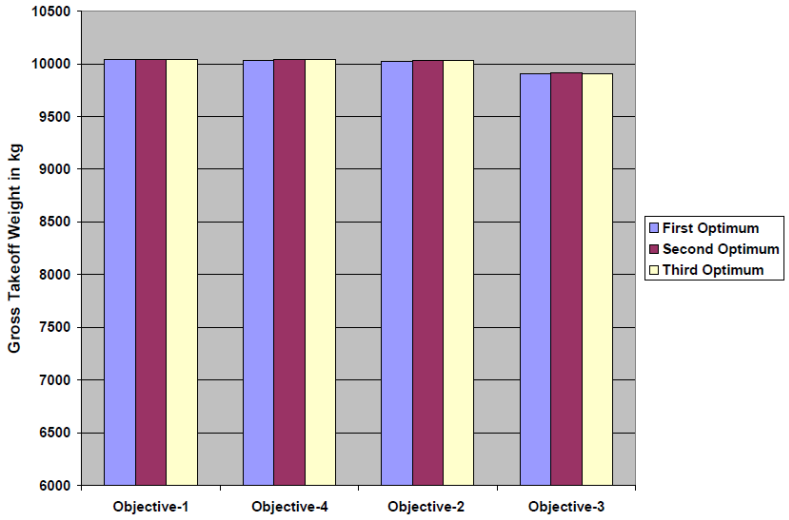

Figure 2.10. Gross takeoff weight obtained for four of the objective functions (objectives 1, 2, 3, and 4) with AFS-A degrees of freedom and a series of three complete optimizations for each objective staring from three significantly different initial points.[27,28,14]
Periannan, V., *Investigation of the Effects of Various Energy and Exergy-Based Objectives/Figures of Merit on the Optimal Design of High Performance Aircraft System*, M.S. Thesis, adviser: M. R. von Spakovsky, Department of Mechanical Engineering, Virginia Tech, Blacksburg, VA, 2005. Used with the permission of Vijay Periannan, 2012.

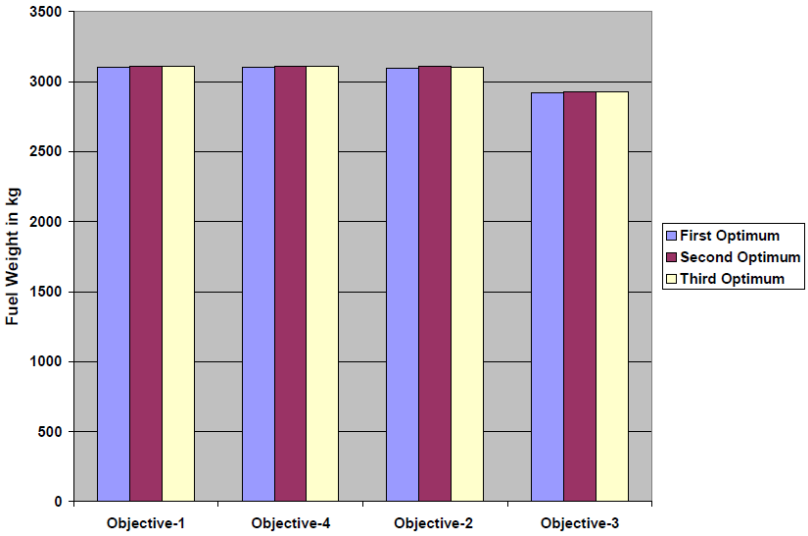

Figure 2.11. Fuel weight obtained for four of the objective functions (objectives 1, 2, 3, and 4) with AFS-A degrees of freedom and a series of three complete optimizations for each objective staring from three significantly different initial points.[27,28,14]
Periannan, V., *Investigation of the Effects of Various Energy and Exergy-Based Objectives/Figures of Merit on the Optimal Design of High Performance Aircraft System*, M.S. Thesis, adviser: M. R. von Spakovsky, Department of Mechanical Engineering, Virginia Tech, Blacksburg, VA, 2005. Used with the permission of Vijay Periannan, 2012.

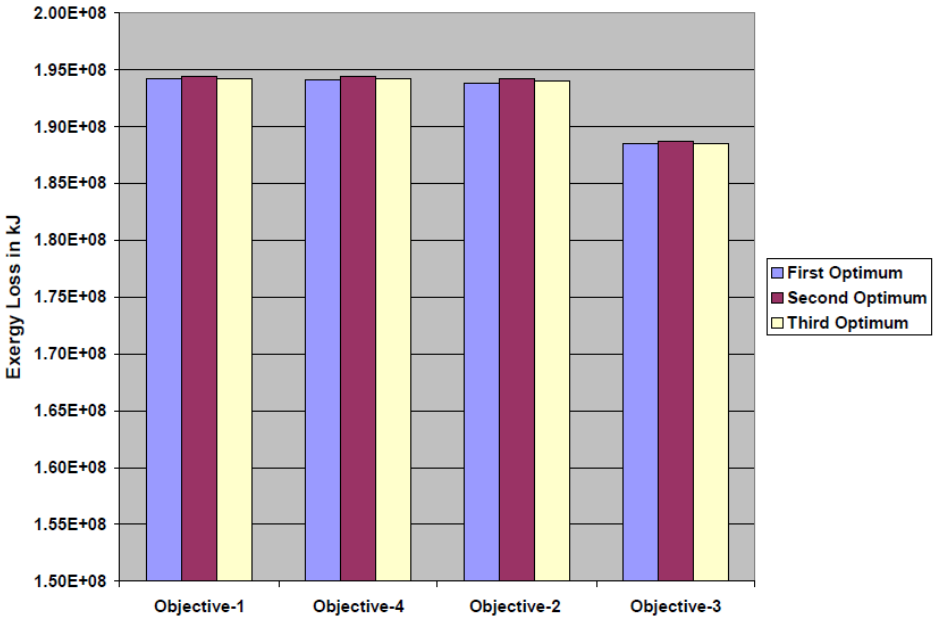

Figure 2.12. Total exergy destruction obtained for four of the objective functions (objectives 1, 2, 3, and 4) with AFS-A degrees of freedom and a series of three complete optimizations for each objective staring from three significantly different initial points.[27,28,14]
Periannan, V., *Investigation of the Effects of Various Energy and Exergy-Based Objectives/Figures of Merit on the Optimal Design of High Performance Aircraft System*, M.S. Thesis, adviser: M. R. von Spakovsky, Department of Mechanical Engineering, Virginia Tech, Blacksburg, VA, 2005. Used with the permission of Vijay Periannan, 2012.

2.1.4 Exergy Analysis for the Mission-Integrated Synthesis/Design Optimization of a Morphing Wing Fighter Aircraft

Butt[29], Moorhouse et al.,[30], Smith[31], Smith and von Spakovsky[32], and von Spakovsky[14] apply the concept of exergy destruction minimization to the optimization of morphing wing fighter aircraft. In the work of Butt[29], Moorhouse et al.[30], and Smith et al.[32], a two-subsystem model is constructed in Matlab® comprised of a PS and an AFS-A. This system is subsequently optimized using a genetic algorithm. The optimization is carried out with a total of 113 synthesis/design and operation decision variables. A very interesting result is the comparison made between the optimal morphing-wing results and those for the same aircraft but with fixed wings. The comparison as part of a sensitivity study is shown in Figure 2.13. Note that the fixed-wing result is shown with the horizontal red line. The sensitivity of the total fuel consumption is plotted with respect to wing-weight and fuel-weight penalties incurred by the morphing wing

aircraft as a result of the weight of the morphing-actuators added to the wings and the additional fuel needed to accommodate the additional weight. As is obvious from the size of the shaded area below the red line, the fuel savings for the morphing-wing aircrafts compared to the fixed-wing aircraft are very significant for many combinations of penalties within the shaded area.

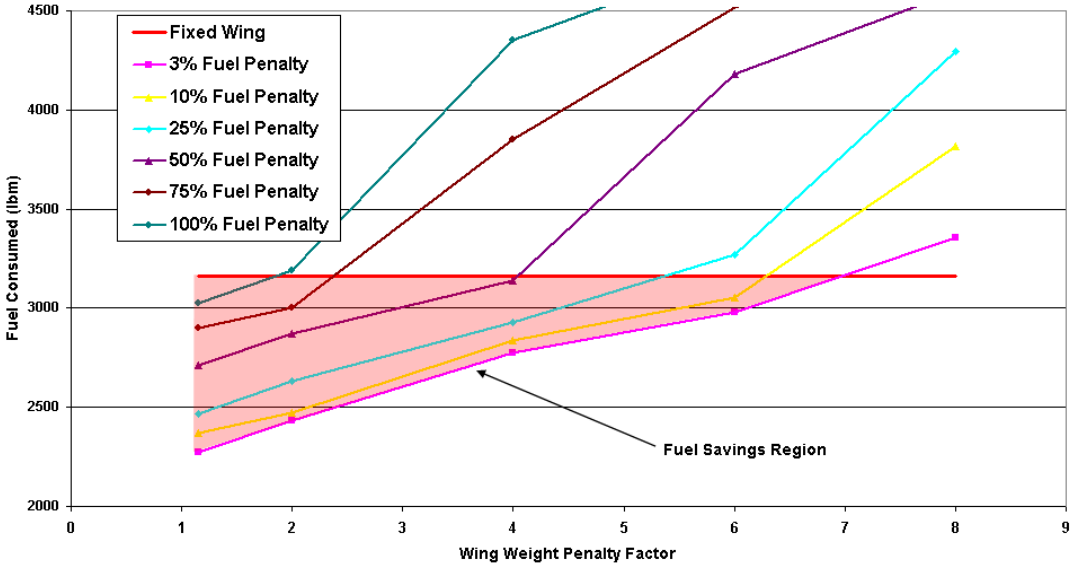

Figure 2.13. Sensitivity analysis of morphing-wing effectiveness for different wing and fuel weight penalties; optimizations for this two-subsystem AAF are based in the minimum fuel burned.[31,32]
Smith, K. W., *Morphing Wing Fighter Aircraft Synthesis/Design Optimization*, M.S. Thesis, adviser: M. R. von Spakovsky, Department of Mechanical Engineering, Virginia Tech, Blacksburg, VA, 2009. Used with the permission of Kenneth W. Smith, 2012.

The work done by Smith[31], Smith et al.[32], and von Spakovsky[14] expands the scope of the optimization problem significantly. In this work, a nine-subsystem air-to-air fighter (AAF) is developed using iSCRIPT™, which is a software language and tool set developed for the purpose of mission-integrated synthesis/design modeling, analysis, and large-scale optimization by TTC Technologies, Inc. The nine subsystems constructed are as follow:

- Morphing-wing AFS-A
- Turbofan PS
- ECS
- FLS
- VC/PAOS

- Electrical subsystem (ES)
- Central hydraulic subsystem (CHS)
- Oil loop subsystem (OLS)
- Flight controls subsystem (FCS)

For a given set of initial conditions and constraints (e.g., Mach number, ambient pressure, compressor pressure ratio, etc.) many simulations of the entire system are run within the iSCRIPT™ built-in genetic algorithm optimizer, initially developed by Leyland[33] and Molyneaux and the Laboratoire a Energétique Industrielle at the Ecole Polytechnique Fédérale de Lausanne. With 734 local-global synthesis/design and operation decision variables and after several hundreds of thousands of simulations a final optimum is reached. A generic 21-segment mission, developed in Anderson[34] is used for the optimization and is described in Table 2.8. Due to the large number of decision variables and the highly non-linear characteristic of the AAF model, the ILGO decomposition strategy is used to optimize the vehicle. It is important to note that the results presented in this work are incomplete due to limitations in the computational resources available at the time. This emphasizes the notion that in order for an optimization problem to be solved in a suitable amount of time, the time cost and resource usage must be minimized, and the optimization algorithm efficient.

Table 2.8. Air-to-air fighter (AAF) mission segments and details.[31]
Smith, K. W., *Morphing Wing Fighter Aircraft Synthesis/Design Optimization*, M.S. Thesis, adviser: M. R. von Spakovsky, Department of Mechanical Engineering, Virginia Tech, Blacksburg, VA, 2009. Used with the permission of Kenneth W. Smith, 2012.

Mission Segment	Description
1	Warm-up and take off, 2000 ft altitude, 1 min for military power warm up, takeoff ground roll + 3 s rotation distance < 1500 ft, $V_{TO} = 1.2 * V_{STALL}$
2	Accelerate to best subsonic climb Mach (BCLM)
3	Minimum time to climb to 20,000 ft at military power
4	Continue minimum time to climb to best cruise Mach (BCM1) and best cruise altitude (BCA1)
5	Subsonic cruise until total distance for climb/cruise is 150 nmi
6	Perform combat air patrol loiter for 20 min at 30,000 ft and best mach for endurance (BCM2)

Mission Segment	Description
7	Accelerate to Mach 0.8
8	Accelerate to Mach 1.2
9	Accelerate to Mach 1.5, total time for acceleration t < 50 s
10	Supersonic Penetration at Mach 1.5 until total distance for accel + supersonic penetration is 100 nmi, supercruise if possible (no afterburning)
11	Combat segment: perform 360 degree, 5 g sustained turn at 30,000 ft, M = 1.6
12	Combat segment: perform two 360 degree, 5 g sustained turns at 30,000 ft, M = 0.9
13	Combat Segment: Accelerate from Mach 0.8 to Mach 1.0 in max power
14	Combat Segment: Accelerate from Mach 1.0 to Mach 1.2 in max power
15	Combat Segment: Accelerate from Mach 1.2 to Mach 1.6 in max power
16	Combat segment: drop payload of 2 AIM-9L's and 250 rds of 25mm ammunition (1309 lb)
17	Escape dash at M = 1.5 and 30,000 ft for 25 nmi, supercruise if possible
18	Climb/decelerate to BCM and BCA at military power, no distance credit
19	Subsonic cruise at best cruise mach (BCM3) and best cruise altitude (BCA2) until total distance is 150 nmi from escape dash
20	Loiter for 20 minutes at 10,000 ft and best mach for endurance (BCM4)
21	Descend and land

Now, in order to deal with the computationally limited results found, results obtained from the first ILGO iteration are extrapolated to obtain a theoretical optimal solution had the optimization had been allowed to continue. The percent-improvement achieved for these extrapolated iterations are based on previous results obtained by Rancruel[20], Rancruel and von Spakovsky[21,22,23], and von Spakovsky [14]. The first ILGO iteration objective functions results as well as the extrapolated results appear in Table 2.9. As can be seen, 35.7% of the total improvement in gross takeoff weight occurs in the first ILGO iteration with an additional 8.4% occurring in the second ILGO iteration.

Finally, a mapping of the exergy losses per subsystem is seen in Figure 2.14. It is obvious that in terms of exergy destruction and loss that the largest amount of irreversibilities occur in the AFS-A and PS due primarily to the fact that they consume the largest amount of exergy in the AAF. Nonetheless, the destruction and loss in the other components is not negligible. In fact, these other subsystems play a vital role in how the AAF flies its mission and, thus, in the synthesis/design of the AFS-A and PS.

Table 2.9. Extrapolated nine-subsystem AAF gross takeoff weight and empty weight versus ILGO iteration based on the ILGO progression from Rancruel.[31,32]

Smith, K. W., *Morphing Wing Fighter Aircraft Synthesis/Design Optimization*, M.S. Thesis, adviser: M. R. von Spakovsky, Department of Mechanical Engineering, Virginia Tech, Blacksburg, VA, 2009. Used with the permission of Kenneth W. Smith, 2012.

ILGO #	W_{TO} (lb_m)	% Improvement	W_{Empty} (lb_m)	% Improvement
0	60000.0	--	39665.5	--
1	38599.5	-35.70%	25517.8	-35.70%
Extrapolated Results				
2	33590.4	-13.00%	20508.7	-19.60%
3	31822.5	-5.30%	18740.8	-8.60%
4	30791.2	-3.20%	17709.5	-5.50%
5	30496.5	-1.00%	17414.9	-1.70%
6	30054.6	-1.40%	16972.9	-2.50%
7	29995.6	-0.20%	16913.9	-0.30%

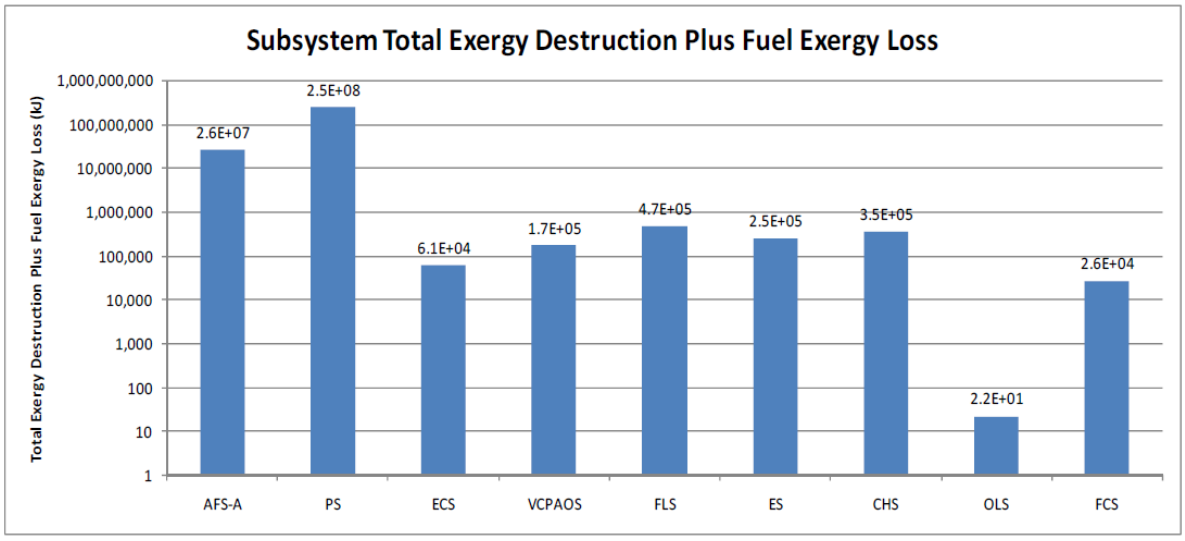

Figure 2.14. Total exergy destruction plus fuel exergy loss for each of the nine subsystems after the first ILGO iteration.[31]

Smith, K. W., *Morphing Wing Fighter Aircraft Synthesis/Design Optimization*, M.S. Thesis, adviser: M. R. von Spakovsky, Department of Mechanical Engineering, Virginia Tech, Blacksburg, VA, 2009. Used with the permission of Kenneth W. Smith, 2012.

2.1.5 Development of Global Exergy Balance Equations for Aerospace Systems

Several of the aforementioned authors have applied exergy concepts to aircraft analysis and optimization. However, work by Riggins[35] has shown that a significant amount of exergy destruction occurs in the wake of the aircraft, as the exhaust mixture coming out of the nozzle equilibrates with the free stream air. To account for exergy destruction in the wake, Riggins developed an overall, 'total vehicle', balance equation which relates flight performance to exergy destruction, i.e.,

$$F_{\text{x(flight)}} \cdot u_i = \dot{m}_f \left\{ H^* + \frac{u_i^2}{2} \right\} - T_i \left(\dot{S}_{\text{vehicle-irr}} + \dot{S}_{\text{wake}} + \dot{S}_{\text{tanks}} \right) \tag{2.1}$$

Where F_x is the net axial force on the vehicle in the direction of flight, u_i is the vehicle's velocity, $\dot{m}_f$ is the fuel flow rate, T_i is the ambient temperature, and $\dot{S}$ is the entropy generation rate. In this balance H^* is the chemical exergy associated with the fuel that takes into account deviation from the tabulated lower heating value (LHV) at non-standard atmospheric conditions. The chemical exergy is defined as

$$\begin{aligned} \dot{m}_f H^* = \dot{m}_f & \left\{ h_{0(f)} + \int_{T_{ref}}^{T_f} c_{p(f)}(T')dT' \right\} - T_i \dot{S}_{fuel} \\ & - \dot{m}_w \sum_{l=1}^{NS} \alpha_{l,w} \left[h_{l,w} - T_i s_{l,i\backslash w}(T_i, P_i, y_{lw}) \right] \\ & + \dot{m}_i \sum_{l=1}^{NS} \alpha_{l,i} \left[h_{l,i} - T_i s_{l,i}(T_i, P_i, y_{li}) \right] \end{aligned} \tag{2.2}$$

Where the α_i are the mass fractions of each constituent, s_i and h_i are the entropy and enthalpy of each constituent, respectively, the y_i are the mole fractions of each constituent, and subscripts *w* and *i* distinguish between flow entering and leaving the control volume.

Figure 2.15 demonstrates that increasing the size of the control volume encompassing the vehicle and its wake increases, the computed net force on the vehicle, and subsequently H^*, asymptotically approaches a limit.

Due to the fact that the net force on the vehicle over the entire mission is zero, integrating the balance equation over time causes the left-hand side of the equation to vanish, yielding the new balance equation given by

$$m_f \left\{ H^* + \frac{u_i^2}{2} \right\} = T_i \left(S_{\text{vehicle-irr}} + S_{\text{wake}} + S_{\text{tanks}} \right) \tag{2.3}$$

Thus, it is possible to say with certainty that entropy generation (and consequently, total exergy destruction) for the total vehicle (i.e., vehicle subsystems and wake) is minimized when the total fuel consumption is minimized.

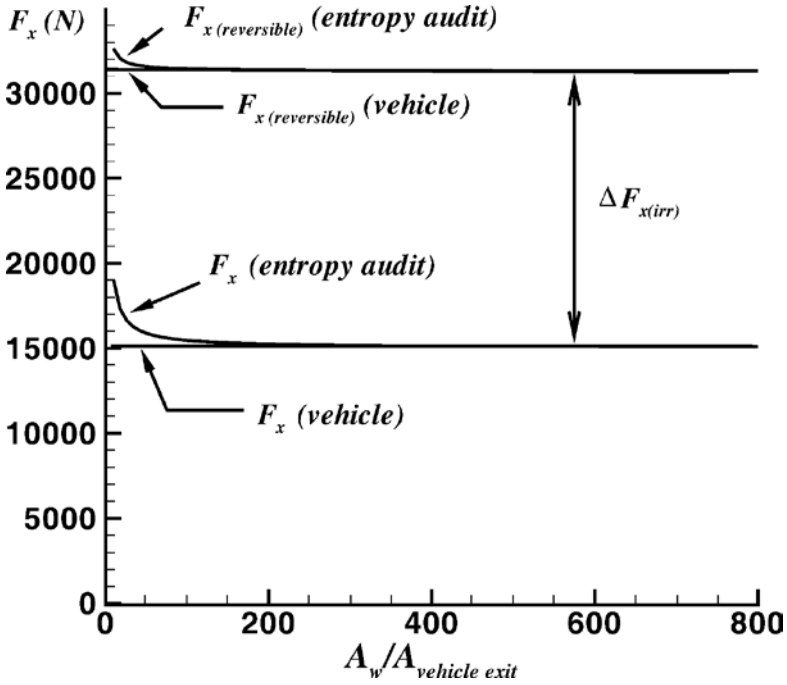

Figure 2.15. Comparison between the axial force Fx on a simplified hypersonic vehicle computed using the standard aerodynamic approach and that computed using the global exergy balance of equation (2.1).[35]
Riggins, D. W., Moorhouse, D. J., Camberos, J. A., 2011, *Exergy Analysis and Design Optimization for Aerospace Vehicles and Systems: Entropy Generation and Aerospace Vehicle Performance*, Progress in Astronautics and Aeronautics, Vol. 238. Used under fair use, 2012.

2.2 INVENT Program

2.2.1 Purpose of the Tip-to-Tail Model as Defined by the INVENT Program

Significant thermal management challenges exist in modern aircraft, which left unresolved, can be of significant detriment to the performance of the vehicle. As described by the INVENT MRIP, a primary goal of the INVENT program and the tip-to-tail model is confrontation and

mitigation of these thermal management issues through system- as well as mission-integrated optimization and trade studies.[5] If successful, the INVENT program is intended to serve as a model for future aircraft development programs.

A part of the optimization and parametric study process is the establishment of appropriate performance metrics, or objective functions. As detailed in Section 2.1, exergy destruction minimization has been shown to be a particularly useful objective. In order to use exergy destruction minimization as a performance metric, exergy balance equations must be implemented in each subsystem. This is beneficial for two reasons. Firstly, exergy balances ensure that all model subsystems have been correctly implemented. If exergy is being created in a subsystem component, the model is incorrect. Secondly, by implementing exergy balances in all model subsystem components it is possible to catalogue the location and magnitude of all irreversibilities present in the system. In this way, designers can see which subsystem components contribute most significantly to the total exergy destruction and can, thus, focus on improving the performance of that specific component. For these reasons, the INVENT program advisors have encouraged INVENT contributors to incorporate exergy analysis into all subsystem component models.

The MRIP emphasizes the importance of implementing transient thermodynamic balances within the tip-to-tail. Transient effects for large thermodynamic systems, such as a fighter aircraft, are typically slow. However, the effect of including transient balances on the performance of an aircraft model is largely unexplored and an area of interest. Additionally, high energy weapons have been shown to produce large, high-frequency transient effects that are missed in steady state analysis. Gvozdich[4] and Gvozdich, Weise, and von Spakovsky[36] investigate the integration of a high energy DEW into the AFRL tip-to-tail model and showed that transient effects are indeed significant, and if not properly managed, can exceed the thermal capacity of modern thermal management subsystems.

2.2.2 Tip-to-Tail Modeling and Simulation

2.2.2.1 Thermal Analysis of an Integrated Aircraft Model

The PTMS is an integral part of the INVENT tip-to-tail model and is used to manage the thermal loads on the aircraft. Bodie et al.[8] performed simple trade studies using a high-fidelity

version of the INVENT tip-to-tail model. Within the PTMS, the primary machinery (air cycle or vapor cycle) used in cooling the hot fluid streams is modeled and the performance is perdicted. Two air cycles and one vapor cycle are tested within the PTMS.

The tip-to-tail model used by the authors includes a 6-DOF AVS model, and as such, runs significantly slower than the tip-to-tail using the drag-polar AVS model. Due to the run-time limitations, the mission profile used in the author's work is altered significantly, to allow Simulink's® ode23s solver to converge to solutions more quickly. The mission profile used in this work is shown in Figure 2.16 below.

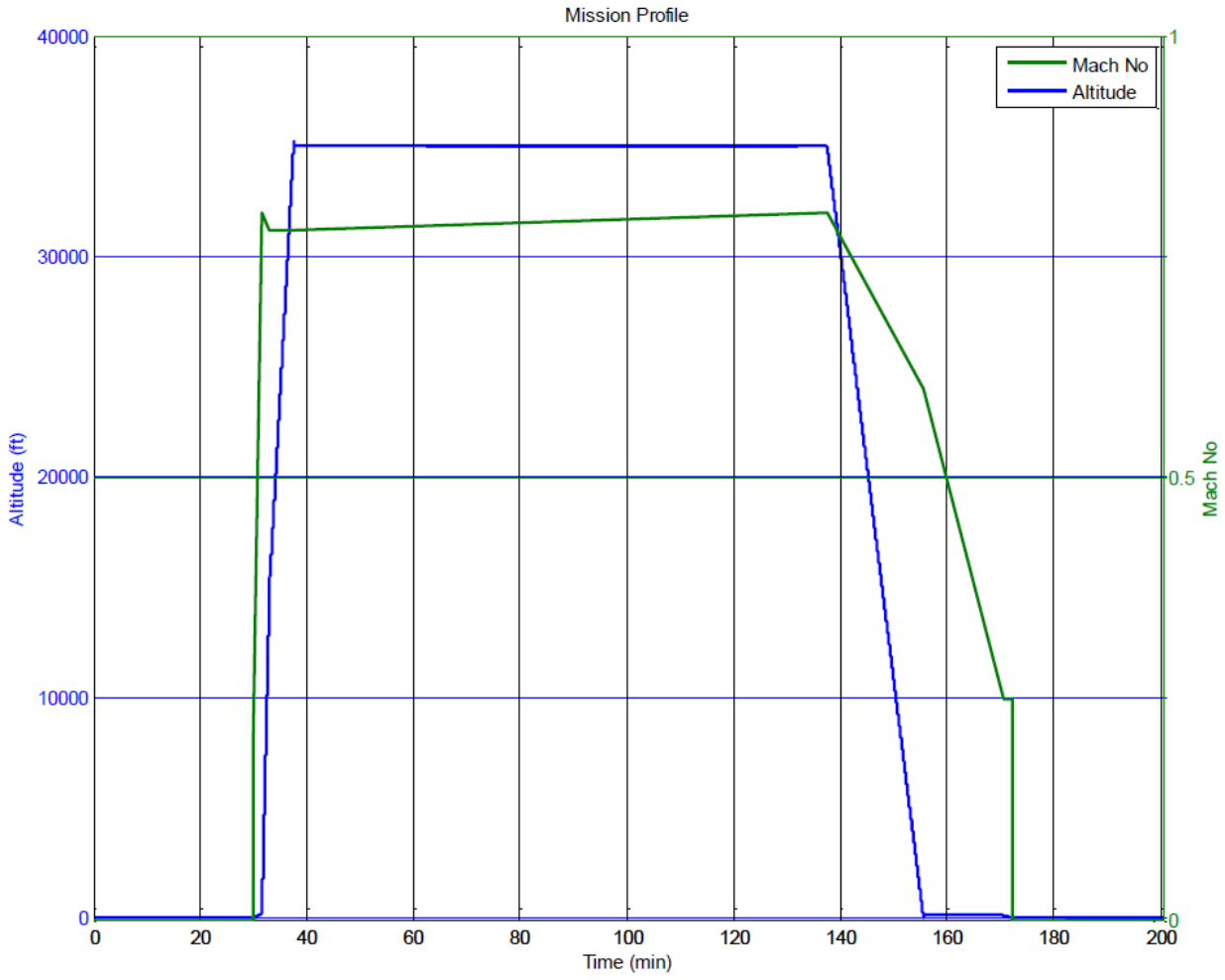

Figure 2.16. Mission profile: altitude and Mach number.[8,c]

[c] This figure is taken from material that is declared a work of the U.S. Government and is not subject to copyright protection in the United States.

Important results from the trade study can be found in Figure 2.17 and Figure 2.18. From these results, important insight into model behavior can be attained. Firstly, note that as seen in the first figure when the vehicle accelerates/climbs and decelerates/descends, the rate of fuel consumption increases. Also, note that as shown in Figure 2.18 fuel temperature increases as the vehicle slows and descends. This effect is most significant in a vapor cycle configuration. These results lead to the conclusion that acceleration/climbs and decelerations/descents are the most taxing segments within a given mission. Furthermore, at low Mach numbers/altitude, where inlet flow rates are limited and the ambient temperature is high, the system may struggle to maintain performance.

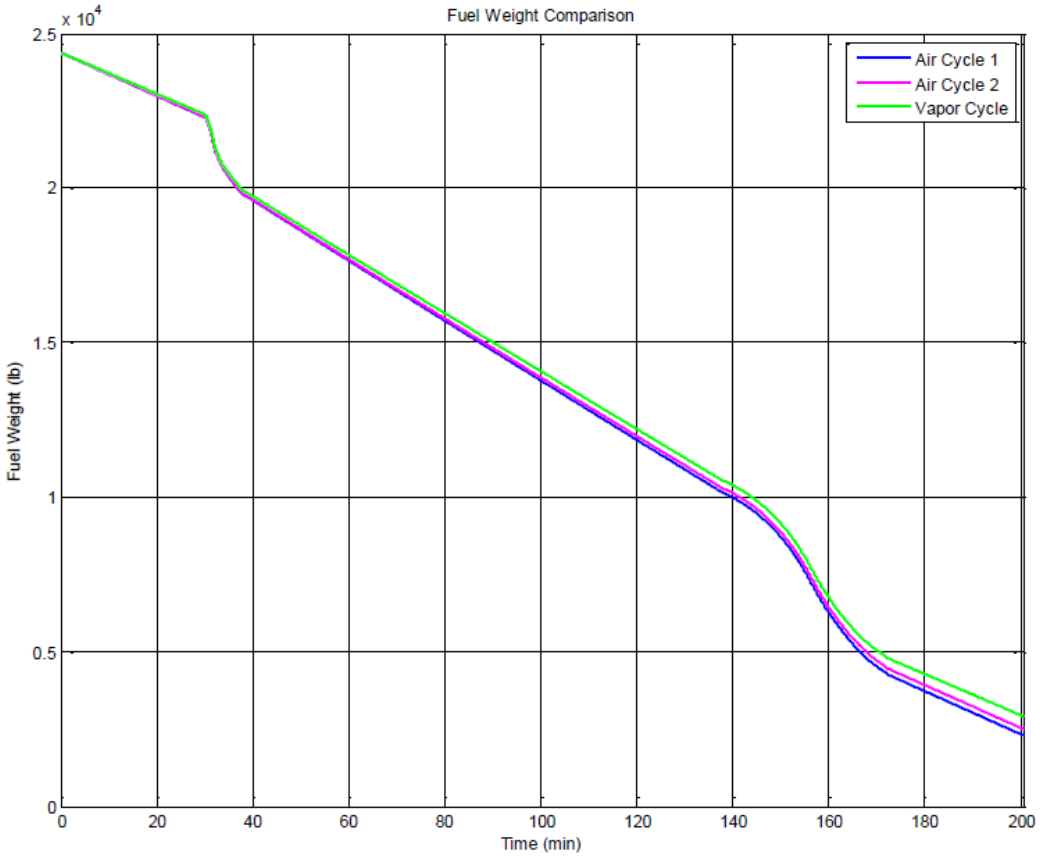

Figure 2.17. Total fuel burn comparison with the PTMS utilizing Air Cycle 1, Air Cycle 2, or the Vapor Cycle.[8,d]

[d] This figure is taken from material that is declared a work of the U.S. Government and is not subject to copyright protection in the United States.

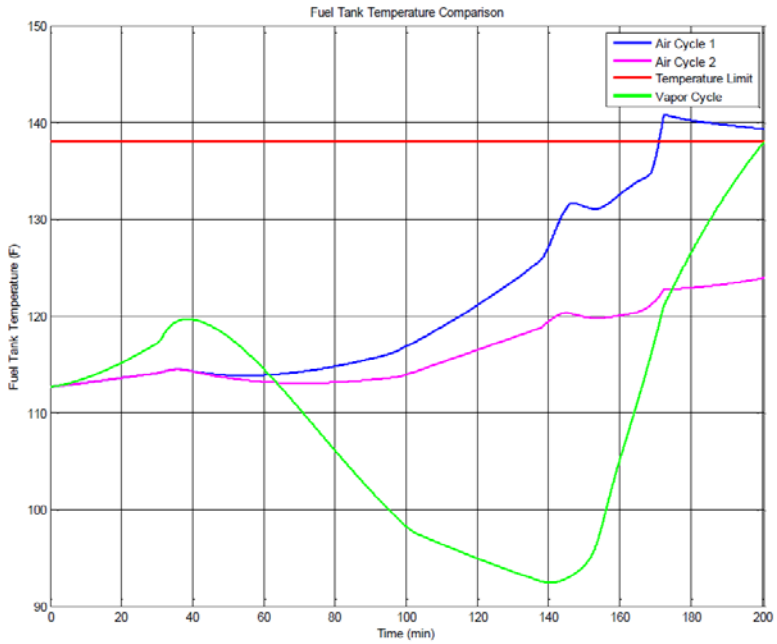

Figure 2.18. Fuel tank temperature comparison with the PTMS utilizing Air Cycle 1, Air Cycle 2, or the Vapor Cycle.[8,e]

2.2.2.2 Modeling and Simulation of a Dynamic Turbofan Engine Using Mathwork's Matlab® Simulink®

Of all the subsystems in the INVENT tip-to-tail model, the PS is the most important. The PS interacts with every other subsystem in the tip-to-tail and, along with the AVS, dictates the performance of the aircraft. Thus, correct implementation of the model equations governing the behavior of the PS is critical. A previous version of the INVENT tip-to-tail model developed in 2010 by Wright State University and Georgia Tech included a basic, steady-state engine model. However, as mentioned previously, capturing the transient effects in the tip-to-tail model is a primary goal of the INVENT program. For this reason, Eastbourn[7] at Wright State University developed a fully dynamic model of a turbofan engine and integrated it into the tip-to-tail model. Model validation was conducted by comparing the results obtained using the transient Wright State engine model to results obtained using a high-fidelity transient AFRL tip-to-tail (T2T) engine model. As shown in Figure 2.19 and Figure 2.20, the transient Wright State engine model behaves similarly to the transient T2T model from the AFRL, with mildly significant deviations

[e] This quote is taken from material that is declared a work of the U.S. Government and is not subject to copyright protection in the United States.

in the fuel consumption occurring only towards the end of the mission sequence. Deviations in the fuel temperature exist across the entire mission, but are never more than 2 °F.

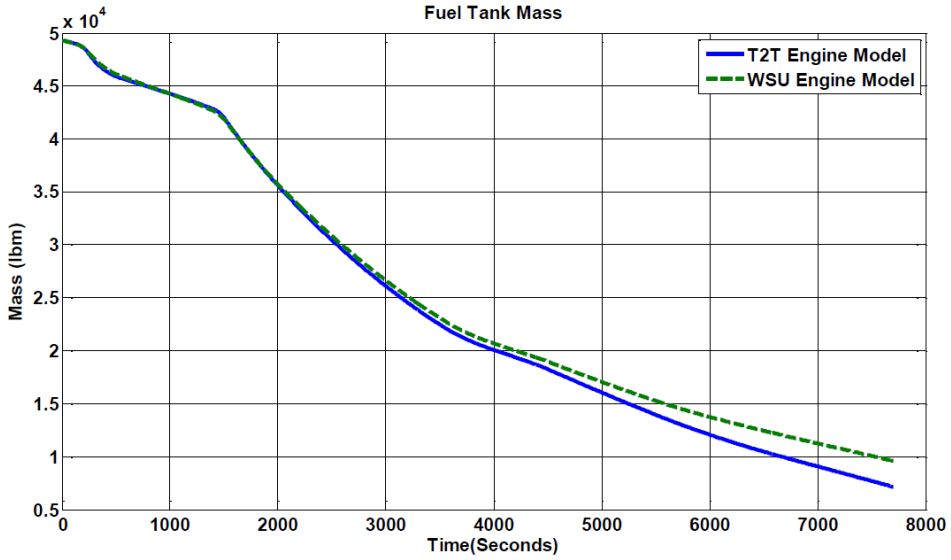

Figure 2.19. Fuel burn comparison between engine models.[7]
Eastbourn, S. M., *Modeling and Simulation of a Dynamic Turbofan Engine Using Matlab/Simulink*, M.S. Thesis, adviser: R. Roberts, Department of Engineering, Wright State University, Dayton, Ohio, 2012. Used with the permission of Scott M. Eastbourn, 2012.

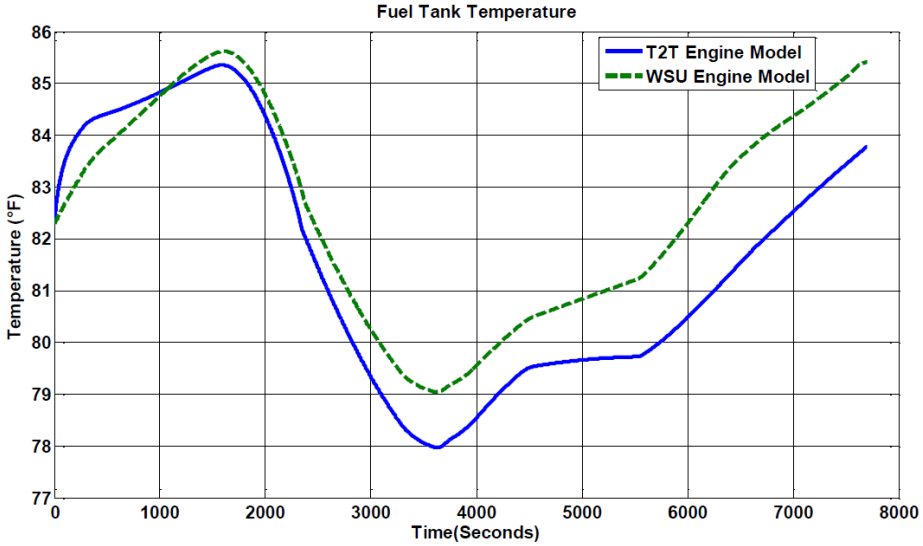

Figure 2.20. Fuel temperature comparison between engine models.[7]
Eastbourn, S. M., *Modeling and Simulation of a Dynamic Turbofan Engine Using Matlab/Simulink*, M.S. Thesis, adviser: R. Roberts, Department of Engineering, Wright State University, Dayton, Ohio, 2012. Used with the permission of Scott M. Eastbourn, 2012.

Within the INVENT tip-to-tail model, one of the most important components, other than those of the PS and AVS, is the Integrated Power Pack (IPP) existing as part of the APTMS. The IPP is a compressor/turbine system the extracts work from the high pressure bleed air stream extracted from the engine. The IPP powers a closed loop air cycle that cools both the cockpit and avionics. Strict constraints are imposed on the performance of the IPP, because if the IPP underperforms, the consequences are dire:

- Elevated temperatures in the cockpit can overheat the pilot, impairing his/her ability to fly and, in extreme cases, could cause heat stroke or death.
- Elevated avionics temperatures can create conditions where components could prematurely fail, jeopardizing the life of the pilot and the success of the mission.

Thus, examining different IPP configurations and comparing performance is of value. In the Eastbourn's[7] work, three specific cases are examined. In case one, a power turbine IPP is examined. In this configuration, the IPP uses bleed air extracted from the engine to power a compressor/turbine system that generates energy used to power the cooling system. The second case is of a configuration with a variable-speed electric motor IPP used to power the cooling loop. In case three, a fixed-speed electric motor IPP is used to power the cooling loop. Results for all three cases are shown in Figure 2.21 and Figure 2.22. As is seen in the first figure, the IPP with the variable-speed electric motor does the best in maintaining the temperature of the avionics. In contrast, in Figure 2.22, it is the IPP with the fixed-speed electric motor which is best at maintaining the temperature of the cockpit.

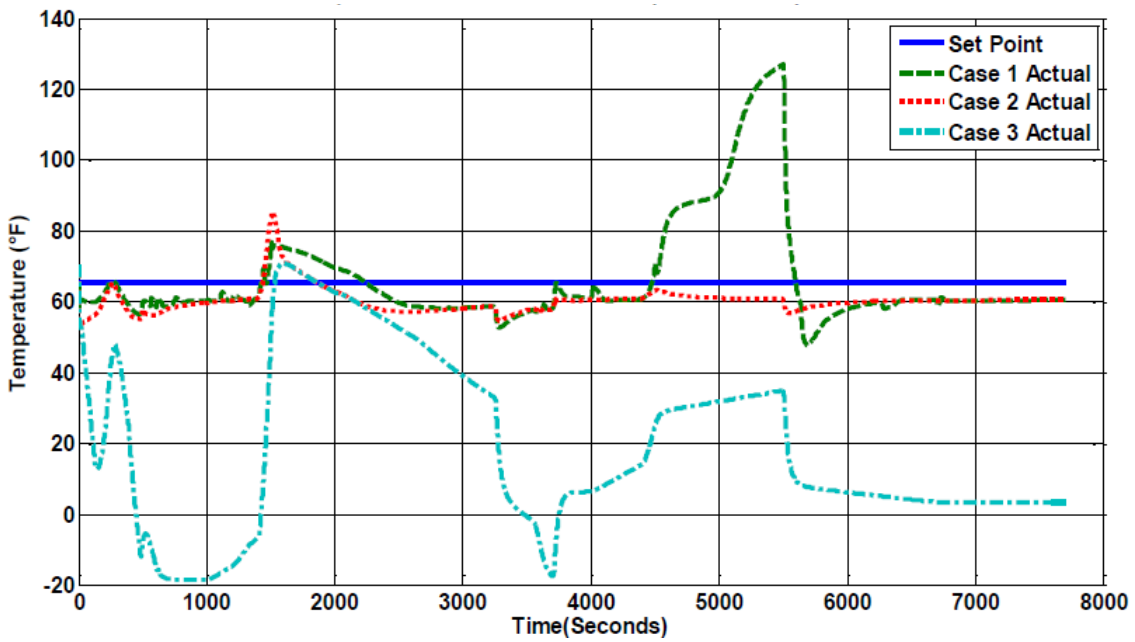

Figure 2.21. Liquid cooled avionics inlet temperature comparison.[7]

Eastbourn, S. M., *Modeling and Simulation of a Dynamic Turbofan Engine Using Matlab/Simulink*, M.S. Thesis, adviser: R. Roberts, Department of Engineering, Wright State University, Dayton, Ohio, 2012. Used with the permission of Scott Eastbourn, 2012.

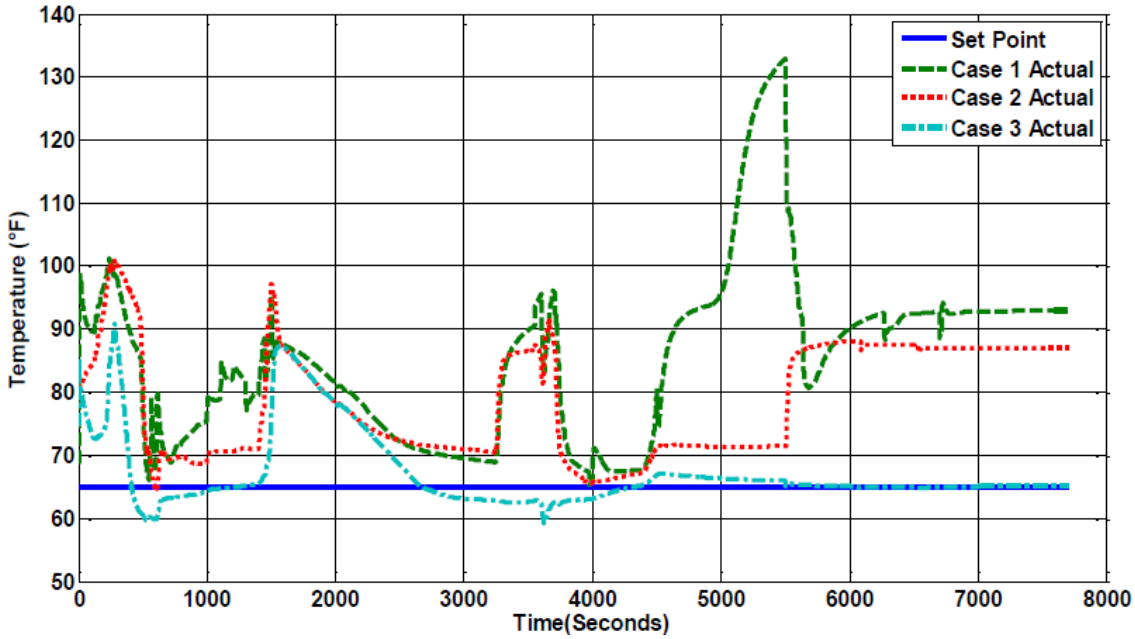

Figure 2.22. Cockpit exit temperature comparison.[7]

Eastbourn, S. M., *Modeling and Simulation of a Dynamic Turbofan Engine Using Matlab/Simulink*, M.S. Thesis, adviser: R. Roberts, Department of Engineering, Wright State University, Dayton, Ohio, 2012. Used with the permission of Scott Eastbourn, 2012.

Notice that for both the cockpit exit temperature and liquid cooled avionics inlet temperature, in all three cases the upper limit is violated at some point in the mission. This reinforces the concept that current and future vehicles are limited by how effective the thermal management solutions are. It is expected that optimization of the tip-to-tail will increase the performance of the tip-to-tail and increase the efficacy of the thermal management subsystems.

2.3 Heat Exchanger Modeling and Simulation in INVENT

2.3.1 Types of Compact Heat Exchangers

Compact heat exchangers exist in a variety of forms and configurations for many different applications. The descriptions given are generic and within each class, variants by manufacturer and class exist. Some of the most common types of compact heat exchangers include

- Plate-fin heat exchanger
- Tube-fin heat exchanger
- Diffusion-bonded heat exchanger
- Plate-frame heat exchanger
- Plate-shell heat exchanger

2.3.1.1 Plate-Fin Heat Exchanger (PFHE)

The plate-fin heat exchanger may be the most common of all heat exchangers due to its high performance and low cost of production. Plate-fin heat exchangers are characterized by their fin structures and flow separation plates. Fin structures found in plate fin heat exchangers are diverse and include, as depicted in Figure 2.23,

- Plain rectangular fins (a)
- Plain triangular fins (b)
- Wavy fins (c)
- Offset strip fins (OSF) (d)
- Perforated fins (e)
- Louvered fins (f)

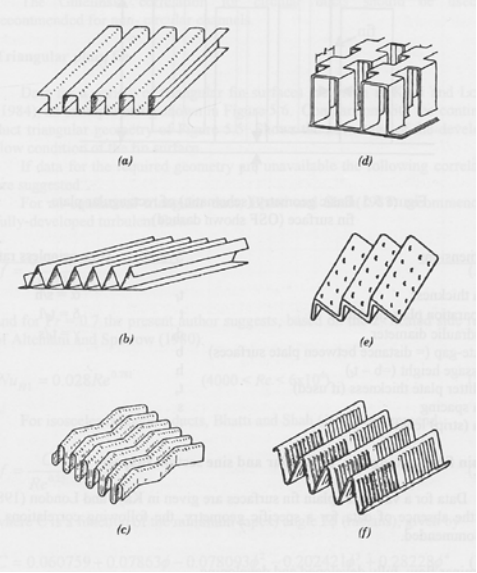

Figure 2.23. PFHE fin geometries.[37]
Hesselgreves, J. E., 2001, *Compact Heat Exchangers: Selection, Design and Operation* (1st ed.). Oxford: Elsevier. Used under fair use, 2012.

2.3.1.2 Tube-Fin Heat Exchanger

Tube-fin heat exchangers are constructed of tubes expanded onto fins to create thermal contact. They are often used in locomotive radiators and steam condensers. Examples of plate-fin and tube-fin heat exchangers can be found in Figure 2.24.

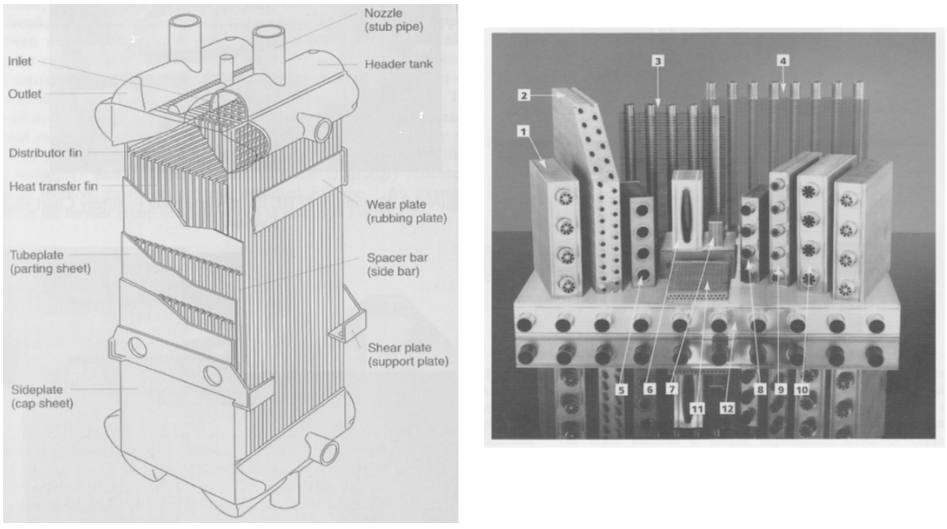

Figure 2.24. Examples of Plate-Fin (*left*) and Tube-Fin (*right*) heat exchangers[37]
Hesselgreves, J. E., 2001, *Compact Heat Exchangers: Selection, Design and Operation* (1st ed.). Oxford: Elsevier. Used under fair use, 2012.

2.3.1.3 Diffusion-Bonded Heat Exchanger

Diffusion-bonded heat exchangers are used in applications where it is critical that heat exchanger material be homogeneous. Diffusion-bonded heat exchangers are often constructed by stacking and compressing grooved plates and heating the assembly until the plates have diffused together. These heat exchangers can have very detailed geometry and small hydraulic diameters. A single plate layer used to construct a diffusion-bonded heat exchanger can is seen in Figure 2.25.

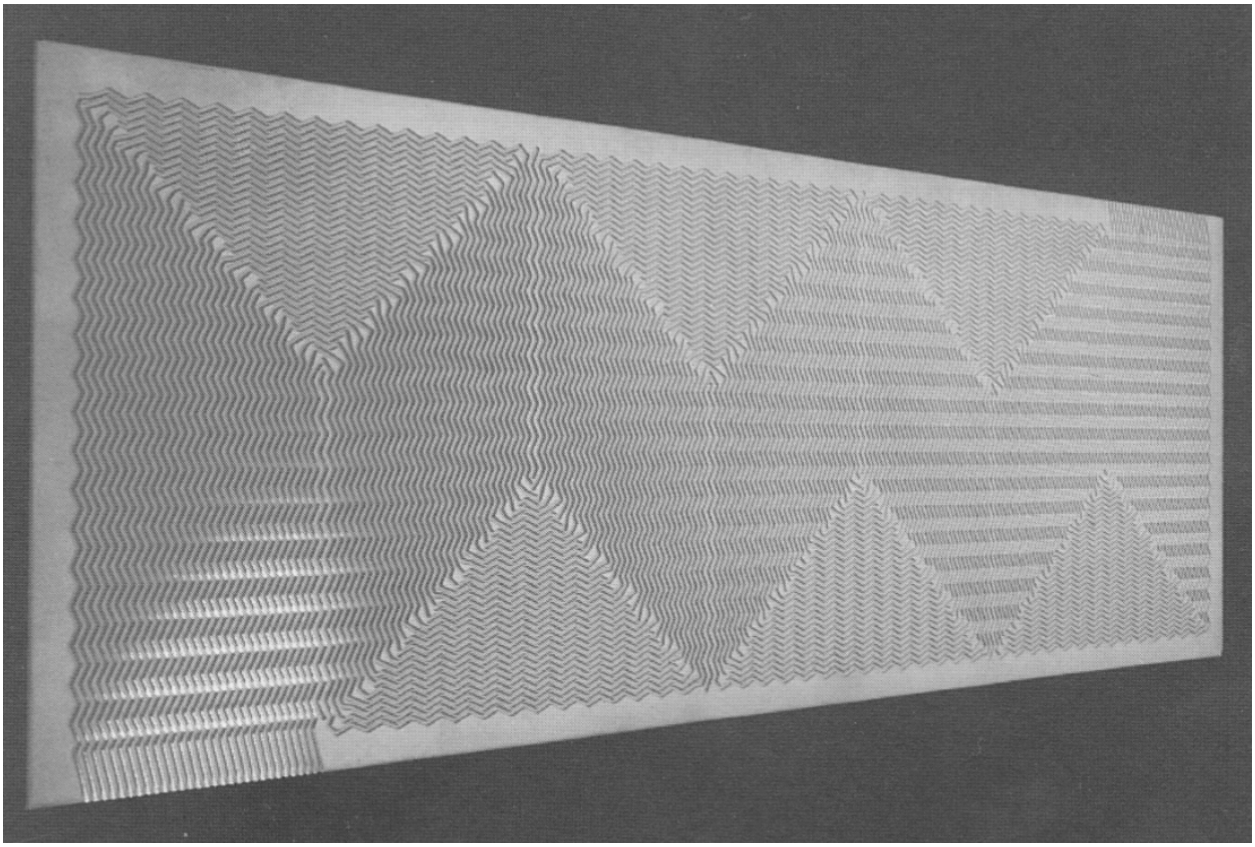

Figure 2.25. Single plate of a diffusion-bonded heat exchanger. Multiple plates are layered, compressed, and heated to diffuse plates together. [37]
Hesselgreves, J. E., 2001, *Compact Heat Exchangers: Selection, Design and Operation* (1st ed.). Oxford: Elsevier. Used under fair use, 2012.

2.3.2 Heat Exchanger Sizing, Modeling, and Simulation in the Literature

Creating an accurate heat exchanger model can be an arduous process. While there are several excellent resources for information regarding heat exchanger characteristics, much of the data that could be used to validate a heat exchanger model is proprietary. As such, it is often the case that the way to validate a model is to compare general behavior and not actual numbers. Thus, when developing heat exchanger models, it is important to use the best correlations and modeling techniques available. Several excellent sources exist for information on modeling and sizing heat exchangers, including Kays and London[38], Shah[39], Kakaç[40], and Hesselgreaves[37].

Hesselgreaves[37], outlines a general sizing technique for counter-flow heat exchangers that is used in this thesis work. The technique is divided into two stages as follows:

Stage 1: Scoping size

- From a given thermal specification, calculate heat exchanger effectiveness.
- From the heat capacity rate, $\dot{m}c_p$, for both sides with the knowledge of the fluids, calculate the ratio of heat capacity rates.
- Estimate the overall Ntu (Number of thermal units)
- Calculate the Ntu for each side.
- Calculate the mass velocity, G, for each side based on an initial estimate of the Ntu for each side and an initial guess for the pressure drop.
- Based on the fin characteristics and design flow rates, calculate the Reynolds number for each side.
- Calculate the overall heat exchanger length for each side.

Stage 2: Counter-flow design

- Calculate the geometric mean of the lengths calculated in the previous stage.
- Calculate a new pressure drop
- Calculate a new effectiveness and overall Ntu.
- Compare the calculated effectiveness with the desired effectiveness.
- Calculate a new overall heat exchanger length and iterate until the effectiveness converges.

Due to the transient nature of the heat exchangers in this thesis work, an altered design process derived from the process outlined by Hesselgreaves is used and described in detail in Chapter 3.

2.3.3 OSF Compact Heat Exchanger Modeling

The transient heat exchanger model developed in this thesis work in collaboration with Gvozdich[4] and used in the INVENT tip-to-tail model represents an OSF compact heat exchanger. OSF compact heat exchangers can be adapted to a variety of conditions and can tolerate liquid-liquid, liquid-gas, and gas-gas flows, as well as reacting flows and high-pressure flows. As such, nearly every heat exchanger found in the tip-to-tail can be modeled as an OSF compact heat exchanger without loss in fidelity.

2.3.3.1 Aspects of Heat Exchanger Compactness

When discussing compact heat exchangers, it is useful to consider what distinguishes compact heat exchangers from all others. Traditionally, there are two parameters that define compactness of heat exchangers: surface area density and hydraulic diameter. Heat exchanger surface area density, β, is defined as the ratio of surface area to surface volume (submerged volume), i.e.,

$$\beta = \frac{A_s}{V} \tag{2.4}$$

Typically, for a heat exchanger to be considered a compact heat exchanger, the surface area density must be greater than 700 m^2/m^3.[37]

Hydraulic diameter is another commonly used parameter in measuring the degree of heat exchanger compactness. Usually, hydraulic diameters for compact heat exchangers are less than 5 mm. The hydraulic diameter for heat exchangers is defined uniquely for each configuration, but can be defined generally as

$$D_h = \frac{4A_c L}{A_s} = \frac{4V_s}{A_s} \tag{2.5}$$

Where L is the characteristic length, A_c is the cross-sectional area of the flow, A_s is the surface area, and V_s is the volume of the fluid in the heat exchanger.

2.3.3.2 Use of Compact Heat Exchangers in Industry

Compact heat exchangers are widely used in a variety of industries including the refrigeration, automotive, and aerospace industries. Within the refrigeration industry, shell and tube heat exchangers are used in applications of large scale due to their low cost of production and easy maintenance. In smaller applications, heat exchangers such as the brazed-plate heat exchanger may be used. In the air conditioning industry, where size constraints often exist, tube-fin heat exchangers are used for evaporation or condensation.

Within the automotive industry, rapid production, low cost, and high performance are critical; and, thus, tube-fin heat exchangers are often used. For example, typical of automotive radiators is the use of louvered fins (or other fin type), coupled with a flat tube surface.

In the aerospace sector, a wide variety of heat exchangers are used in a large number of ways. Due to high performance-to-weight ratio constraints, as well as low production numbers, heat exchanger costs in this industry tend to be higher than in other industries. Primary heat exchanger uses include oil cooling or fuel preheating for which shell and tube units are often used as well as environmental control for which plate-fin heat exchangers are used.

2.3.4 Updated Transient Heat Exchanger Model Developed Here and Previously Implemented

The heat exchanger model developed as part of this thesis work describes the development of a transient model of an OSF compact heat exchanger. This model was incorporated into the INVENT tip-to-tail as part of the work on DEW integration by Gvozdich.[4] The model uses the discretization scheme demonstrated in Figure 2.26. While only three nodes are shown in the figure, the model allows for the expansion to an arbitrary number of nodes at the expense of increased simulation time. At each node, conductive and convection heat transfer modes are modeled using transient thermodynamic energy balances. Heat exchanger physical parameters such as mass, volume, and surface area are determined using the iterative sizing algorithm described in Chapter 3 of this thesis.

The compact heat exchanger is integrated into the HPTMS where it is used to manage thermal loads produced by the DEWS developed by Gvozdich.[4] This HPTMS was subsequently

integrated into the FTMS in the INVENT tip-to-tail. Gvozdich showed that the FTMS has the largest capability to manage the significant thermal loads produced when the DEW fires. A schematic of the DEW integrated into the FTMS is shown in Figure 2.27.

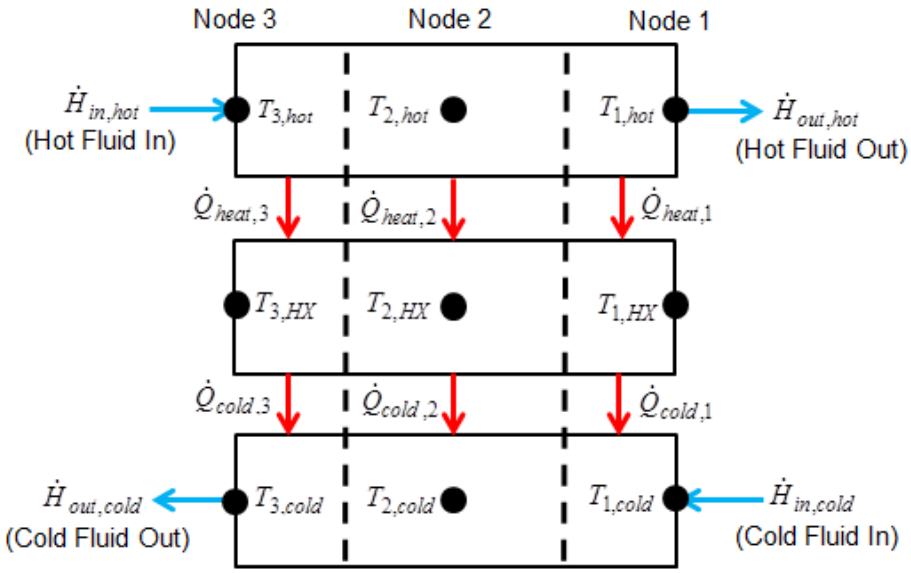

Figure 2.26. Discretization scheme used in the compact heat exchanger model.[4]
Gvozdich, G., *Modeling the Effects of Transient High Energy Weapon Subsystems on High-performance Aerospace Systems*, M.S. Thesis, adviser: M. R. von Spakovsky, Department of Mechanical Engineering, Virginia Tech, Blacksburg, Virginia, 2011. Used with the permission of Grant G. Gvozdich, 2012.

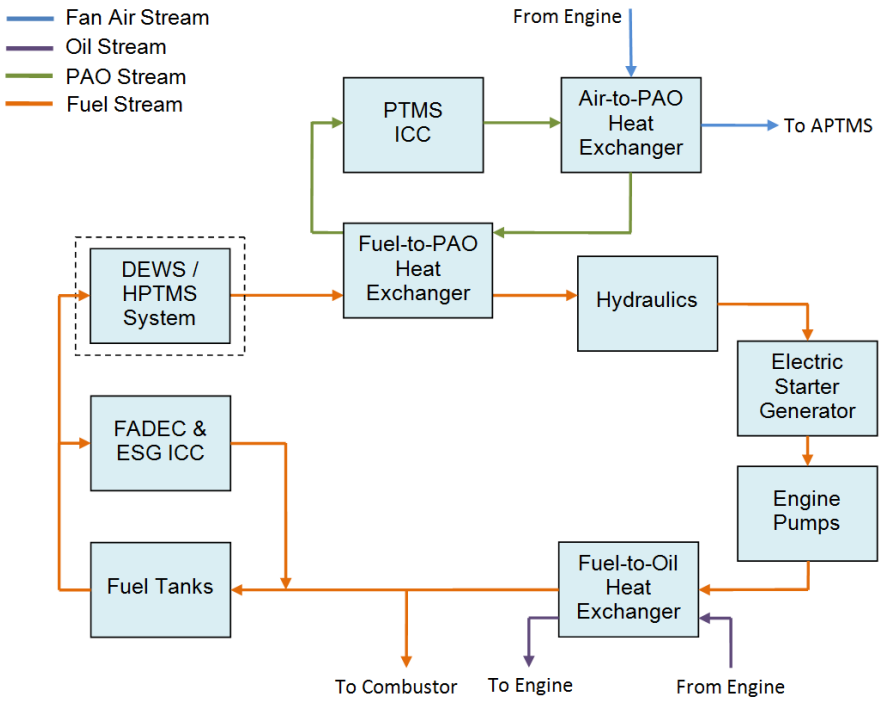

Figure 2.27. Schematic of the DEW integrated into the FTMS.[4]
Gvozdich, G., *Modeling the Effects of Transient High Energy Weapon Subsystems on High-performance Aerospace Systems*, M.S. Thesis, adviser: M. R. von Spakovsky, Department of Mechanical Engineering, Virginia Tech, Blacksburg, Virginia, 2011. Used with the permission of Grant G. Gvozdich, 2012.

The heat exchanger model discussed here is integrated into the tip-to-tail in multiple locations within the APTMS and the FTMS. As such, a more rigorous discussion of the heat exchanger model follows in Chapter 3.

2.4 Benefits and Challenges of Large-Scale Surrogate Based Analysis and Synthesis/Design Optimization

2.4.1 Large-Scale Synthesis/Design Optimization

Large-scale synthesis/design optimization is a vital tool for the aerospace research/design community. If correctly implemented, large-scale synthesis/design optimization provides a set of parameters that optimize a specific objective function. In the aerospace community, typical objectives include minimizing fuel usage and maximizing performance or safety. In multi-objective large-scale synthesis/design optimization, where several objectives are utilized, a

Pareto frontier is established. This Pareto frontier describes a set of Pareto-optimal solutions, as opposed to a single optimum solution. A solution can be described as Pareto-optimal if there is no other solution which can improve upon one of the objectives without detriment to the other objectives. By assigning weights to each objective function, a specific optimal solution can be chosen from the Pareto-optimal set that best meets the design requirements. Whether or not the optimization is based on a single or multiple objectives, large-scale optimization is a computationally intensive process which must be unburdened in whatever way possible without significant loss in fidelity.

2.4.2 Addressing the Computational Problem

SBAO has proven to be effective in addressing the computational burden imposed by large-scale analysis and optimization. For example, for the case of the liquid rocket injector[41], completing a single simulation requires running a complex computational fluid dynamics (CFD) code. Increasing the fidelity of the CFD mesh incurs a proportional computational cost. To reduce this cost the fidelity of the CFD mesh must be no greater than necessary, but even then to optimize this system the CFD model must be replaced with a surrogate model which must be built with the fewest data points, i.e., CFD simulations, possible.

In a similar fashion, the computational burden encountered when performing optimization on the INVENT tip-to-tail is extremely large. At present, the tip-to-tail model takes approximately 4-5 minutes (in Matlab® Simulink's® Accelerator mode) to complete a single simulation on a quad core Intel i7-2600k overclocked to 4.5 GHz. In order to successfully optimize the tip-to-tail using a reasonably large set of decision variables, surrogate based optimization is the only feasible option, other than reducing model simulation time through either more efficient programming methods or a loss of fidelity.

An example of the computational burden optimization presents can be found in the work of Smith[31]. Smith's synthesis/design optimization of a morphing-wing fighter aircraft used over 734 DOF, presenting a challenging, mixed integer nonlinear programming optimization problem. Although the simulation time was small, it took over two months to perform a single ILGO iteration of many hundreds of thousands of simulations using a genetic algorithm.

2.4.3 Uses of SBAO in the Literature

Queipo et al.[41] illustrate the benefits of utilizing SBAO in the multi-objective design optimization of the liquid rocket injector mentioned in the previous section. As illustrated in Figure 2.28, the four design decision variables for this CFD optimization are flow angle, hydrogen flow area, oxygen flow area, and oxidizer post tip thickness. Additionally, the four objective functions are injector chamber wall temperature, face temperature, combustion length, and injector tip temperature. In order to increase injector life, it is desired that the wall temperature, face temperature, and tip temperature all be minimized. Similarly, to minimize the overall size of the injector, it is desired that the combustion length be minimized. It is noteworthy that due to the strong correlation between injector face temperature and wall temperature, the authors eliminate wall temperature as a design variable. Rather than use computationally burdensome optimization algorithms, (e.g., genetic algorithms, pattern search algorithms, etc.), the authors use Design of Experiments (DOE) and surrogate models to analyze and optimize the system. Figure 2.29 describes the Pareto frontier for the maximum injector face temperature (TF_{max}) versus combustion length (X_{cc}), as well as for the maximum injector face temperature (TF_{max}) versus the maximum injector tip temperature (TT_{max}).

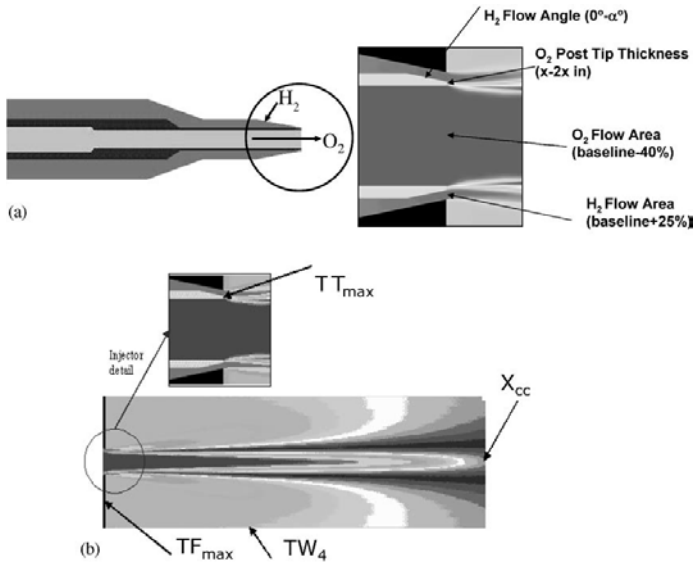

Figure 2.28. (a) Design variables and (b) objectives of the single element rocket injector.[41] Queipo, N. V., Haftka, R. T., Shyy, W., Goel, T., Vaidyanathan, R., Tucker, P. K., *Surrogate-Based Analysis and Optimization*, Progress in Aerospace Sciences 41 (2005), p. 1-28, Oxford: Elsevier. Used with the permission of Elsevier, 2012.

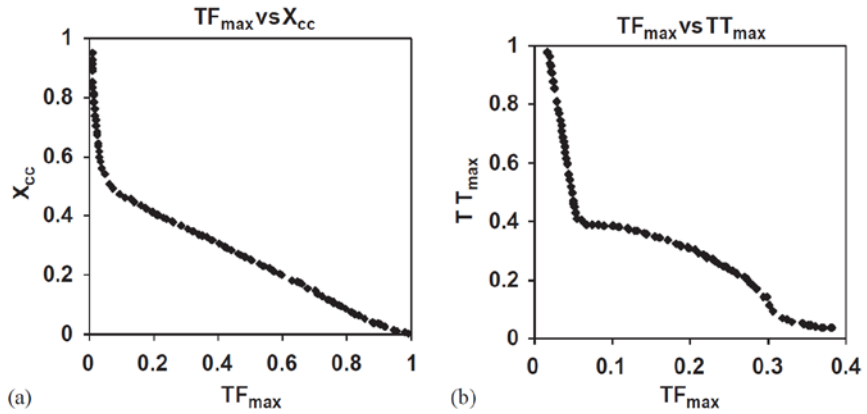

Figure 2.29. Pareto optimal front: (a) maximum injector face temperature vs. combustion length (b) maximum injector face temperature vs. maximum injector tip temperature.[41]
Queipo, N. V., Haftka, R. T., Shyy, W., Goel, T., Vaidyanathan, R., Tucker, P. K., *Surrogate-Based Analysis and Optimization*, *Progress in Aerospace Sciences* 41 (2005), p. 1-28, Oxford: Elsevier. Used with the permission of Elsevier, 2012.

Successful demonstration of SBAO for large-scale synthesis/design optimization has been shown to be effective in dealing with a large variety of problems. Gorissen et al.[42] have successfully used SBAO in the optimization of several unique systems, including a low noise amplifier (LNA), an automotive B-pillar, and combustion. The authors demonstrate that when employing SBAO, it is critically important to select the correct metrics for measuring model accuracy and even more important to select an appropriate method to model the response surface.

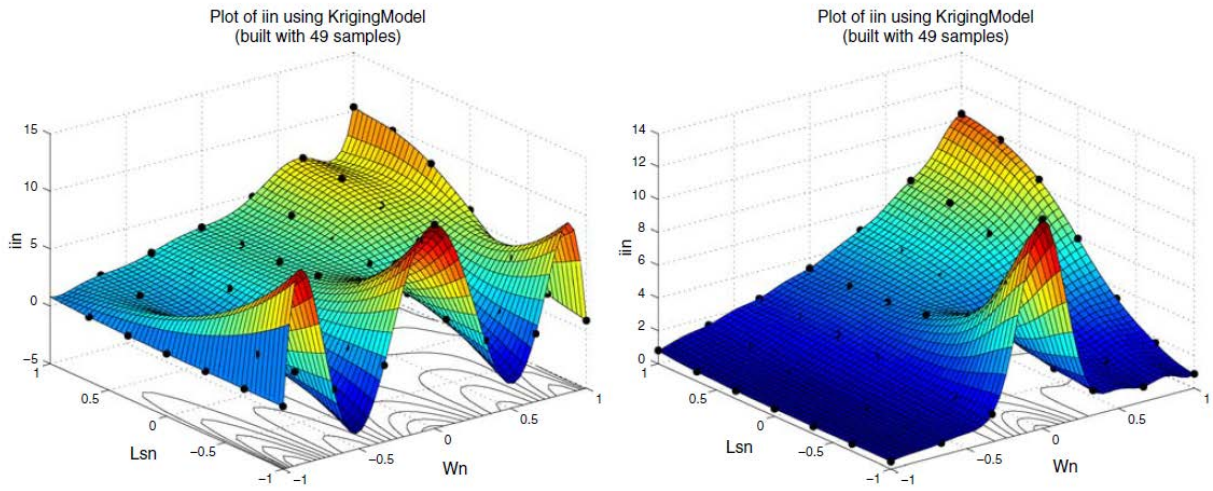

Figure 2.30. Plot of the models at the extreme Pareto points for the LNA problem (minimal validation error [left], minimal smoothness penalty [right]).[42]
Gorissen, D., Couckuyt, I., Laermans, E., Dhaene, T., *Multiobjective Global Surrogate Modeling, Dealing With the 5-percent Problem*, Engineering with Computers (2010) 26:81-98. Used with permission of Springer, 2012.

For the LNA problem, the two inputs are the width of the metal–oxide–semiconductor field-effect transistor (MOSFET)[f], W_n, and the normalized inductance, L_{sn}; and the output is the input noise current, i_{in}. Using a Latin hypercube (LHC) initial design of 15 points and employing an adaptive sampling technique, surrogate models are constructed. Figure 2.30 illustrates that given the same set of data with which to create a surrogate model, using an appropriate error metric will produce superior results. Note that the figure on the left exhibits highly nonlinear behavior in the region $L_{sn} < 0$. This behavior is due to minimizing the error between the model and the data points, and consequently it can be seen that the model fits the given data very well. However, in the regions of oscillatory behavior it is expected that the predictive capabilities of the model will be very poor. On the other hand, while the model on the right, which uses a different error metric, may not fit the given data as well as the model on the left, it is expected that the predictive capability of the model will be significantly better.

[f] A MOSFET is a transistor used for amplifying or switching electronic signals.

2.4.4 Motivation for Using SBAO for the Mission Integrated Synthesis/Design Optimization of a Tip-to-Tail Aircraft Model

The driving force behind the development of new optimization algorithms has been the desire to reduce the time required to solve the optimization problem and to increase the probability of convergence to the global optimum. Commonly used algorithms, such as genetic algorithms or gradient-based algorithms, are limited in the sense that neither can achieve both goals. Wither they achieve the former and not the latter or vice versa.

Genetic algorithms are codes that attempt to mimic Darwin's theory of evolution and natural selection. The first use of genetic algorithms can be attributed to John Holland of the University of Michigan in 1975.[43] The idea is that after an initial feasible model solution is given, called a "parent," the algorithm creates a set of "children" by mutating input parameters of the parent, subsequently weighing them against a fitness function. As in natural selection, the most viable solutions make it through to the next phase and the process repeats. Although genetic algorithms are desirable due to their simplicity, they also have several critical drawbacks.

When dealing with complex systems, a vast quantity of model solutions must be found before iterating. Consequentially, genetic algorithms are very computationally expensive for complex systems; and while convergence to a global optimum is likely, the cost paid in terms of simulation time (i.e., finding model solutions) is very high.

Alternatively, gradient-based algorithms can be used for the optimization of real-valued functions, due to the numerical methods applied in its use. Considering some function one wishes to minimize

$$f(\vec{x}) \quad \text{w.r.t.} \quad \vec{x} \tag{2.6}$$

The iterative algorithm resulting is

$$\vec{x}^{k+1} = \vec{x}^{k} - \alpha^{k} \nabla f\left(\vec{x}^{k}\right) \tag{2.7}$$

In equation (2.7) α is a sufficiently small step size, the choice of which is governed by the choice of numerical algorithm (e.g. Newton's method, conjugate direction method, etc.). The two most popular gradient-based optimization algorithms are the Method of Feasible Directions (MFD)[44] and Sequential Quadratic Programming (SQP)[45]. Gradient-based approaches are convenient in that the typically converge very quickly to an optimal solution. However, the solution is often times a local optimum.

These drawbacks have led the scientific and engineering community to seek new methods for optimizing systems. As a result, the engineering community now has at its disposal optimization tools such as pattern search and surrogate modeling techniques. One such tool is the Matlab® SUMO Toolbox, produced by faculty and students at Ghent University (Gent, Belgium).[46]

The Surrogate Modeling (SUMO) toolbox is a Matlab® toolbox that creates surrogate models based on specified user inputs and the simulation outputs. A surrogate model is created by sampling points all across the domain, using pre-defined parameters as the variables. There are several methods by which SUMO selects sample points (e.g., randomly, error based, density based, etc.). In addition to methods for sample selection, there are also methods used to analyze the behavior of the surrogate model, each of which is tailored to certain types of inputs. The logic flow used to develop surrogate models can be found in Figure 2.31 below.

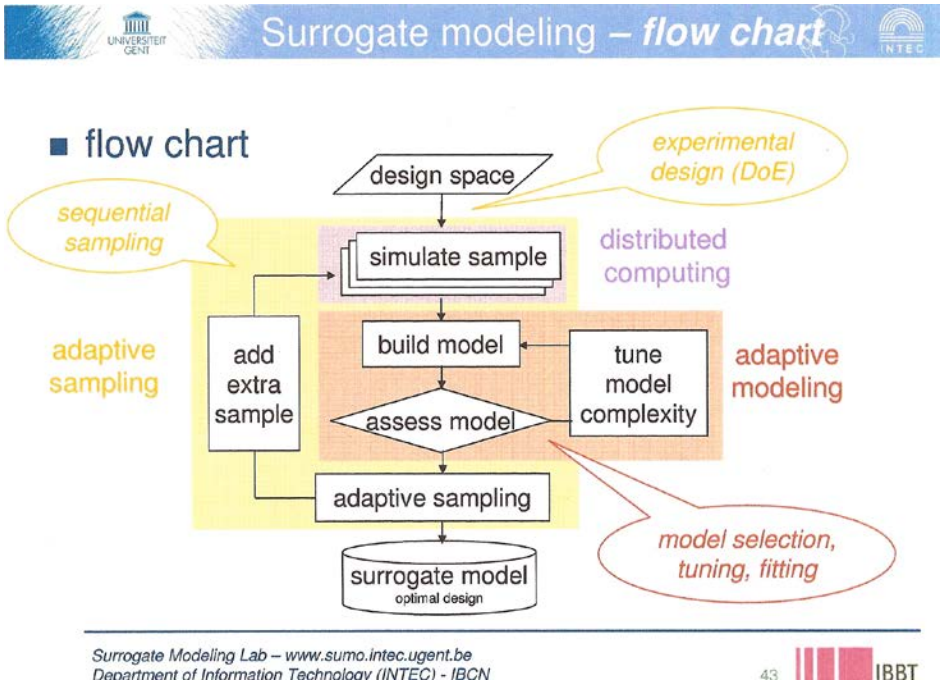

Figure 2.31. Flow of logic used by SUMO.[46]
Gorissen, D., Crombecq, K., Couckuyt, I., Dhaene, T., Demeester, P., *A Surrogate Modeling and Adaptive Sampling Toolbox for Computer Based Design*, Journal of Machine Learning Research, Vol. 11, pp. 2051-2055, Jul. 2010. Used with the permission of Dirk Gorissen, 2012.

A similar, though more polished and user friendly SBAO algorithm, has been developed by Phoenix Integration and distributed as part of their ModelCenter® software. ModelCenter® is

preferred over other SBAO algorithms due to the fact that it easily integrates with many of the popular modeling and design tools used by academia and industry today, including SolidWorks®, ANSYS®, and most importantly Matlab®/Simulink®. Phoenix Integrations provides an algorithm named 'Design Explorer' that uses a hybrid surrogate/gradient based approach. The design explorer algorithm first samples points from the entire design space and constructs an initial surrogate model. Based on an error metric, the algorithm decides if the surrogate is sufficient or if further sampling is needed. Once the surrogate is constructed, a gradient-based optimization algorithm is used in the most promising regions of the design space. Using this methodology increases the probability of converging to the global optimum, while using significantly fewer simulations than that of a genetic algorithm or similar global optimization technique.

Chapter 3 - Tip-to-Tail Model, Heat Exchanger Model, and Sizing Algorithm

3.1 Tip-to-Tail Subsystem Descriptions

As shown earlier in Figure 1.1 of Chapter 1, the aircraft subsystems which make up the INVENT tip-to-tail model consist of six intimately linked subsystems: the HPEAS, REPS, PS, AVS, FTMS, and APTMS. The subsystems are described in detail in the following sections.

3.1.1 Primary Vehicle Subsystems

Unpowered flight is the simplest of all forms of aviation. Unpowered aircraft, such as gliders and kites, use wings, potential energy, and thermally induced updrafts to maintain altitude and velocity. Thus, in the vernacular used in this thesis work, unpowered aircraft need only an AVS to be considered a complete system. Powered flight requires an additional subsystem, the PS, in order to be considered complete. Thus, in powered flight, the aircraft vehicle and propulsion subsystems are termed the primary vehicle subsystems. All other subsystems found in modern aircraft enhance aircraft performance or add auxiliary capabilities to the aircraft.

3.1.1.1 Aircraft Vehicle Subsystem (AVS)

In a military aircraft, the AVS is arguably the most important subsystem. The AVS provides the lift and control surface movement that allows a pilot to fly the aircraft. Additionally, the AVS functions as the housing for all the other subsystems found in the aircraft. Although not the most complicated subsystem, the degree to which it effectively integrates all other subsystem components greatly affects the manner in which the vehicle performs.

The AVS model used in the INVENT tip-to-tail model simulates the vehicle's motion through the air using a simple drag-polar force balance model. A drag-polar model assumes that the airframe can be effectively modeled as a point-mass moving through space. A free-body diagram indicating the forces used to describe the behavior of the system found in Figure 3.1 yields the following force balance

$$\sum F_{\substack{flight-\\direction}} = (T - D) - W \sin\alpha = m\frac{dV}{dt} \tag{3.1}$$

Where F is a force, T the engine thrust, D the drag, W the system weight, α the angle of attack, and V the vehicle velocity. Rearranging and noting that

$$\sin(\alpha) = \frac{1}{V}\frac{dV}{dt} \tag{3.2}$$

yields what is termed by Mattingly et al.[19] as the master flight equation, described in Table 3.1. It is important to note that the drag term in this equation includes both parasitic and lift-induced drag. Parasitic drag consists of several components including form drag, skin friction, and interference drag. Lift-induced drag is the penalty paid to generate lift and is caused by redirecting air around the wings and fuselage. Figure 3.2 shows how total drag varies as airspeed increases.

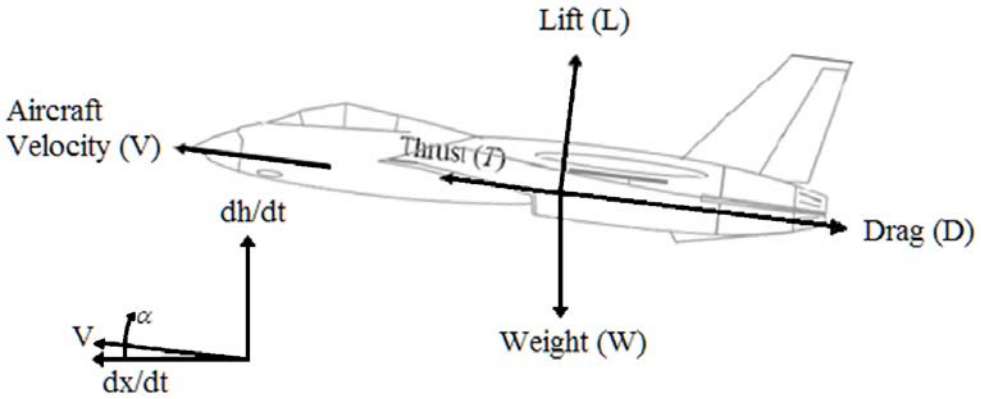

Figure 3.1. Free body diagram used to develop drag-polar model equations.

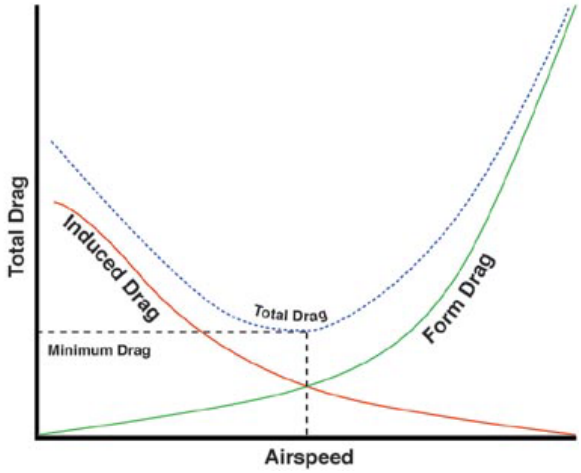

Figure 3.2. Total drag versus airspeed.

Table 3.1. Master flight equation.

Variable	Description	Model Equation
T	Thust (N)	$(T-D)V = W\frac{d}{dt}\left(h+\frac{V^2}{2g}\right)$
D	Drag (N)	
W	Weight (N)	
V	Velocity (m/s)	
h	Altitude (m)	
g	Gravitational acceleration at sea level on Earth (m/s^2)	

Drag-polar model equations are described in Table 3.2. Inputs to the drag-polar model include total vehicle weight, altitude, Mach number and the corresponding properties of air. Using these equations, the drag-polar model calculates the drag force on the vehicle plus a flight angle dependent adjustment to the thrust requirement. This adjustment takes into account the fact that when the vehicle is climbing or descending the thrust requirement will be greater or less, respectively. Notice that at level flight (e.g. α = 0), the thrust requirement equals the drag exactly.

Table 3.2. Drag-polar model equations.

Component	Variable	Description	Model Equation
Aircraft Gross Weight	W_T	Total vehicle weight (N)	$W_T = W_0 + W_f$
	W_f	Weight of fuel (N)	
	W_0	Empty weight of vehicle (N)	
Climb Angle	α	Climb angle (r)	$\Delta x = V\Delta t$ $\alpha = \tan^{-1}\left(\frac{\Delta h}{\Delta x}\right)$
	V	Velocity (m/s)	
	Δt	Time step (s)	
	Δx	Corresponding distance traveled (m)	
	Δh	Change in altitude (m)	
Dynamic Pressure	$P_{dynamic}$	Dynamic pressure (Pa)	$P_{\text{dynamic}} = \frac{1}{2}\rho V^2$
	ρ	Density (kg/m^3)	
	V	Velocity (m/s)	
Coefficient of Lift	C_L	Coefficient of lift	$C_L = \frac{L}{P_{\text{dynamic}}S} = \frac{W_T\cos(\alpha)}{P_{\text{dynamic}}S}$
	L	Lift (N)	
	$P_{dynamic}$	Dynamic pressure (Pa)	
	α	Climb angle (Radians)	
	W_T	Total vehicle weight (N)	
	S	Reference area (m)	
Coefficient of Drag	C_D	Coefficient of drag	$C_D = C_{D0} + KC_L^2$

Component	Variable	Description	Model Equation
	C_{D0}	Coefficient of parasitic drag	
	K	Lift factor	
Thrust Requirement	T_{Req}	Thrust requirement (N)	$T_{\text{Req}} = D + T_{\text{adj}}$ $T_{\text{Req}} = C_D P_{\text{dynamic}} S + W_T \sin(\alpha)$
	T_{adj}	Climb/descent thrust adjustment (N)	
	D	Drag (N)	
	$P_{dynamic}$	Dynamic pressure (Pa)	
	S	Reference area (m)	
	α	Climb angle (r)	
	W_T	Total vehicle weight (N)	

Figure 3.3 shows the implementation of the drag-polar model in Simulink®. As shown in the figure, there are two inputs: the environmental conditions and information from the FTMS regarding the weight of the vehicle. The environmental conditions include information about the current altitude, Mach number, and corresponding air properties. Using this information, the model calculates the current vehicle weight, climb angle, and dynamic pressure. Subsequently, a coefficient of lift is determined. Instead of the model equations described in Table 3.2, the INVENT tip-to-tail model uses a table lookup to convert C_L to C_D. Upon calculating the drag and the climb/descent adjustment, a thrust requirement is calculated. This thrust requirement is sent sent to the engine controller, which varies the flow rate of fuel to the engine.

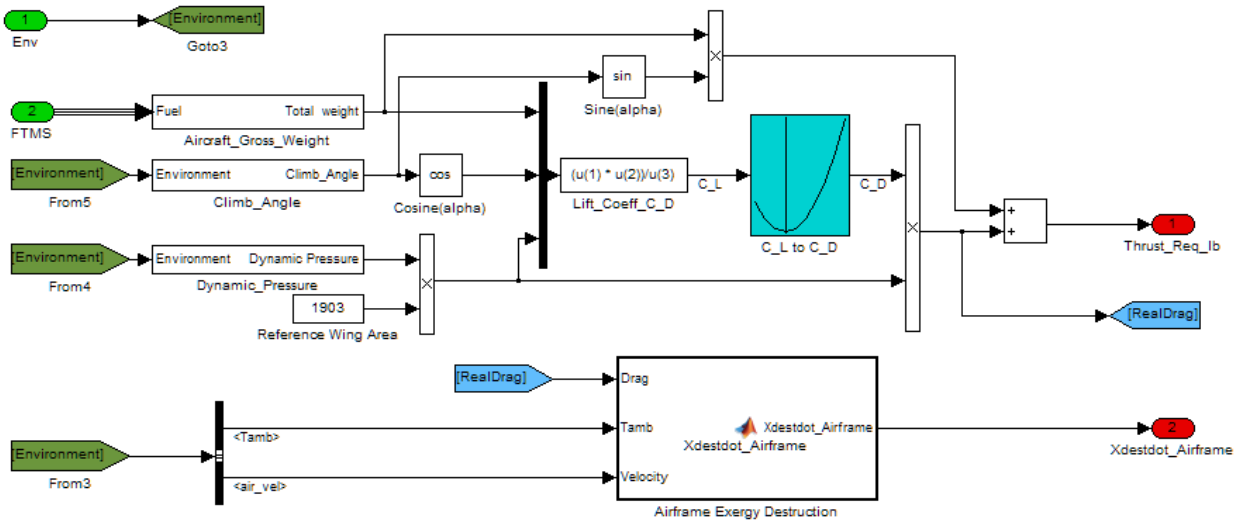

Figure 3.3. Tip-to-tail drag-polar Simulink® model

3.1.1.2 Propulsion Subsystem (PS)

There are many dynamic interfaces between the engine and the other INVENT tip-to-tail subsystems. These interfaces, shown in Figure 3.4, demonstrate how the PS integrates into the tip-to-tail model. It should be noted that these interfaces are for the complete AFRL tip-to-tail model. In the case of the generic INVENT tip-to-tail model used in this thesis work, the REPS and HPEAS loads are simplified to a duty-cycle based lookup table. Additionally, the 6-DOF model displayed in Figure 3.4 is replaced by a drag-polar model in the generic tip-to-tail.

The AVS model calculates the thrust the engine (PS) needs to produce, and the PS returns a fuel flow rate used to update vehicle weight. The REPS calculates a torque load that will be applied to the engine shaft, and the PS model calculates a corresponding shaft speed necessary to produce that torque. The FTMS supplies the fuel flow rate to the PS, and the PS recirculates any fuel used for cooling back to the FTMS. The APTMS extracts bleed air to power the IPP and cool subsystem components and then recirculates some of the bleed air back into the mixer. The HPEAS calculates forces on control surfaces and, in the case of a variable nozzle exit area, sends information regarding the current nozzle position to the PS.

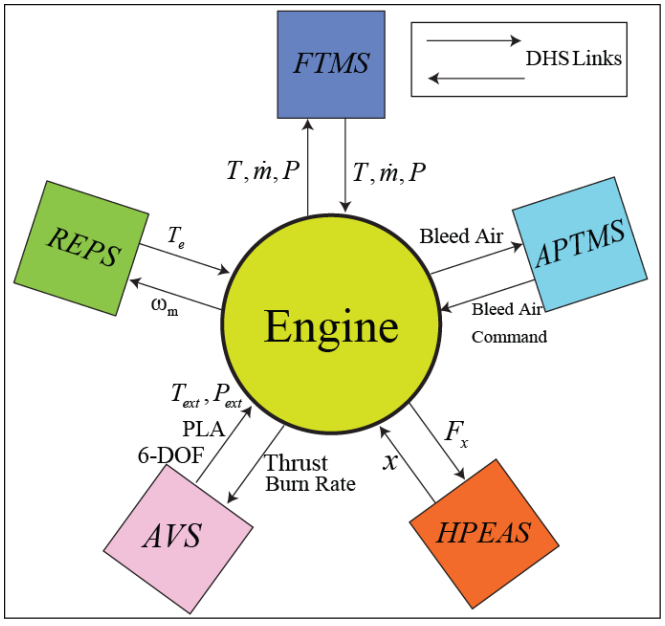

Figure 3.4. Propulsion subsystem integration points.[5,g]

[g] This figure is taken from material that is declared a work of the U.S. Government and is not subject to copyright protection in the United States.

3.1.1.2.1 Brief Description of Tip-to-Tail Engine Model

The PS implemented in the generic INVENT tip-to-tail model is based on the work by Eastbourn.[7] A detailed analysis of the PS model can be found in his work. A brief description of this model and some important characteristics are discussed here. The PS model equations describe a generic, high-bypass ratio turbofan consisting of nine key components:

- Fan
- High pressure compressor (HPC)
- Combustor
- High pressure turbine (HPT)
- Low pressure turbine (LPT)
- Bypass plenum volume
- Nozzle
- High pressure shaft (HPS)
- Low pressure shaft (LPS)

A schematic of a typical turbofan engine, as well as one of the generic INVENT tip-to-tail engine model can be found in Figure 3.6 and Figure 3.5, respectively. Figure 3.6 shows the schematic of the generic INVENT tip-to-tail PS system. Note that order of the components in the figure corresponds to the physical layout of a typical turbofan engine. Figure 3.5 shows a schematic of a typical turbofan engine. The schematic shows that a portion of the air that enters the fan is sent to the core where it is compressed, combusted, and expanded, and a portion of the flow is bypassed around the core. This behavior is typical of a high-bypass turbofan engine which, in this case, pulls bleed streams from both the fan and compressor for use in the thermal management subsystems.

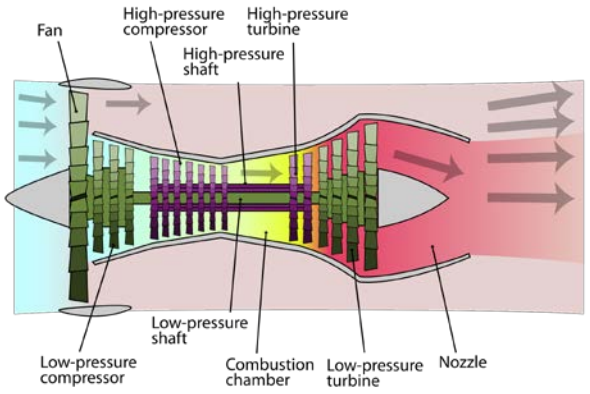

Figure 3.5. Generic turbofan engine.

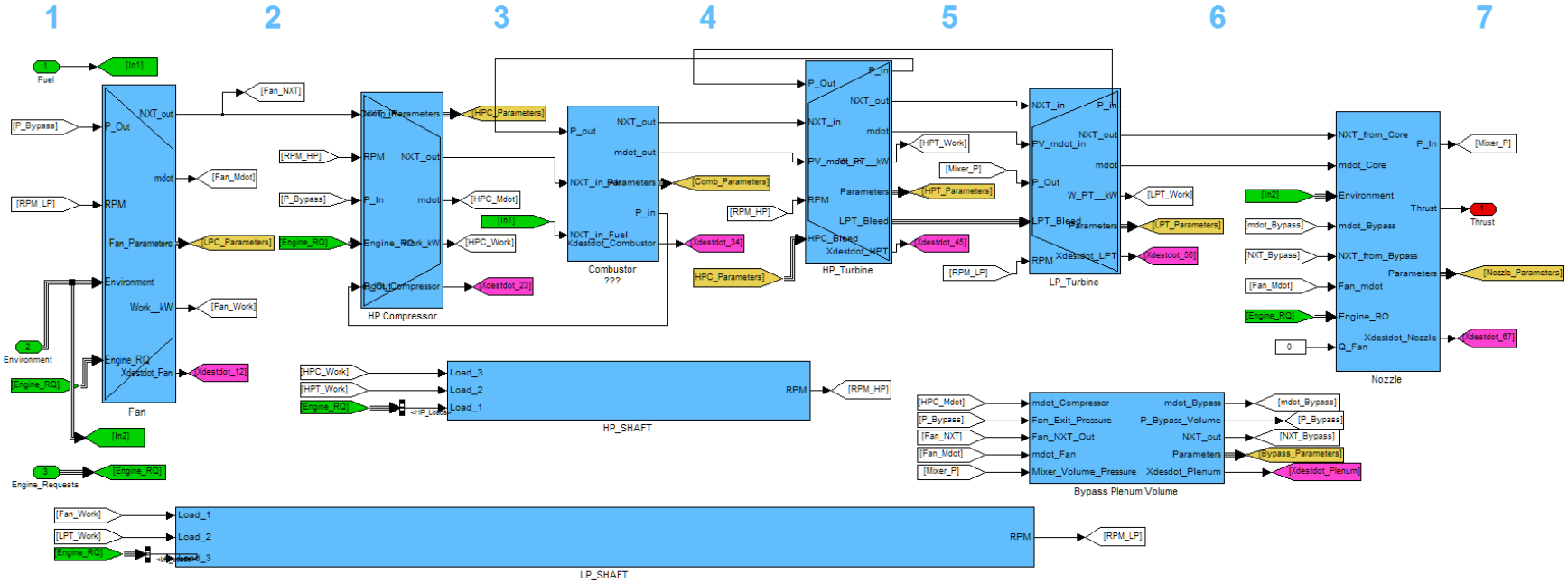

Figure 3.6. Tip-to-tail engine model.

3.1.1.2.2 Important PS Model Characteristics

The turbofan engine implemented in the generic INVENT tip-to-tail is rated at 20,000 lb_f. This tip-to-tail model is intended to describe a generic long range strike (LRS) vehicle. The LRS model should describe a flying wing, four engine aircraft similar in configuration to a B-2 Spirit. As such, the maximum available thrust of the PS is 80,000 lb_f.

The PS model implemented in the tip-to-tail is unique in that it captures the dynamic behavior of the engine using plenum volumes. The bypass plenum volume uses dynamic equations to model a duct connecting the volume between the fan and the HPC to the mixer. This bypass volume ensures that not all the air coming into the fan enters the engine core. This is beneficial for several reasons. Firstly, air can be extracted from the bypass plenum volume and used to power the integrated power pack (IPP) and cool components in the thermal management subsystems (FTMS/APTMS). Secondly, the bypass air eventually mixes with the core stream, reducing the average velocity of the air exiting the nozzle. Since exit velocity is directly proportional to noise, high-bypass turbofans typically are quieter than low-bypass engines. Thus, stealth aircraft like the LRS benefit from high-bypass turbofans.

3.1.2 Electrical Subsystems

There are two primary electrical subsystems in the generic INVENT tip-to-tail model: the HPEAS and the REPS. However, the thermal tip-to-tail model does not include high-fidelity electrical subsystem models. In this thesis work, all loads and responses within the HPEAS and REPS are defined by lookup tables.

3.1.2.1 High Power Electric Actuation Subsystem (HPEAS)

A block diagram of the tip-to-tail HPEAS implemented in Matlab® Simulink® is shown in Figure 3.7 below. Inputs to the HPEAS are contained in the ‘Mission’ bus. The ‘Mission’ bus is an output from the AVS that defines a duty cycle for the HPEAS. Based on this duty cycle, the HPEAS uses a table lookup to determine various heat loads, electrical loads, and the temperature of the hydraulics within the electromechanical actuators.

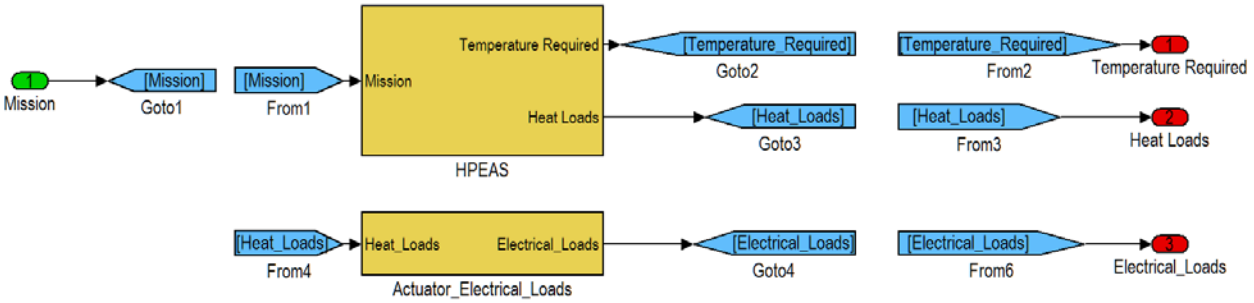

Figure 3.7. HPEAS implemented in Matlab® Simulink® tip-to-tail model.

3.1.2.2 Robust Electrical Power Subsystem (REPS)

The REPS, although more detailed than the HPEAS, still uses a pre-defined duty cycle to determine a heat/electrical load schedule. Inputs to the REPS are the same 'Mission' bus used in the HPEAS, current altitude and Mach number, electrical loads from the HPEAS, and an electrical load from the DEWS. Using these inputs, the REPS utilizes table lookups to determine heat loads from various components in the tip-to-tail including the Full Authority Digital Engine Control (FADEC), cockpit and avionics. Additionally, the generator block calculates a required power that gets sent to the system controller, which will vary the performance of the IPP in order to meet the request.

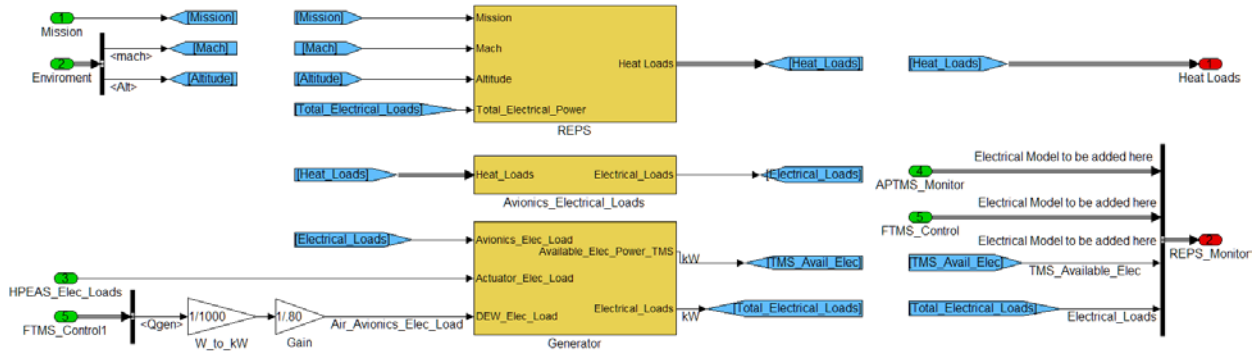

Figure 3.8. REPS implemented in Simulink® tip-to-tail model.

3.1.3 Thermal Management Subsystems

Within the generic INVENT tip-to-tail, there are two primary thermal management subsystems: the FTMS and the APTMS. Many subsystems in the tip-to-tail generate heat loads, including the HPEAS, REPS, DEWS, onboard avionics, pumps, and compressors. The FTMS

and APTMS contain heat exchangers that use fuel, RAM or bleed air, and secondary (closed-loop) water or PAO to manage these loads. The system controller block contains PI controllers responsible for managing the flow rates in order to effectively handle the heat loads.

3.1.3.1 Fuel Thermal Management Subsystem (FTMS)

The FTMS, shown schematically in Figure 3.9, is a complex subsystem with several key responsibilities:

1. The FTMS manages thermal loads from the DEWS. The temperature of the laser diode arrays within the DEWS strongly affects the performance of the DEWS. In order to keep emitted radiation within the absorption band of the gain media, the diode array temperature must be kept within a few degrees of the design operating temperature.[47] Thus, FTMS performance is critical in maintaining DEWS efficiency.
2. The FTMS is responsible for keeping the temperature of the fuel below the vaporization temperature. Fuel is an excellent heat sink and is used extensively throughout the FTMS to cool various components including the hydraulics heat exchanger and the DEW. Fuel also interacts, via a heat exchanger, with a secondary PAO loop that cools the power and thermal management system controller / inverter converter controller unit (PTMSC/ICC).
3. The FTMS contains the tip-to-tail's fuel tanks and pumps. The FTMS interacts with the system controller to manage the amount of fuel being sent to the PS. However, the fuel gets sent to the PS only after it has absorbed heat from several of the aforementioned components. To ensure that the fuel does not get too hot, the FTMS interacts with the system controller to increase closed loop flow rates and reduce flow temperatures.
4. The FTMS sends fuel to a vapor compression subsystem (VCS) found in the APTMS. The VCS uses a bleed stream from the fan to cool the fuel before it gets recirculated back into the fuel tanks.

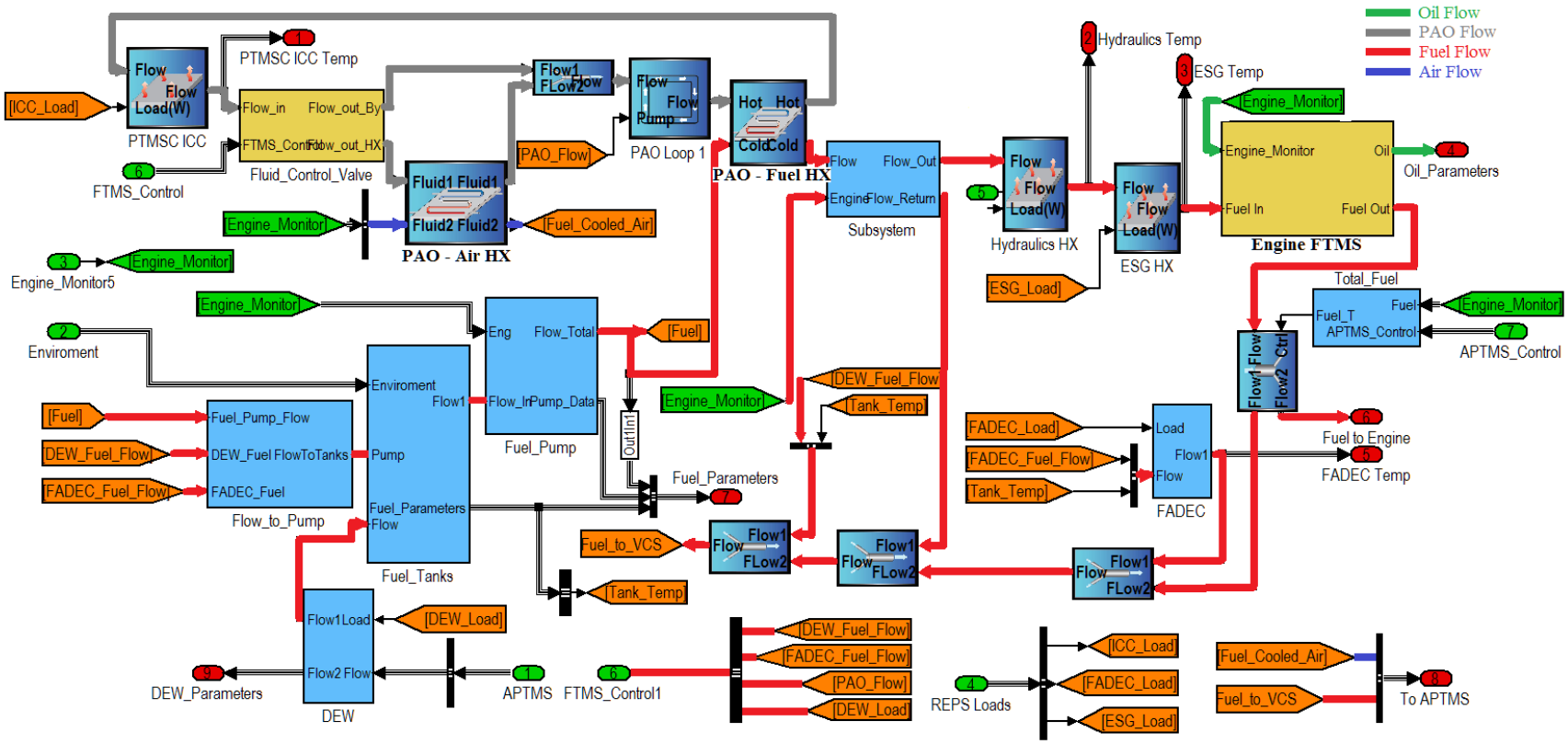

Figure 3.9. FTMS implemented in Simulink® tip-to-tail model.

3.1.3.2 Advanced Power & Thermal Management Subsystem (APTMS)

The APTMS, shown schematically in Figure 3.10, is the thermal management subsystem responsible for managing and powering several important subsystem components:

1. The APTMS contains the IPP, a source of auxiliary power used to run the generator found in the REPS. The IPP is essentially a turbo-shaft engine that combusts fuel from the FTMS with bleed air from the PS to create power.
2. The tip-to-tail avionics package is cooled by both liquid and air streams. A closed PAO loop cools the liquid cooled avionics. The PAO temperature is maintained to a reasonable temperature through interaction with the fan bleed air via a compact heat exchanger. This heat exchanger, labeled 'Multinode_Transient_HX1' in Figure 3.10, was modeled and implemented as part of this thesis work. Additional heat exchangers within the APTMS, including 'Multinode_Transient_HX' have also been developed as part of this thesis work. The optimization described in Chapter 4 uses the synthesis/design variables of these heat exchangers as optimization decision variables.
3. Bleed air extracted from the PS is split into two streams which are used to manage the thermal loads of the air cooled avionics and the cockpit. These two streams are rejected to the environment.

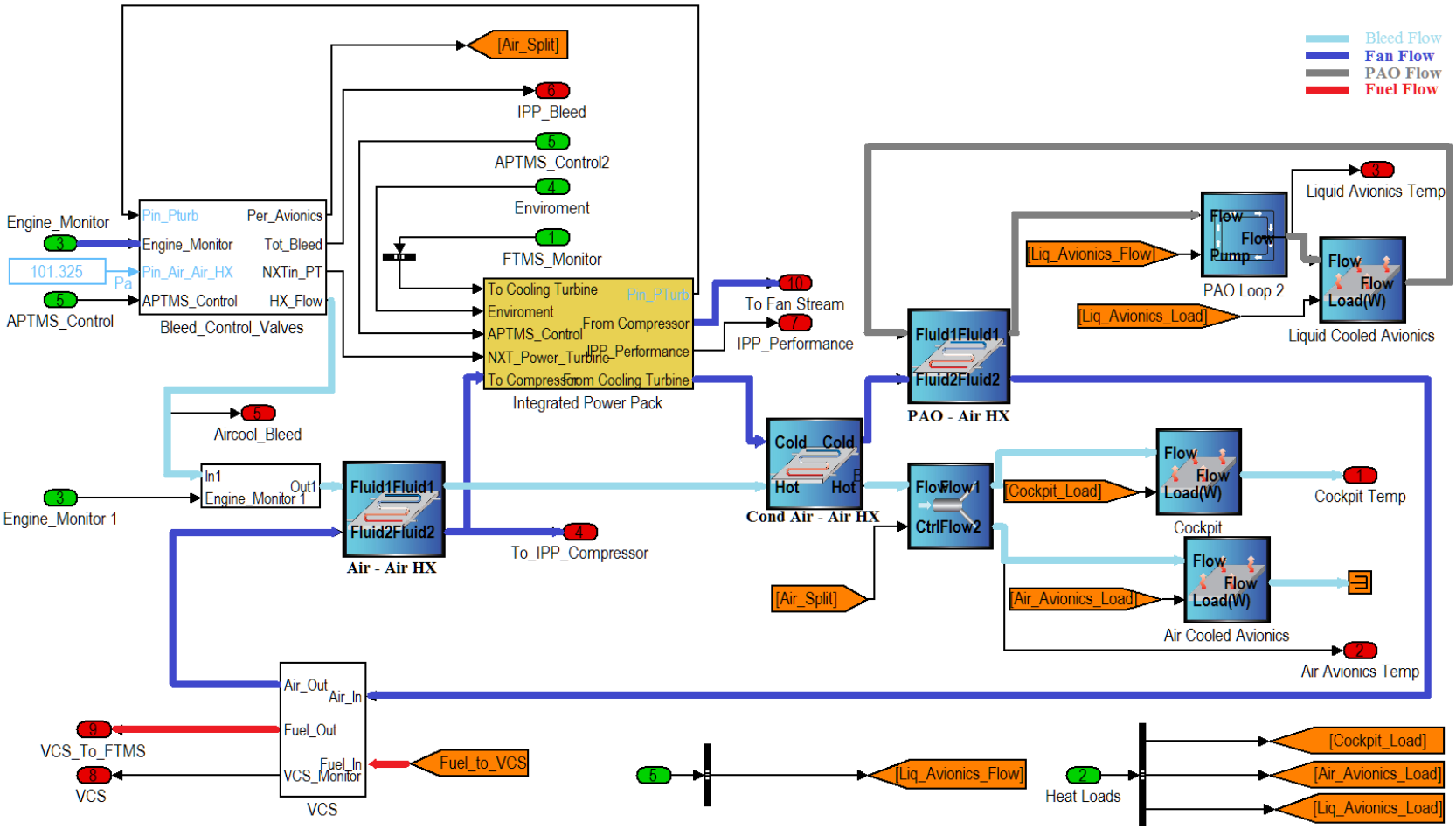

Figure 3.10. APTMS implemented in Simulink® tip-to-tail model.

3.2 Heat Exchanger Model

This thesis work includes the development of a transient, multi-nodal, heat exchanger to be used as a replacement for several of the heat exchanger models previously implemented in the generic INVENT tip-to-tail. These previously implemented heat exchangers needed to be revised for reasons that will be discussed further on in this chapter. Additional work includes the development of an iterative method for determining heat exchanger mass and volume based on physical and operational parameters.

3.2.1 Development of the Heat Exchanger Sizing Algorithm

The equations and parameters describing the physical geometry of a compact heat exchanger can be found in Table 3.3. The parameters describing the physical geometry, shown schematically in Figure 3.11, are related to five important characteristics of a compact heat exchanger: hydraulic diameter, D_h, porosity, σ, and non-dimensional aspect ratios α, δ and γ.

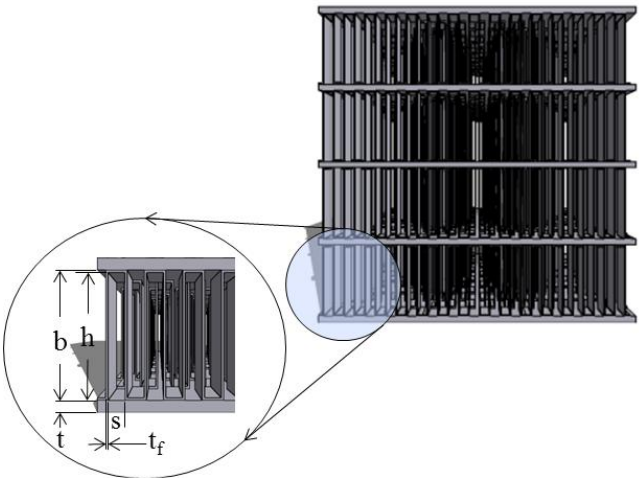

Figure 3.11. Schematic of a typical counter-flow compact heat exchanger.

The hydraulic diameter is related to the Reynolds number, which impacts not only the heat transfer capabilities of the heat exchanger but the pressure drop across it. The porosity is a measure of heat exchanger compactness and can be defined as the ratio of enclosed (wetted) volume to total volume. Another measure of compactness is the heat transfer surface area

density, β, the ratio of wetted surface area to total volume. Typically, for an OSF compact heat exchanger, β ranges from 300 to 3000 m^2/m^3. The non-dimensional aspect ratios defined in Table 3.3 are used in the correlations to determine f, the Fanning friction factor, and j, the Colburn coefficient, both of which are defined in Table 3.5.

Table 3.3. Equations describing the physical geometry of the new heat exchanger model.

Variable	Description	Model Equation
D_h	Hydraulic diameter (m)	$D_h = \frac{4shl}{2(sl + hl + t_f h) + t_f s}$
σ	Porosity (m^3/m^3)	$\sigma = \frac{s(b - t_f)}{(s + t_f)(b + t)}$
β	Surface area density of one side of heat exchanger (m^2/m^3)	$\beta = \frac{4\sigma}{D_h}$
s	Fin channel width (m)	
h	Fin channel height (m)	
l	Fin strip length (m)	
b	Plate gap thickness (m)	
t_f	Fin thickness (m)	
t	Plate thickness (m)	
L	Overall heat exchanger length (m)	$\alpha = \frac{s}{h},\ \delta = \frac{t_f}{l},\ \gamma = \frac{t_f}{s}$
α	Non-dimensional aspect ratio	
δ	Non-dimensional aspect ratio	
γ	Non-dimensional aspect ratio	

3.2.1.1 Iterative Process to Solve for Area

An important aspect of the algorithm created to determine heat exchanger size is the iterative process shown in Figure 3.12. Solving for area requires an iterative approach due to the implicit nature of the equations found in Table 3.5. Calculating the Reynolds number requires knowledge of u, the fluid flow velocity, which is a function of the volumetric flow rate and flow area. Of these two, volumetric flow rate is known, leaving flow area as the only unknown. If the flow area, $A_{c,0}$, is provided as an initial estimate, working through the equations yields the mass velocity term, G, which is a function of the mass flow rate and flow area. At this point, it is

possible to solve for the new flow area. However, unless the initial estimate for the flow area is correct, the calculated flow area is different from this initial value. Thus, it is necessary to undergo the iterative process described in Figure 3.12 and below until convergence is reached. Fast convergence is guaranteed with a sufficiently close initial guess. However, providing the algorithm with an accurate initial guess requires some heuristic knowledge. The iterative process is as follows:

1. Selection of the physical parameters of the heat exchanger allows for the calculation of the hydraulic diameter.
2. Providing an estimate for the heat exchanger flow area allows the Reynolds number to be determined.
3. Using the Reynolds number and the non-dimensional aspect ratios described in Table 3.3, the Colburn coefficient, *j*, and friction factor, *f*, can be determined. The correlations for *f* and *j* are unique in that, as demonstrated by the authors, the correlations are valid for both laminar and turbulent flow regimes.[48] Notice that these equations account for the geometry of the heat exchanger through the non-dimensional aspect ratios defined in Table 3.3.
4. The effectiveness-Ntu method, shown in Figure 3.12, is used in the determination of the heat exchanger effectiveness.
5. The pressure drop and subsequently the mass velocity are calculated based on the previously determined information.
6. From the mass velocity, a new flow area is calculated. If the new flow area differs from the previously guessed/calculated flow area, an iterative process ensues until the difference between the current flow area and previous value are within some tolerance.
7. Using the flow area, it is possible to determine the weight, volume, and surface area of the heat exchanger using the equations shown in Table 3.6.

The implementation of this method requires several assumptions. The first assumption is that the fin efficiency is constant at 0.8[37]. Previous optimizations have shown this assumption is valid for most heat transfer coefficients and fin materials. Additional assumptions include incompressible flow and constant properties (e.g., specific heat, density, viscosity), which are

also valid for this application due to the relatively low temperature and pressure ranges that the system operates within.

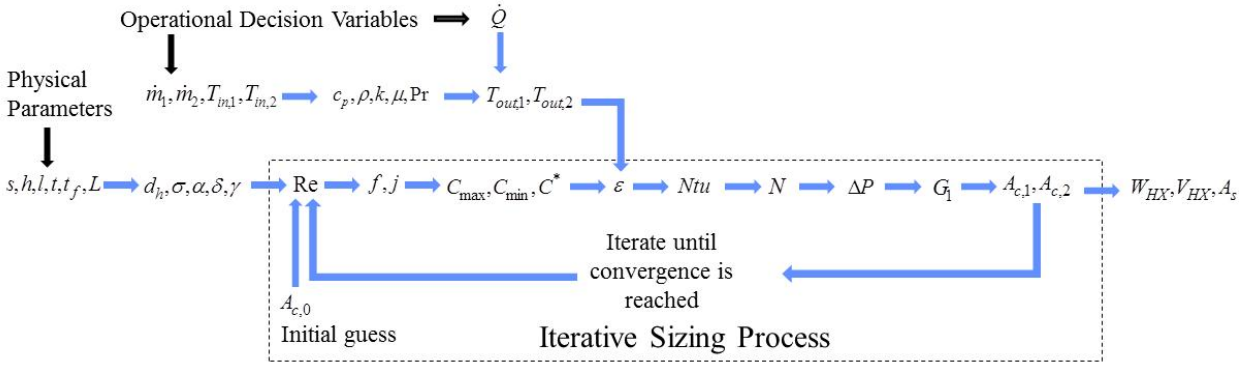

Figure 3.12. Iterative process used to size heat exchanger for each application.

Table 3.4. Equations used to determine heat exchanger effectiveness.

Variable	Description	Model Equation
ε	Effectiveness	$C_{\min} = \min(C_{hot,in}, C_{cold,in})$
Q_{max}	Maximum heat transfer (W)	$C_{\max} = \max(C_{hot,in}, C_{cold,in})$
C_{min}	Minimum heat capacity (J/K)	$\dot{Q}_{\max} = C_{\min}(T_{hot,in} - T_{cold,in})$
C^*	Heat capacity ratio	$\dot{Q}_{heat} = \varepsilon \cdot \dot{Q}_{\max}$
C_{max}	Maximum heat capacity (J/K)	$C^* = C_{\min} / C_{\max}$
Ntu	Number of thermal units	$\varepsilon = \frac{1 - e^{-NTU(1-C^*)}}{1 - C^* e^{-NTU(1-C^*)}}$
		$Ntu = \frac{\varepsilon}{1 - \varepsilon}$

Table 3.5. Equations describing iterative process used to size heat exchanger.[37,48]
Manglik, R. M., Bergles, A. E., *Heat Transfer and Pressure Drop Correlations for the Rectangular Offset Strip Fin Compact Heat Exchanger*, Experimental Thermal and Fluid Science, Volume 10, Number 2, pp. 171-180, Feb. 1995. Used with the permission of Elsevier, 2012.

Variable	Description	Model Equation
f	Fanning friction factor	$\mathrm{Re} = \frac{\rho u D_h}{\nu}$
j	Colburn coefficient	$f = 9.6243\,\mathrm{Re}^{-0.7422}\,\alpha^{-.01856}\delta^{0.3053}\gamma^{-0.2659} \times \left(1 + 7.669\times10^{-8}\,\mathrm{Re}^{4.429}\,\alpha^{0.92}\delta^{3.767}\gamma^{0.236}\right)^{0.1}$
ε	Heat exchanger effectiveness	$j = 0.6522\,\mathrm{Re}^{-0.5403}\,\alpha^{-0.1541}\delta^{-0.1409}\gamma^{-0.0678} \times \left(1 + 5.269\times10^{-5}\,\mathrm{Re}^{1.34}\,\alpha^{0.504}\delta^{0.46}\gamma^{-1.055}\right)^{0.1}$
$\dot{Q}$	Heat load (W)	$\varepsilon = \frac{Q}{Q_{\max}} = \frac{\dot{Q}}{\left(\dot{m}\times c_p\right)_{\min}\left(T_{1,i} - T_{2,i}\right)}$
$\dot{Q}_{\max}$	Design heat load (W)	$Ntu = \frac{\varepsilon}{1-\varepsilon}$
Ntu	Number of thermal units	$N = \frac{2\times Ntu}{\eta_0}$
N	Ntu for one side	$\Delta p = \frac{1}{2}\rho f\left(\frac{\dot{m}}{A_c}\right)^2\frac{4L}{D_h}$
$A_{c,fluid}$	Fluid flow area (m^2)	$G_1 = \frac{\dot{m}_1}{A_{c,1}} = \sqrt{\frac{2\times\rho_1\times\Delta p_1\times j_1/f_1}{\mathrm{Pr}_1^{2/3}\,N}}$
ΔP	Pressure drop (Pa)	
G	Mass velocity (kg/m^2s)	

Table 3.6. Equations used to determine heat exchanger volume and weight.

Variable	Description	Model Equation
m_{hx}	Mass of heat exchanger (kg)	$m_{hx} = \rho_m L\left(\frac{A_{c,1}}{\sigma_{1`}}\left(1-\sigma_1\right) + \frac{A_{c,2}}{\sigma_2}\left(1-\sigma_2\right)\right) + \left(A_{c,1}\rho_1 + A_{c,2}\rho_2\right)L$
m_s	Mass of one side of heat exchanger (kg)	

Variable	Description	Model Equation
V_{hx}	Volume of heat exchanger (m^3)	$V_{hx} = L\left(\frac{A_{c,1}}{\sigma_1}(1-\sigma_1)+\frac{A_{c,2}}{\sigma_2}(1-\sigma_2)\right)$
A_s	Surface area of one side of heat exchanger (m^2)	$A_s = \beta\left(L\left(\frac{A_c}{\sigma}(1-\sigma)\right)+A_c\right)$

3.2.2 Discussion of the Original Heat Exchanger Models

The heat exchanger model constructed as part of this thesis work was an improvement over the original heat exchanger model implemented in the generic INVENT tip-to-tail model provided by the AFRL. The latter, while correctly implemented, was insufficient for the purposes of optimization for several reasons: the correlations used to determine the heat transfer coefficients were not applicable to the physical system, and there were no correlations linking the physical parameters of the compact heat exchanger (e.g., mass, volume, etc.) to its performance. By leaving these issues unresolved, successful optimization of the tip-to-tail would have been rendered impossible due to the fact that heat exchangers add significant mass to the model and play a critical role in the overall thermodynamic performance of the system. A distinguishing feature of the heat exchanger model developed as part of this thesis work is the inclusion of synthesis/design variables that dictate the performance and size of the heat exchanger. Equations describing the behavior of the original heat exchanger model can be found in Table 3.7.

The equations in this table are implemented in Matlab® Simulink® and solved using the ordinary differential equation (ode23s) solver. The most obvious problem with the equations shown in Table 3.7 is that while the heat transfer coefficient, *h*, is a function hydraulic diameter, D_h, there is no correlation between the hydraulic diameter and the fin geometry. As demonstrated in Table 3.3 and Figure 3.12, the parameters used to define D_h are also used to define α, γ and λ, which do have a significant impact on heat exchanger performance. Additionally, in solving for the heat transfer coefficient, the Dittus-Boelter[49] correlation is used.

The Dittus-Boelter correlation is commonly used when modeling heat exchangers. However, it is only reasonable to use the Dittus-Boelter correlation under the following conditions:[49]

- $0.7 \leq Pr \leq 160$
- $Re \geq 10^4$
- $L/D_h \approx 10$

In many cases, especially when using viscous oils, the Reynolds' number can be much less than 10^4, the Prandtl number can be larger than 160, and subsequently, the Dittus-Boelter equation does not apply.

Table 3.7. Model equations representing original heat exchanger model.[h]

Variable	Description	Model Equation
Re	Reynolds Number	$\mathrm{Re} = \frac{\rho u D_h}{\nu}$
ρ	Fluid density (kg/m^3)	
D_h	Hydraulic diameter (m)	
u	Fluid velocity (m/s)	$Nu = 0.023\,\mathrm{Re}^{4/5}\,\mathrm{Pr}^{n}$
ν	Dynamic Viscosity (m^2/s)	$h = \frac{NuD_h}{k}$
Pr	Prandtl number	$Q_{net} = h_1 A_1 \left(T_{1,o} - T_{hx}\right) + h_2 A_2 \left(T_{2,o} - T_{hx}\right)$
Nu	Nussult number	
k	Thermal conductivity ($W/m\text{-}K$)	$T_{2,o_{n+1}} = \int \frac{-h_2 A_2 \left(T_{2,o_n} - T_{hx}\right) + \dot{m}_2 c_{p,2} \left(T_{2,i_n} - T_{2,o_n}\right)}{V_{hx}\left(\frac{m_{hx}}{V_{hx}}\right) c_{p,2}} dT_{2,o_n} + T_{2,o_n}$
$\dot{m}_{fluid}$	Fluid flow rate (kg/s)	
$c_{p,fluid}$	Specific heat capacity of fluid ($J/kg\text{-}K$)	
h_{fluid}	Film coefficient ($W/m^2\text{-}K$)	$T_{1,o_{n+1}} = \int \frac{-h_1 A_1 \left(T_{1,o_n} - T_{hx}\right) + \dot{m}_1 c_{p,1} \left(T_{1,i_n} - T_{1,o_n}\right)}{V_{hx}\left(\frac{m_{hx}}{V_{hx}}\right) c_{p,1}} dT_{1,o_n} + T_{1,o_n}$
Q_{net}	Heat load (W)	
A_{Fluid}	Heat transfer area (m^2)	
T_{Fluid}	Fluid temperature (K)	
T_{HX}	Mass temperature (K)	

[h] As a matter of convention, the hot fluid is denoted as fluid one, and the cold as fluid two.

In light of the aforementioned issues, it was necessary to devise a new heat exchanger model that accounts for the effect physical parameters have on heat exchanger performance and utilizes correct heat transfer correlations. The most appropriate model in this case is of a compact plate-fin heat exchanger, a schematic of which is seen in Figure 3.11. The process used to construct this heat exchanger model can be broken into two steps:

1. Size the heat exchanger:
    a. Create an algorithm that calculates the weight and volume of the compact heat exchanger based on the physical and operational parameters.
    b. Minimize the weight of the heat exchanger by performing synthesis/design optimization using the appropriate physical parameters and operational constraints.
2. Construct the heat exchanger model:
    a. Formulate the equations governing the thermodynamic performance of the heat exchanger and ensure that the new model uses the correct correlations to determine the heat transfer coefficients.
    b. Validate the model by comparing the results obtained from simulations to data found in the literature.

3.2.3 Development of Transient Heat Exchanger Model Equations

A counter-flow, plate-fin heat exchanger model is created from a collection of thermodynamic, geometric, and heat transfer models. In addition, this model is implemented as a one-dimensional model, discretized along the axial flow direction using a finite difference approximation. The resulting thermodynamic system, shown in Figure 3.13, utilizes two working fluids and an intermediary heat exchanger mass. The model describes an open-system with two mass interactions. Individual thermodynamic energy and mass conservation balances for the two working fluids and heat exchanger account for heat transfer. These thermodynamic models are presented in Table 3.8 and assume incompressible behavior and one-dimensional flow.

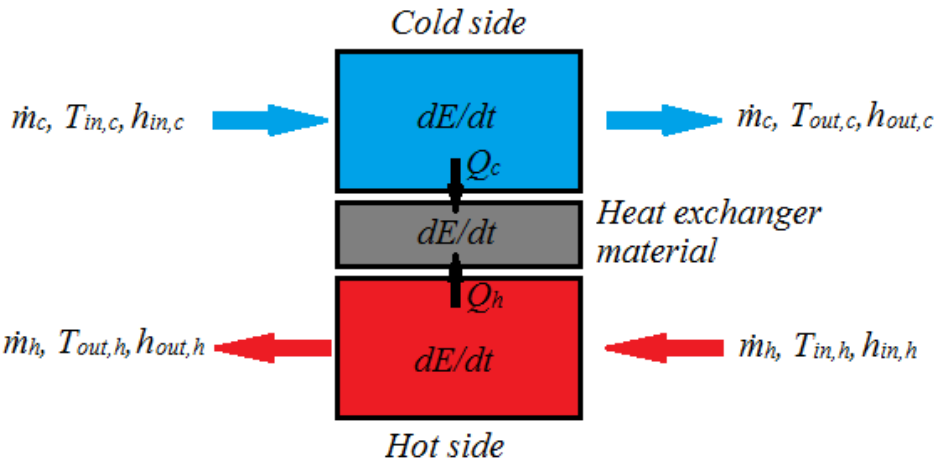

Figure 3.13. Heat exchanger thermodynamic system used to formulate energy balance equations.

Table 3.8. Heat exchanger thermodynamic model equations.

Variable	Description	Model equation
m_{HX}	Heat exchanger mass (*kg*)	$m_{HX} c_{HX} \frac{dT_{HX}}{dt} = \dot{Q}_h + \dot{Q}_c$ $m_h c_{p,h} \frac{dT_h}{dt} = -\dot{Q}_h + \dot{H}_{h,in} - \dot{H}_{h,out}$ $m_c c_{p,c} \frac{dT_c}{dt} = -\dot{Q}_c + \dot{H}_{c,in} - \dot{H}_{c,out}$
c_{HX}	Heat exchanger specific heat capacity (*J/kg-K*)	
T_{HX}	Heat exchanger temperature (*K*)	
$\dot{Q}_h$	Hot fluid heat interaction (*W*)	
$\dot{Q}_c$	Cold fluid heat interaction (*W*)	
m_{fluid}	Fluid mass (*kg*)	
$c_{p,fluid}$	Fluid specific heat capacity (*J/kg-K*)	
T_{fluid}	Fluid temperature (*K*)	
$\dot{H}_{fluid,in}$	Enthalpy flow rate into the system (*W*)	
$\dot{H}_{fluid,out}$	Enthalpy flow rate out of the system (*W*)	

3.2.4 Heat Transfer Model

Table 3.9 describes the metrics used to measure heat exchanger performance. The primary measure of heat exchanger performance is effectiveness, which is theoretically bounded between zero and unity. As heat exchanger performance and size increases, the effectiveness approaches unity. However, second law limitations prevent heat exchanger effectiveness from actually reaching unity. Table 3.9 also describes the methodology used to determine the heat transfer

coefficients utilized in the thermodynamic model. Based on the Reynolds number and Prandtl number, an appropriate correlation for Nussult number is determined from Table 3.10. Upon determination of the Nussult number, it is simple to calculate the wall heat transfer coefficient for each side of the heat exchanger. Matlab® Simulink's® numerical solver has difficulty converging to a solution if it is continually switching which correlation the model is using to calculate *Nu*. For example, if the Prandtl number drops below 1.5 during the simulation (due to changes in fluid temperature), the correlation used to calculate *Nu* changes. This causes a discontinuity that causes to solver to fail to converge within that iteration. In the heat exchanger model, the Gnielinski correlations shown in the table are replaced by a surrogate to ensure that Nu is a continuous function of *f*, Re, Pr, and D_h.

Table 3.9. Heat transfer model equations.

Component	Variable	Description	Model Equation
Methodology for Determining Wall Heat Transfer Coefficients	h	Fluid, film coefficient (W/m^2K)	$Nu = g(f, \mathrm{Re}, \mathrm{Pr}, D_h)$ (Use Gneilinski Correlations, Table 3.10) $h = Nu \cdot k_f / D_h$
	Nu	Nussult number	
	k_f	Fluid thermal conductivity ($W/m\text{-}K$)	
	D_h	Hydraulic diameter (D_h)	
	f	Friction factor	
	Re	Reynolds number	
	Pr	Prandtl number	

Table 3.10. Gnielinski correlations used in solving for the Nussult number.[50]
Gnielinski, V., 1983, *Forced Convection in Ducts, Section 2.5.1*, Heat Exchanger Design Handbook, Hemisphere. Used under fair use, 2012.

Model Equation	Valid Range	
	Reynold's Number	Prandtl Number
$Nu = \frac{(f/2)(\mathrm{Re}-1000)\mathrm{Pr}}{1+12.7(f/2)(\mathrm{Pr}^{2/3}-1)}\left[1+\left(\frac{d_h}{L}\right)^{2/3}\right]$	Re = [2300, $5x10^4$]	Pr = [0.2, 2000]

Model Equation	Valid Range	
	Reynold's Number	Prandtl Number
$Nu = 0.0214\left(\mathrm{Re}^{0.8} - 100\right)\mathrm{Pr}^{0.4}\left[1+\left(\frac{d_h}{L}\right)^{2/3}\right]$	Re = [10^4, 5x10^5]	Pr = [0.5, 1.5]
$Nu = 0.012\left(\mathrm{Re}^{0.87} - 280\right)\mathrm{Pr}^{0.4}\left[1+\left(\frac{d_h}{L}\right)^{2/3}\right]$	Re = [3x10^3, 10^6]	Pr = [1.5, 500]

3.2.5 Transient Exergy Balance Equations

As mentioned previously, the model uses a 1D finite difference approximation to increase the fidelity of the heat exchanger model. This ensures a more accurate calculation of the heat exchanger exergy destruction. Transient exergy balances are implemented in the model. However, because temperature is defined as

$$T = \left(\frac{dE}{dS}\right)_{V,n,\beta} \tag{3.3}$$

it must be true that temperature can only be defined in an equilibrium state (i.e., along the line of equilibrium states defined by the energy-entropy curve). Thus, for a system in a non-equilibrium (i.e., transient) state, temperature cannot be defined. However, in order to capture the transient behavior of the system, an approximation to the temperature of the non-equilibrium state can be made based on the average of the inlet and outlet bulk flow states of each control volume (CV). Figure 3.14 shows a diagram of the system used to formulate the exergy balance equations shown in Table 3.11

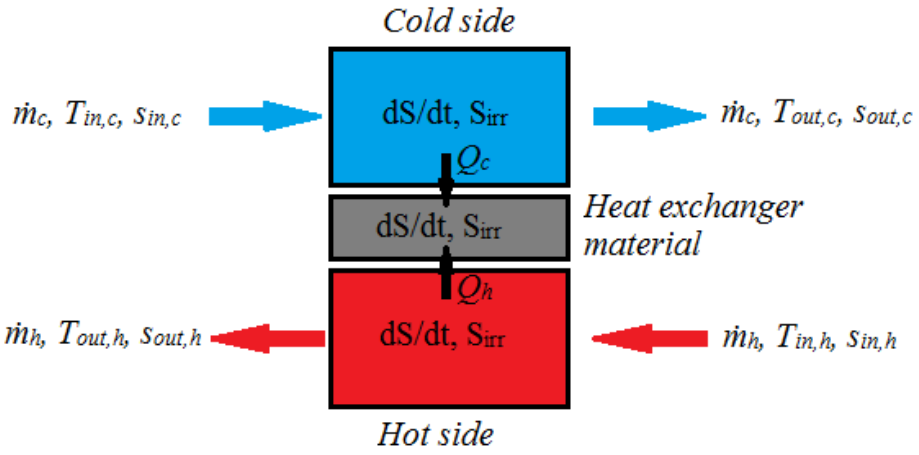

Figure 3.14. Heat exchanger thermodynamic system used to formulate the entropy balance equations.

Table 3.11. Heat exchanger exergy balance equations.

Variable	Description	**Model equation**
$\dot{S}_{irr,c}$	Cold fluid entropy generation rate (*W/K*)	$m_c \frac{c_{p,c}}{T_c}\frac{dT}{dt} = \frac{-\dot{Q}_c}{T_{HX}} + \dot{m}\left(s_{in,c} - s_{out,c}\right) + \dot{S}_{irr,c}$
$\dot{S}_{irr,h}$	Hot fluid entropy generation rate (*W/K*)	$m_h \frac{c_{h,c}}{T_h}\frac{dT}{dt} = \frac{-\dot{Q}_h}{T_{HX}} + \dot{m}\left(s_{in,h} - s_{out,h}\right) + \dot{S}_{irr,h}$
$\dot{S}_{irr,HX}$	HX entropy generation rate (*W/K*)	$m_{HX} \frac{c_{h,HX}}{T_{HX}}\frac{dT}{dt} = \frac{\dot{Q}_c + \dot{Q}_h}{T_{HX}} + \dot{S}_{irr,HX}$
s	Fluid/material specific entropy (*J/kg-K*)	$\dot{X}_{dest} = -T_0\left(\dot{S}_{irr,HX} + \dot{S}_{irr,hot} + \dot{S}_{irr,cold}\right)$
c_p	Fluid/material specific heat (*J/kg-K*)	$\dot{X}_{dest} = -T_0[m_{HX}\frac{c_{h,HX}}{T_{HX}}\frac{dT}{dt} + m_h\frac{c_{h,c}}{T_h}\frac{dT}{dt} - \dot{m}\left(s_{in,h} - s_{out,h}\right) + m_c\frac{c_{p,c}}{T_c}\frac{dT}{dt} - \dot{m}\left(s_{in,c} - s_{out,c}\right)]$
$\dot{Q}_c$	Heat transfer rate into the cold fluid (W)	
$\dot{Q}_h$	Heat transfer rate out of the hot fluid (W)	
T_c	Temperature of the cold-side CV (*K*)	
T_h	Temperature of the hot-side CV(*K*)	
T_{HX}	Temperature of the heat exchanger mass (*K*)	
$\dot{X}_{dest}$	Composite system exergy destruction rate (*W*)	

3.2.6 Heat Exchanger Model Behavior

In order to ensure that the model behavior is correct, temperature distributions across the heat exchanger for the hot and cold fluid streams are compared to results presented in Shah.[39] Three cases are considered. In case (a), the heat capacity ($C = \dot{m}c_p$) of the hot fluid is larger than that of the cold fluid. In case (b), the heat capacities of each fluid are equivalent, while in case (c), the cold fluid has a larger heat capacity than the hot fluid. Figure 3.15 shows published results[39] for each of the three cases. Figure 3.16 shows results obtained from simulations of the heat exchanger model under each of the three conditions. A comparison of these results makes it clear that the heat exchanger model behaves as it should.

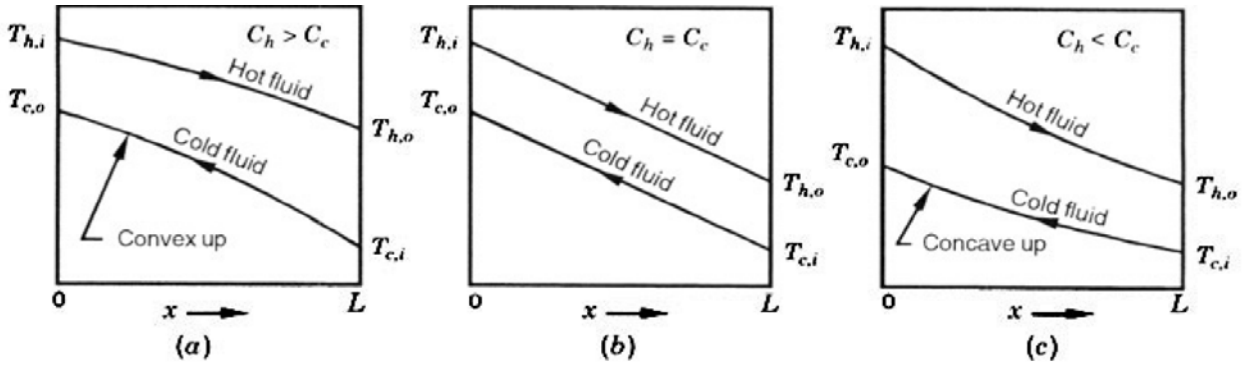

Figure 3.15. Temperature distributions across a counter-flow heat exchanger in conditions where (a) $C_h > C_c$, (b) $C_h = C_c$, and (c) $C_h < C_c$. [39]
Shah, R. K., Sekulic, D. P., 2003, Fundamentals of Heat Exchanger Design, John Wiley & Sons, Inc., Hoboken, New Jersey. Used under fair use, 2012.

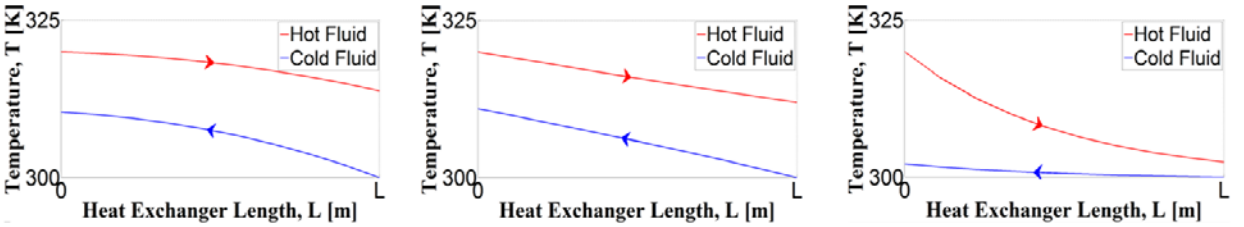

Figure 3.16. Temperature distributions across the counter-flow heat exchanger model in conditions where (a) $C_h > C_c$, (b) $C_h = C_c$, and (c) $C_h < C_c$.

3.2.7 Using Heat Exchanger Sizing Parameters in Optimization

As can be seen in Figure 3.12, the size and weight of the heat exchanger depends not only on the operational decision variables (flow rate, temperature, and pressure), but on the fin geometry as well. In fact, fin geometries are the most significant parameters effecting heat exchanger mass and volume. Logically, it stands to reason that an optimization algorithm could be employed to find the set of fin geometry parameters that meets the performance requirements, while minimizing the heat exchanger's mass and volume. Thus, an optimization problem can be formulated as follows:

Minimize:

$$m_{hx} = \rho_m L\left(\frac{A_{c,1}}{\sigma_{1`}}(1-\sigma_1)+\frac{A_{c,2}}{\sigma_2}(1-\sigma_2)\right)+\left(A_{c,1}\rho_1 + A_{c,2}\rho_2\right)L \tag{3.4}$$

With respect to:

$$\{s, h, l, t_f, t\} \tag{3.5}$$

Subject To:

$$lb \le \lfloor s, h, l, t_f, t \rfloor \le ub \tag{3.6}$$

$$\Delta P \le 30\, kPa \tag{3.7}$$

Where m is the mass of the heat exchanger, ρ is the density, A_c is the cross-sectional area of each side of the heat exchanger, σ is the porosity of each side of the heat exchanger, L is the overall heat exchanger length, s is fin channel width, h is fin channel height, l is fin strip length, t_f is fin thickness, t is plate thickness, lb is the lower bound on fin geometry parameter values, ub is the upper bound on fin geometry parameter values, and ΔP is the pressure drop.

The upper and lower bounds for fin geometry parameter values are obtained from Shah[39]. The optimization algorithm used in this part of the thesis work is a Sequential Quadratic Programming (SQP) algorithm employed to solve a constrained minimization problem of the form

$$\min f(x) \text{ such that } \begin{cases} c(x) \leq 0 \\ ceq(x) = 0 \\ A \cdot x \leq b \\ Aeq \cdot x \leq beq \\ lb \leq x \leq ub \end{cases} \tag{3.8}$$

where *x*, *b*, *beq*, *lb*, and *ub* are vectors, *A* and *Aeq* are matrices, *c*(*x*) and *ceq*(*x*) are functions that return vectors, and *f*(*x*) is a function that returns a scalar. In this case, the objective function, *f(x)*, is the weight of the heat exchanger. This algorithm ("fmincon") is part of Matlab®'s Optimization Toolbox, and documentation on fmincon and SQP can be found via Mathwork's website[51] and Boggs[52], respectively. In this problem, no linear constraints exist, rendering the terms *A*, *Aeq*, *b*, and *beq* unnecessary. The non-linear constraint in this optimization problem is on the pressure drop, not exceeding 30 kPa.

As mentioned previously, the various heat exchangers within the generic INVENT tip-to-tail model have been replaced with the model developed here. Subsequently, mission-integrated synthesis/design optimization has been performed on the tip-to-tail using heat exchanger parameters as decision variables. However, in order to ensure that the initial set of heat exchanger design variables used in the global optimization are valid, it is necessary to perform a local optimization on each heat exchanger first since each heat exchanger within the tip-to-tail model has different performance requirements. Additionally, each heat exchanger operates with different input flow rates, temperatures, and pressures. Thus, as expected, optimal size of each heat exchanger may vary dramatically from one to another. In the ensuing section, various heat exchangers within the tip-to-tail model are examined and optimized. The set of optimal design parameters for each heat exchanger will be used as a starting point in the global tip-to-tail model mission-integrated synthesis/design optimization.

3.2.8 Optimization of Various Heat Exchangers in the Generic INVENT Tip-to-Tail Model

3.2.8.1 APTMS Heat Exchangers

Within the APTMS, there are three heat exchangers that must be replaced by the transient heat exchanger model developed here. The first heat exchanger, labeled as “PAO-Air HX” (see Figure 3.10), cools a secondary PAO loop responsible for managing thermal loads from the LCA. The second heat exchanger, labeled as “Conditioning Air-Air HX” (see Figure 3.10), maintains the temperatures of the two bleed air streams to ensure that there is enough capacity in each stream to cool downstream components. The third, labeled as “Air-Air HX” (see Figure 3.10), helps maintain the temperatures of the two bleed streams used to cool the VCS, air cooled avionics and cockpit. The design information for all three heat exchangers, given in Table 3.12, Table 3.13, and Table 3.14, is obtained by simulating a mission with the original transient heat exchangers still in the model.

Table 3.12. Design information for PAO-Air HX.

	Cold Fluid	**Hot Fluid**
Fluid Type	Air	PAO
Design Temperature (K)	284.45	321.56
Design Flow Rate (kg/s)	5.1021	1.8144
Design Heat Load (W)	122260	

Table 3.13. Design information for Air-Air HX.

	Cold Fluid	**Hot Fluid**
Fluid Type	Air	Air
Design Temperature (K)	274.36	354.19
Design Flow Rate (kg/s)	4.1228	0.7696
Design Heat Load (W)	40900	

Table 3.14. Design information for Conditioning Air-Air HX.

	Cold Fluid	**Hot Fluid**
Fluid Type	Air	Air
Design Temperature (K)	270.76	345.42
Design Flow Rate (kg/s)	4.25	0.743
Design Heat Load (W)	33900	

3.2.8.2 FTMS Heat Exchangers

Within the FTMS, there are three additional heat exchangers that must be replaced by the transient heat exchanger model developed here. The first, labeled as “PAO-Fuel HX” (see Figure 3.9), helps maintain the temperatures of a closed PAO loop. This PAO loop maintains the temperature of PTMSC ICC and interacts with the second heat exchanger, labeled as “PAO-Air HX” (see Figure 3.9). The design information for these heat exchangers, given in Table 3.15 and Table 3.16, is obtained by simulating a mission with the original transient heat exchangers still in the model.

Table 3.15. Design information for FTMS PAO-Fuel HX.

	Cold Fluid	**Hot Fluid**
Fluid Type	PAO	JP8
Design Temperature (K)	287.57	294.79
Design Flow Rate (kg/s)	3.63	13.99
Design Heat Load (W)	50000	

Table 3.16. Design information for FTMS PAO-Air HX.

	Cold Fluid	**Hot Fluid**
Fluid Type	Air	PAO
Design Temperature (K)	254.04	294.78
Design Flow Rate (kg/s)	2.6185	0.7257
Design Heat Load (W)	60000	

Within the Engine FTMS (EFTMS), a subsystem of the FTMS (see Figure 3.9), there is a final heat exchanger that must be replaced by the transient heat exchanger model developed here. This heat exchanger, labeled “EFTMS PAO-Fuel HX”, is responsible for maintaining the fuel at reasonable temperatures. The fuel is used as a coolant within the PS to maintain bearing temperatures within the fan, HPC, HPT, and LPT. Design information for the EFTMS PAO-Fuel HX, given in

Table 3.17, is obtained by simulating a mission with the original heat transient heat exchanger still in the model.

Table 3.17. Design information for EFTMS PAO-Fuel HX.

	Cold Fluid	Hot Fluid
Fluid Type	JP8	PAO
Design Temperature (K)	289.09	296.12
Design Flow Rate (kg/s)	9.8025	2.0971
Design Heat Load (W)	24786	

3.2.8.3 Optimal Sizes of Heat Exchangers

Optimal results obtained by implementing the "fmincon" algorithm described previously yields the results shown in Table 3.18 for the individual heat exchanger optimizations (i.e., individual in that the optimizations are not part of an overall mission-integrated optimization). The constraints on heat exchanger parameters are given in Table 3.19. Additionally, because fmincon is a gradient based approach, the algorithm requires an initial starting point, which is set so that the pressure drop is be minimal, thus, ensuring that the pressure drop constraint is not violated during the first few iterations of a given optimization. It is important to note that in each case, the optimal values for the design variables l, t_f, and t all converge to either an upper or a lower bound.[i] Thus, in the mission-integrated tip-to-tail optimization, it is possible to reduce the number of decision variables required to describe the problem, thereby, reducing the number of simulations of the computationally expensive model required to reach an optimal solution. Analysis of the optimal set of heat exchanger sizing parameters using a more robust, surrogate-based method is found in Section 4.2.2 of Chapter 4. The solution space is highly non-linear and likely contains many local optima. Thus, this more robust surrogate-based method is necessary to guarantee that the optimizer converges to a global optimum instead of a local optimum.

[i] For example, in the case of fin thickness, t_f converges to a lower bound. The reason is that since fin efficiency is fixed, there is no penalty incurred for making a fin thinner. A thin fin equates to a lower mass and, thus, in the heat exchanger weight minimization problem, fin thickness necessarily converges to the lower bound.

Table 3.18. Optimal sizes of heat exchangers based on the individual heat exchanger optimizations.

		s_1	h_1	l_1	$t_{f,1}$	t_1	s_2	h_2	l_2	$t_{f,2}$	t_2	L	m_{hx}	ΔP_1	ΔP_2
		mm	*mm*	*mm*	*mm*	*mm*	*mm*	*mm*	*mm*	*mm*	*mm*	*m*	*kg*	*Pa*	*Pa*
APTMS Heat Exchangers	PAO Air HX	1.5	10.6	6.3	0.208	11.361	0.830	10.6	6.35	0.472	15.313	0.841	290.7	30000	19376
	Cond Air Air HX	1.278	10.6	6.3	0.142	1.240	1.524	10.579	6.35	0.319	1.858	0.187	7.88	28610	3577
	Air Air HX	0.83	10.597	6.3	0.374	3.783	0.83	10.6	6.35	0.466	17.034	0.350	95.75	30000	6794
FTMS Heat Exchangers	PAO Fuel HX	0.836	10.6	6.299	0.322	14.290	0.83	10.6	6.35	0.462	17.686	0.380	404.3	30000	738
	PAO Air HX	0.891	10.6	6.300	0.143	13.987	0.83	10.6	6.35	0.231	7.652	0.336	78.13	29999	4426
	Engine FTMS / PAO Fuel HX	0.833	10.6	2.722	0.5	1.018	0.832	10.6	6.35	0.112	9.553	0.501	73.75	10341	30000

Table 3.19. Constraints imposed on heat exchanger sizing parameters.

	s_1	h_1	l_1	$t_{f,1}$	t_1	s_2	h_2	l_2	$t_{f,2}$	t_2	L	ΔP_1	ΔP_2
	mm	*mm*	*mm*	*mm*	*mm*	*mm*	*mm*	*mm*	*mm*	*mm*	*m*	*Pa*	*Pa*
Lower Bound	0.83	1.29	2.4	0.1	0.9	0.83	1.29	2.4	0.1	0.9	0.05	1	1
Upper Bound	2.08	10.6	6.35	0.5	19	2.08	10.6	6.35	0.5	19	2.5	30000	30000
Starting Point	1.8	9	5	0.5	18	1.8	9	5	0.5	18	0.5		

3.3 Exergy and Entropy Generation

As part of this thesis work, exergy balances have been implemented for the AVS, the heat exchangers in the FTMS and the APTMS (see section 3.2.5), and the total vehicle. The term total vehicle describes a control volume including the vehicle as well as the wake of the vehicle, shown schematically in Figure 3.17. Additionally, in cooperation with Woodburn[53], exergy balance equations have been implemented for the PS.

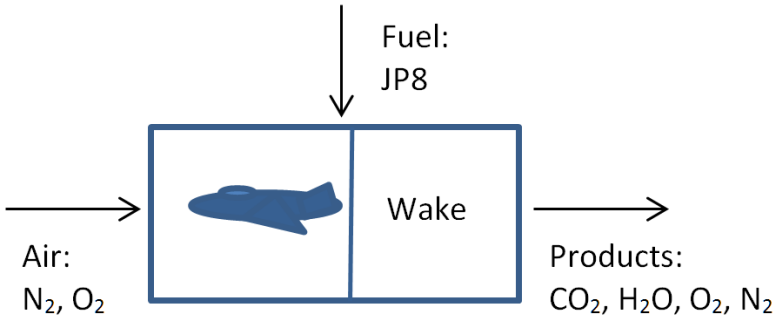

Figure 3.17. Total vehicle control volume.

3.3.1 AVS Exergy Balances

The exergy destruction equation for the AVS is an independent equation related to the drag coefficient and is not derived from an exergy or entropy balance. The total exergy destruction rate due to drag is determined by the equation below, where T_0 is a reference (or dead state) temperature, T_{amb} is the ambient (or local) temperature, D is the total (parasitic and induced) drag, and u_i is the vehicle's air velocity, i.e.,

$$\dot{X}_{des} = \frac{T_0 D u_i}{T_{amb}} \tag{3.9}$$

3.3.2 Total Vehicle Exergy Analysis

The total vehicle exergy balance used in this analysis is based on a balance initially derived by Riggins[54] and subsequently modified here to allow for the use of table data and curve fits with inconsistent or unknown reference values. The balance developed by Riggins is

$$F_{\text{x(flight)}} \cdot u_i = \dot{m}_f \left\{ H^* + \frac{u_i^2}{2} \right\} - T_i \left(\dot{S}_{\text{vehicle–irr}} + \dot{S}_{\text{wake}} + \dot{S}_{\text{tanks}} \right) \tag{3.10}$$

In this balance, H^* is the net exergy per unit mass in and out of the control volume of Figure 3.17 which takes into account deviations from the tabulated Gibbs free energy of reaction of the fuel at non-standard conditions. The net exergy flow in and out of the control volume is defined by

$$\begin{aligned} \dot{m}_f H^* = {} & \dot{m}_f \left\{ h_{0(f)} + \int_{T_{ref}}^{T_f} c_{p(f)}(T')dT' \right\} - T_i \dot{S}_{fuel} \\ & - \dot{m}_w \sum_{l=1}^{NS} \alpha_{l,w} \left[h_{l,w} - T_i s_{l,i\backslash w}(T_i, P_i, y_{lw}) \right] \\ & + \dot{m}_i \sum_{l=1}^{NS} \alpha_{l,i} \left[h_{l,i} - T_i s_{l,i}(T_i, P_i, y_{li}) \right] \end{aligned} \tag{3.11}$$

It is clear that in order for the balance equation developed by Riggins to be true, the reference temperature and pressure used to determine entropies, enthalpies, and specific heats for all the constituents of the process (fuel, nitrogen, oxygen, and products of combustion) must all be the same. Typically it is difficult to find tables or curve-fits that all use the same reference values. Thus, it is convenient to develop a balance that is flexible enough to use tables with arbitrary reference values. To address this, a modified equation for H^* is presented here. A derivation of this equation is found in appendix A. The final result on a mole basis is

$$\begin{aligned} \dot{n}_f H^* = {} & \dot{n}_f \left(\int_{T_0}^{T_f} c_{p(f)}(T)dT - T_i \int_{T_0}^{T_f} \frac{c_{p(f)}(T')}{T'} dT' \right) \\ & - \dot{n}_w \sum_{l=1}^{NS} y_{l,w} \left[\int_{T_0}^{T_i} c_{p,l,w}(T')dT' - T_i \left(\int_{T_0}^{T_i} \frac{c_{p,l,w}(T')}{T'} dT' - R \ln\left(\frac{P_w}{P_0} \right) - R \ln\left(y_{l,w} \right) \right) \right] \\ & + \dot{n}_i \sum_{l=1}^{NS} y_{l,i} \left[\int_{T_0}^{T_i} c_{p,l,i}(T')dT' - T_i \left(\int_{T_0}^{T_i} \frac{c_{p,l,i}(T')}{T'} dT' - R \ln\left(\frac{P_i}{P_0} \right) - R \ln\left(y_{l,i} \right) \right) \right] \\ & + -\frac{1}{t} \left[\sum_{l=1}^{NS} \nu_l \left(\Delta g_f^0 \right)_l + \left(\sum_{l=1}^{NS} \nu_l \left[\int_{T_0}^{T_i} c_{p,l}(T')dT' \right] \right) - T_i \left(\sum_{l=1}^{NS} \nu_l \left[\int_{T_0}^{T_i} \frac{c_{p,l}(T')}{T'} dT' \right] \right) \right] \end{aligned} \tag{3.12}$$

Of course, this equation assumes Gibbs-Dalton mixtures of ideal gases for the reactant (air) and products and an incompressible liquid for the fuel if it is, for example, JP-8 and ideal gas if it is, for example, hydrogen. Furthermore, this equation assumes complete combustion, but could easily be modified to include reaction coordinates were they known. Now, upon implementation of this equation, it was found that due to the small change in pressure and temperature experienced by the aircraft, the deviation of H^* from the Gibbs free energy of reaction is approximately 8% at any given instant of time. Additionally, it was found that implementation of this equation caused a 4-fold increase in model simulation time which at this point in my thesis work could not be addressed adequately. For purposes of the exergy analysis, this does not pose a problem and, thus, for both the exergy analysis of the initial and final results of the fuel minimization problem and that presented in the following section, equation (3.12) is used. However, for the exergy destruction minimization problem, the lower heating value (LHV) replaces equation (3.12). As can be seen in Figure 3.18, this approximation is valid since over the course of the mission, H^* deviates from the LHV by less the 2%. Additionally, Figure 3.18 shows that the LHV is an even closer approximation to H^* than the Gibbs free energy of reaction. It is important to note that to determine the latter, the Gibbs free energies of formation for a surrogate model of JP-8 are used because tabulated properties of JP-8 are not available. This surrogate model consists of the mixture of hydrocarbons shown in Table 3.20. Tabulated values for the Gibbs free energies of formation for each surrogate constituent are shown in Table 3.20.

Table 3.20. Surrogate model used to calculate the Gibbs free energy of reaction for JP-8.

	Surrogate Properties at 25 °C					
Compound Name	**Isooctane C_8H_{18}**	**Methylcyclohexane C_7H_{14}**	**m-Xylene C_8H_{10}**	**Dodecane $C_{12}H_{26}$**	**Tetralin $C_{10}H_{12}$**	**n-Tetradecane $C_{14}H_{30}$**
Density (kg/m^3)	712.4	794.1	833.0	749.5	940.9	651.3
Molecular Weight (g/mol)	114.2	98.2	106.2	170.3	132.0	198.4
Mole Fraction	0.11	0.28	0.20	0.23	0.06	0.11
Δg_f^0 **(kJ/kg)**	147.8	278.0	1119.6	294.0	1265.9	337.0

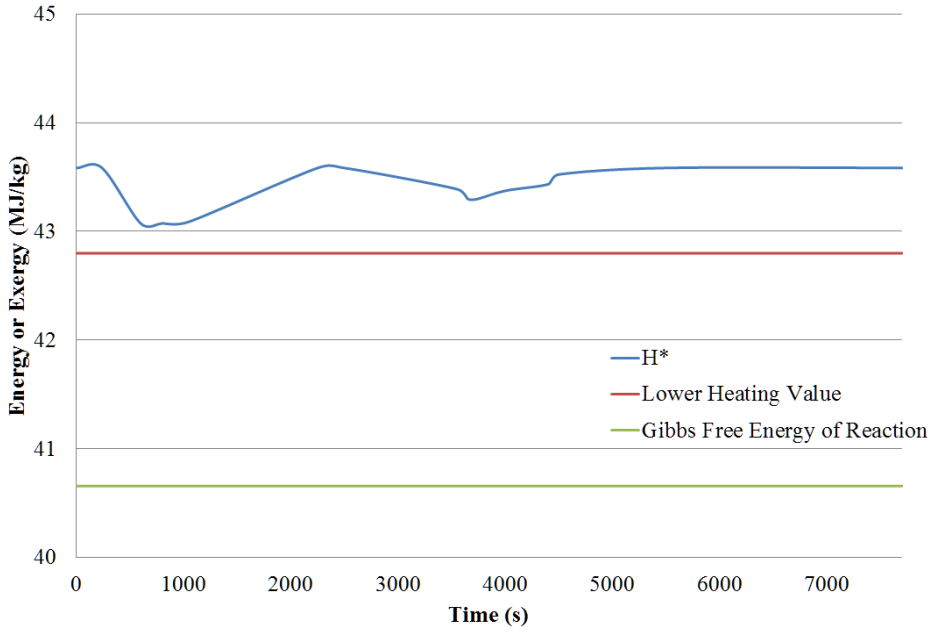

Figure 3.18. Comparison of H^* with the lower heating value and the Gibbs free energy of reaction over the entire mission.

3.3.3 Preliminary Exergy Analysis Results

Preliminary exergy analysis results obtained from the generic INVENT tip-to-tail model can be found in Figure 3.19 and Figure 3.20. The first figure demonstrates the effect of using ambient conditions for the dead state reference, as opposed to a fixed dead state reference. In the figure, a temperature of 298.15 K and a pressure of 101.325 kPa are used as the fixed dead state conditions.

Figure 3.20 shows the variation of the exergy destruction rate for each subsystem over the entire mission. From the figure it is apparent that the exergy destruction rate significantly increases during climbs/accents. It should also be noted that the exergy destruction rate for each subsystem is positive at all times, indicating that the system is feasible. Figure 3.20 also shows the variation in total exergy destruction over the entire mission. The fact that the total exergy destroyed in each subsystem increases monotonically coincides with the data showing positive exergy destruction rates. It is clear from Figure 3.20 that the total exergy destroyed by the PS and AVS are a significant portion of the total vehicle exergy destruction. In fact, the PS accounts for

approximately 48% of the total exergy destroyed and the AVS accounts for approximately 18%. The exergy destruction in the APTMS and the FTMS is very small, contributing to less than 2% of the total exergy destruction.

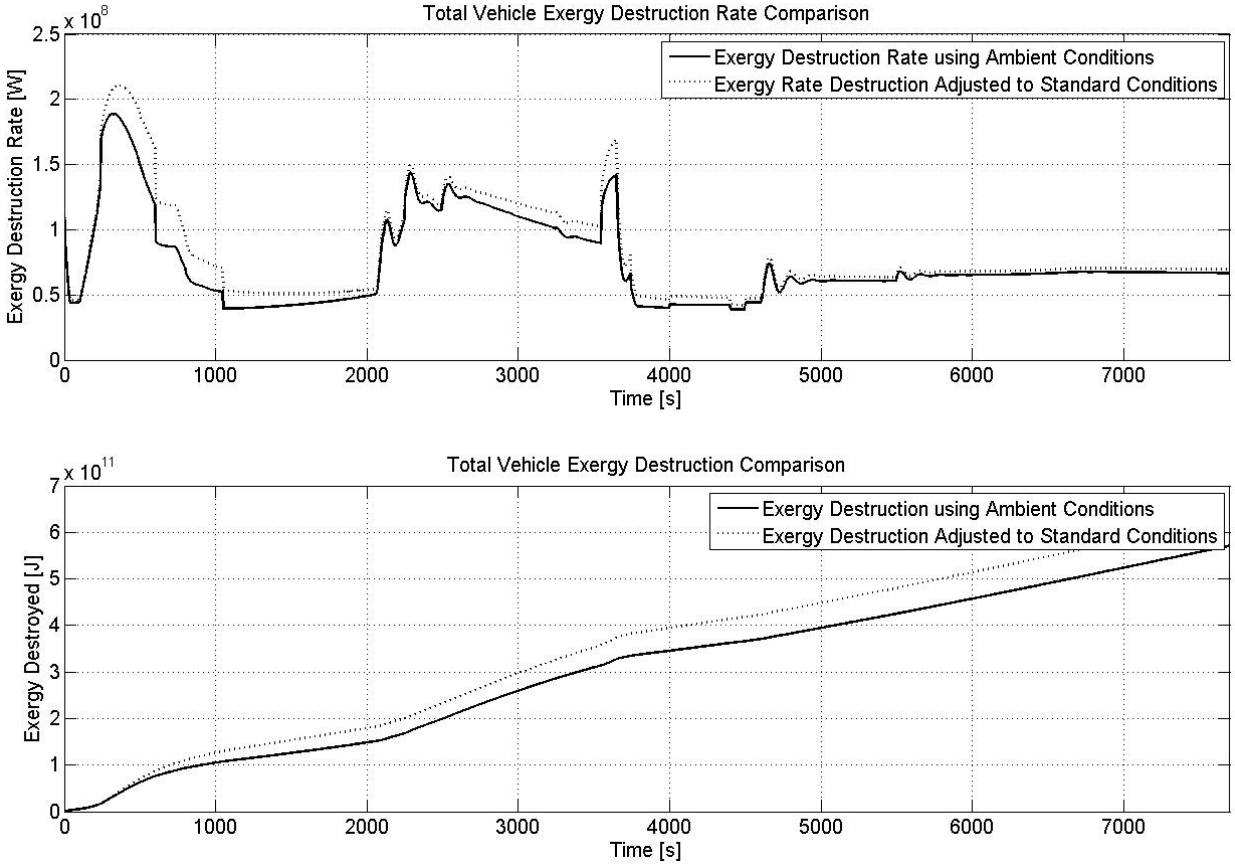

Figure 3.19. Effect of using a local ambient dead state on the exergy destruction rate.

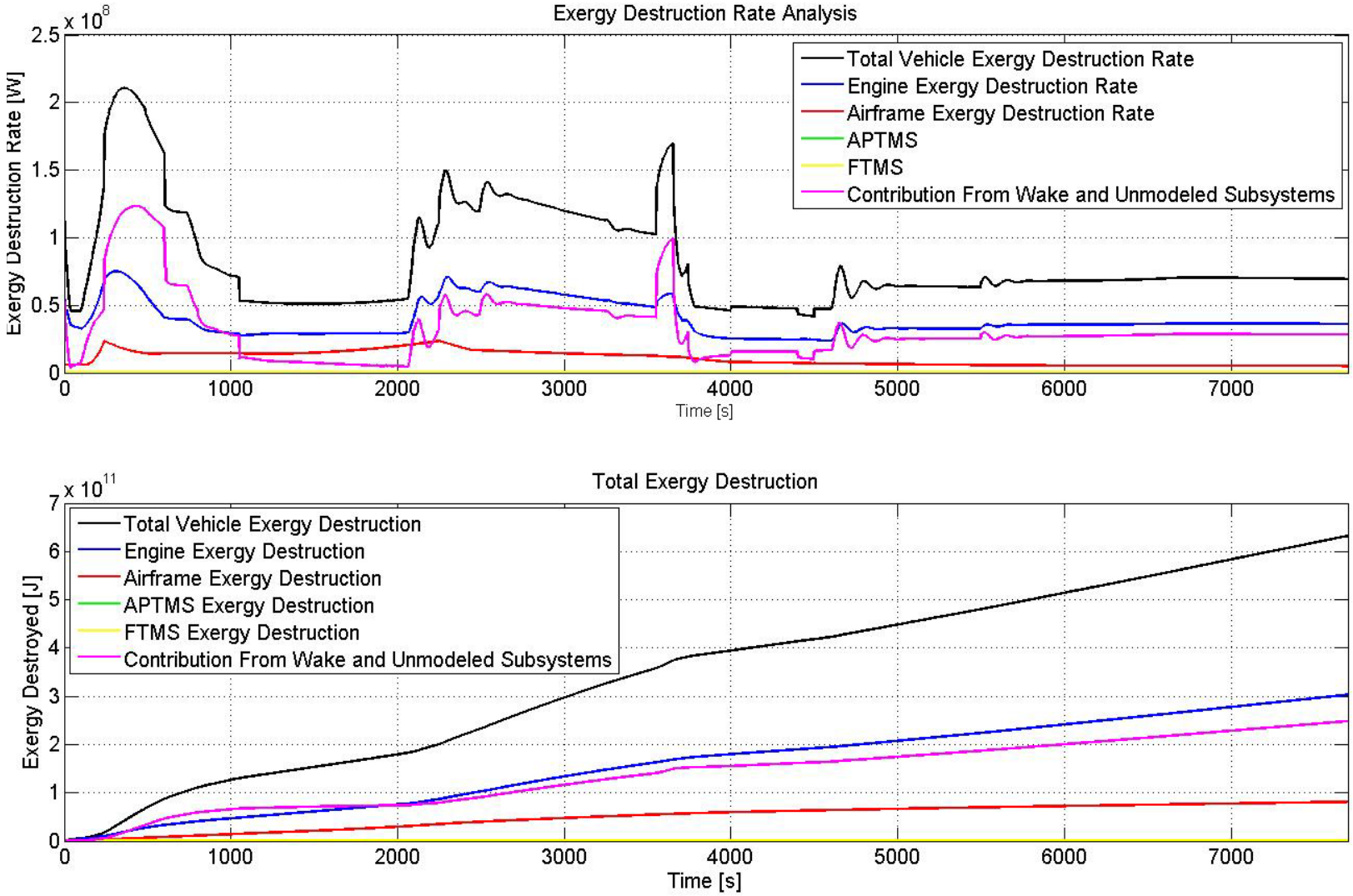

Figure 3.20. Analysis for the INVENT tip-to-tail including the PS, AVS, APTMS, FTMS, wake and remaining subsystems.

Chapter 4 - Surrogate Modeling and Optimization

Large-scale synthesis/design optimization is a vital tool for the aerospace research/design community. If correctly implemented, it provides a set of parameters that optimize a specific objective function and, thus, a particular system. In the aerospace community, typical objectives include minimizing fuel usage and maximizing performance or safety. Unfortunately, data collection in the aerospace industry can be very time consuming and expensive. This problem is effectively demonstrated in the generic INVENT tip-to-tail optimization problem. As described in Section 2.4.2, running a single simulation of the tip-to-tail model takes 4-5 minute – or more if the tip-to-tail becomes unstable[j]. Surrogate modeling proves effective in cases where capturing a single data point for the optimization, i.e., completing a single simulation, can be costly in terms of time and resources.

There are two primary uses of surrogate models: capturing the behavior of physical systems (e.g., compressors, pumps, etc.) and capturing the behavior of computational models (e.g., tip-to-tail, CFD, etc.). In physical systems, it is not useful to capture data points describing every operating condition of that system. Instead, it may be beneficial to gather fewer data points and fit a response surface to the data. The response surface (i.e., surrogate model) describes, with some degree of certainty, the functional relationship existing between the independent and dependent variables of the system. The resultant surrogate model can be validated using additional data points and if acceptably accurate, used as a stand-in for the original model. This methodology can be used to construct surrogate models for systems such as compressors. A surrogate model of a compressor (compressor map) can be used to predict performance of compressors under conditions that were not explicitly tested. Similarly, for computational models such as the generic INVENT tip-to-tail model, surrogate models can be used to predict the performance of the model at a given design point without having to actually run a simulation. Additionally, these surrogate models are useful in optimization. Rather than perform

[j] Investigation into model instability shows that during steep descents, the generic INVENT tip-to-tail model requires little to no thrust to maintain airspeed. Under these conditions, the bleed air mass flow rate going to the IPP is minimal and the IPP can struggle to maintain performance. Recognizing the poor IPP performance, the system controller will extract more and more bleed air off the engine causing the high pressure compressor in the engine to go into surge. While the engine is surging, the Matlab® Simulink® solver (ode23s) has a very difficult time converging, leading to very long simulation times.

optimization on the actual system or computational model, a surrogate model can be used instead. Because the surrogate model is typically[k] less computationally expensive, it requires less time and resources to converge to the optimum, whether local or global.

The following section describes the methodology used in a typical surrogate modeling process. The case study used to describe the process involves the construction of a surrogate model for the APTMS Multinode_Transient_HX1 described previously. This surrogate model is used in an optimization problem that minimizes the weight of the heat exchanger. This result is then compared to the results detailed in Section 3.2.8.

4.1 Surrogate Modeling Methodology

The surrogate modeling process is a multi-step process that may consist of several iterations. The typical surrogate modeling process is as follows:

- Analysis of system inputs
- Screening tests
- Design of experiments
- Sample data
- Construct surrogate model
- Evaluate model
- If need be, iterate

If upon evaluation, the model is not sufficient, taking additional sample points must be considered. This, however, should be avoided if possible due to the significant time associated with this effort.

4.1.1 Analysis of System Inputs

Input analysis is critical to the successful creation of a surrogate model. The idea behind input analysis is to determine the range over which independent variables of the system may be

[k] It was found that creating a surrogate model of the transient heat exchanger model developed here was more computationally expensive than the model itself. Due to the highly nonlinear behavior of the response surface and, thus, the size and complexity of the surrogate model, evaluating the surrogate model required more CPU operations than evaluating the model itself.

varied. The importance of this is due to the fact that surrogate models can only be valid over certain ranges of each parameter. That is to say, if a surrogate model of a heat exchanger is constructed that is valid for cold stream inlet temperatures of 270 K to 285 K, the model can only handle inputs between those bounds. When analyzing inputs, it is important to question if those inputs might change in the future and if so, create the model to be able to handle those inputs. At a certain point though, it becomes unfeasible to make the model any more robust. If the upper bound on the cold fluid inlet temp is extended to 295 K and the same quantity of sample points is used, the model is guaranteed to lose fidelity.

As part of the work to generate a surrogate model for the compact heat exchanger, it is necessary to analyze the inputs to the heat exchanger model. The inputs are the inlet temperatures and flow rates of both the hot and cold fluid and the heat load the heat exchanger was tasked to handle. Plots of heat load, temperature, and flow rate throughout the mission are shown in Figure 4.1, Figure 4.2, and Figure 4.3, respectively. The heat load schedule shown in Figure 4.1 indicates an increased heat load during high altitude/Mach number mission segments. Figure 4.2 demonstrates that an increased avionics heat load is accompanied by an increase temperature difference between the two fluid streams. Figure 4.3 shows the flow rates of the hot and cold fluid streams over the course of the mission. Note that the flow rate of PAO is constant over the course of mission. This is due to the fact that control for the PAO loop is not built into the generic INVENT tip-to-tail and is, thus, fixed at a constant value.

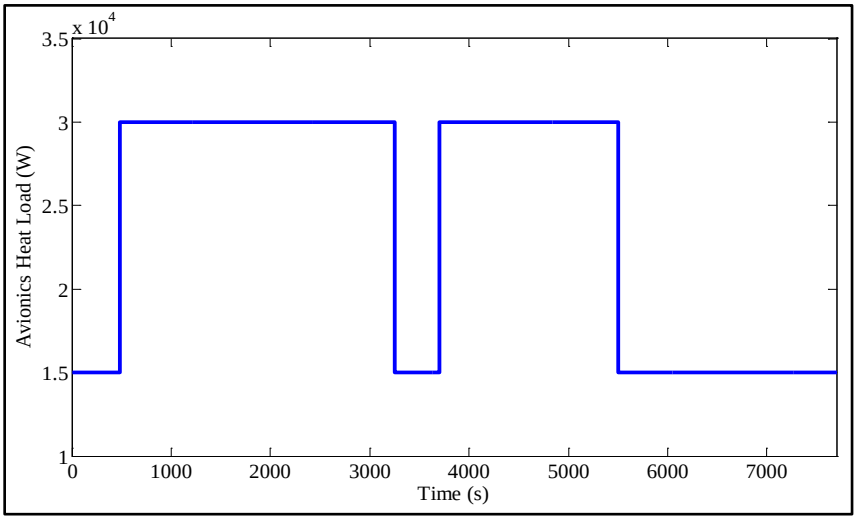

Figure 4.1. Heat load schedule for the air-cooled avionics.

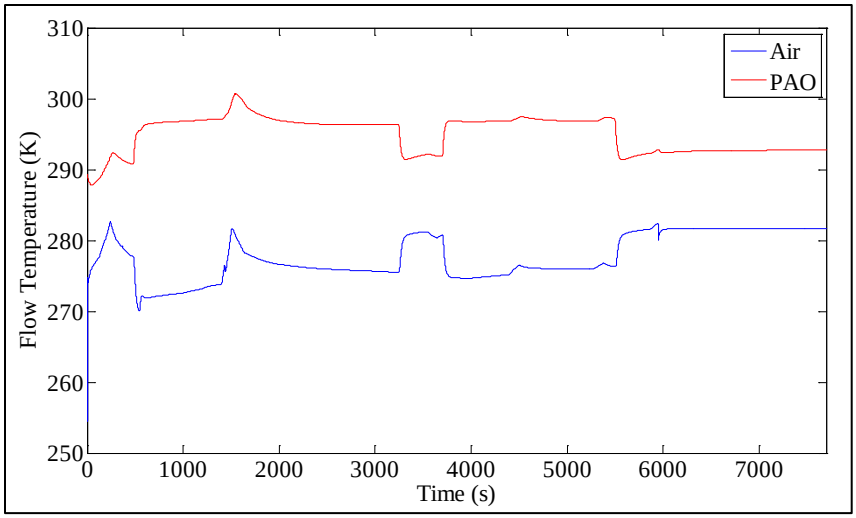

Figure 4.2. Temperature at the entrance of the compact heat exchanger.

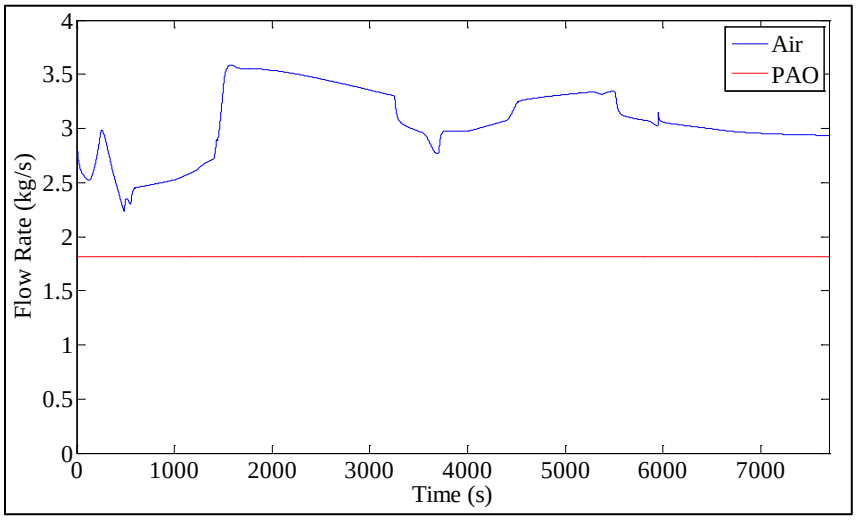

Figure 4.3. Flow rate of the PAO and air through the compact heat exchanger.

4.1.2 Screening Test

Similar to a sensitivity test, the purpose of the screening test is to determine if there are any parameters in the model that have no significant effect on the response of the model. The screening test shows what parameters, if any, can be eliminated as DOF and set at fixed values for the purpose of constructing the surrogate model. Starting with the full set of parameters, a design of experiments is performed, yielding an initial set of sample points (or initial design). Typically, factorial designs are used to screen for significant factors. A full factorial design

allows the study of the effect of each parameter on the response, as well as the effects of interactions between parameters on the response. However, for a large number of DOF, fractional factorial designs are preferred. Fractional factorial designs can be used to estimate the effects of a single parameter on the response, as well as the effect of interactions on the response. However, as opposed to a full factorial design, a fractional factorial design is limited by its 'resolution': the ability to distinguish between main effects (effects due to a single parameter) and interactions. At higher resolution, this ability is enhanced at the cost of a larger data set being required. The preferred fractional factorial design resolution is based on the number of DOF and whether higher order effects (e.g., the effect an interaction of several parameters had on the response) needs to be studied.

In the process of creating a surrogate model for the heat exchanger sizing, the logical first step is to examine the model and determine the number of DOF. For the heat exchanger model, there are eleven. In the first round of screening tests, it was decided to only estimate the main effects. The benefits to this are a decrease in design construction time and the immediate knowledge of whether or not certain factors can be eliminated from the model. The most appropriate design for estimating the main effects of an 11-factor, non-linear model is a resolution VII fractional factorial design. At resolution VII, it is possible to distinguish interactions of four factors or less from the main effects. Thus, the design allows us to estimate which model parameters are significant. By examining the main effects, it is found that both l_1 and l_2 are insignificant, where l_1 and l_2 are the fin strip length for each side of the heat exchanger. In the two-factor interaction l_1 and l_2 are still insignificant; however, due to hierarchy and the fact that the interactions $l_1 \times t_{f,1}$ and $l_2 \times t_{f,2}$ are significant, they are not eliminated. Here, $t_{f,1}$ and $t_{f,2}$ describe the thickness of the fins used in the heat exchanger. Thus, the screening test shows that each independent variable is important and must be included in the model. Although this increases the number of sample points required to develop a surrogate model, it is acceptable to the quick run time of the heat exchanger sizing algorithm.

4.1.3 Design of Experiments (DOE)/Sample Data

The purpose of the design of experiments (DOE) is to determine the best location at which to sample data. Several software packages exist that will perform a design of experiments. The specific software used in this research is Design Expert 8 (DX8), developed by Stat-Ease. Typically, in screening tests, weak fractional factorial designs are used to minimize the number of data points. In an experiment where higher fidelity is required, full factorial or stronger fractional factorials may be used. The DOE software accepts the input ranges determined during the analysis of inputs and delivers a set of sample points. These sample points are the result of a complex algorithm implemented by the DOE software and have been chosen specifically at locations that maximize the fidelity of the model and reduce the expected residual error. Finally, a simulation is run for each sample point and the data is imported into DX8.

4.1.4 Construct/Evaluate Surrogate Model

Once the data has been imported, the DOE software uses a polynomial regression to fit the non-linear model. DX8 provides analysis of variance (ANOVA) data that can be used to determine if the polynomial used to construct the surrogate is appropriate. If the error is significant, ANOVA can provide insight into what can be done to improve the fidelity of the model, including eliminating terms in the polynomial, reducing or increasing the order of the polynomial, etc. This information helps determine if the model will suffice as a surrogate for the original model. The final step is to run the surrogate model using additional sample points and compare the results to those obtained from the original model under the same conditions. If the error between the surrogate model and the original model is insignificant, then the surrogate can replace the original model and be used as a computationally inexpensive alternative.

4.2 Optimization Using Surrogate Models

4.2.1 Phoenix Integration's ModelCenter® Design Explorer® Algorithm

ModelCenter®, software developed by Phoenix Integration, is an excellent integration, analysis, and optimization tool. ModelCenter® was chosen for use in this thesis work for several

reasons: ModelCenter® can ‘wrap’ around other programs and manipulate them externally, allowing optimization algorithms developed by Phoenix Integration to be applied to computational models developed in almost any other coding language. Specifically, ModelCenter® interacts with Matlab® via the Matlab® application-program interface (API). Additionally, ModelCenter® provides a large assortment of optimization algorithms including several variants of the genetic algorithm, several variants of Newtonian gradient-based methods, as well more recently developed optimization algorithms such as pattern search optimization, particle swarm optimization, and hybrid techniques such as the Design Explorer® algorithm.

The Design Explorer® algorithm is of particular interest due to its rapid convergence to the global optimum of a smooth response surface. The Design Explorer® algorithm is a hybrid, surrogate modeling-based optimization technique. The algorithm begins by intelligently generating an initial set of points at which to sample data. This initial design is chosen based on the number of DOF, the desired fidelity of the initial surrogate model. Upon selection of the set of initial sample points, the optimizer runs a simulation for each sample point, and constructs a surrogate model to fit the data. By default ModelCenter® uses Kriging models to fit the data, but other options are available, including Taylor series models, polynomial models, and rational function models. Subsequently, the optimizer performs an optimization of the surrogate model using ModelCenter®’s built in SQP gradient-based algorithm. The optima found based on the surrogate model are compared to data from the actual computational model. If the error is significant, Design Explorer® intelligently increases the fidelity of the model by sampling additional points in regions where the error is high. The optimizer iterates through this process until this error between the surrogate model and the real model is insignificant.

The Design Explorer® is an exceptionally efficient optimization algorithm due to the fact that each gradient-based optimization is performed on the surrogate model as opposed to the actual computational model. Additionally, Design Explorer® guarantees convergence to a global optimum rather than to one of the several local optima present. Results obtained by utilizing the Design Explorer® algorithm in the optimization of the size of the compact heat exchangers used in the generic INVENT tip-to-tail model are shown in the succeeding section.

4.2.2 Local Optimization Results Comparison

Results obtained by implementing Matlab®'s "fmincon" algorithm are first presented in Table 3.18 of Chapter 3. These results are compared to results obtained from the implementation of the Design Explorer® algorithm in Table 4.1. From these results (see the column for the mass of the heat exchanger), it is clear that the "fmincon" algorithm converged to a local minimum. In every case, without exception, the Design Explorer® produced a heat exchanger with a lower mass. It is important to note that in every case the values for h_1, l_1, $t_{f,1}$, t_1, h_2, l_2, $t_{f,2}$, and t_2 converged to either the upper or lower bound (see Table 4.2). This is an important result that allows for the elimination of these variables as DOF in the global optimization problem. Thus, in the mission-integrated tip-to-tail optimization problem, the DOF for each heat exchanger is limited to s_1, s_2, and L. Again, it is expected that accounting for variable fin efficiency would affect the model in such a way as to cause some of these parameters to become important in the optimization problem.

Table 4.1. Comparison of optimal heat exchanger sizing parameters from the Matlab® 'fmincon' optimization algorithm (red) and the Design Explorer algorithm (blue).

		s_1	h_1	l_1	$t_{f,1}$	t_1	s_2	h_2	l_2	$t_{f,2}$	t_2	L	m_{hx}	ΔP_1	ΔP_1
		mm	*mm*	*mm*	*mm*	*mm*	*mm*	*mm*	*mm*	*mm*	*mm*	*m*	*kg*	*Pa*	*Pa*
APTMS Heat Exchangers	Multinode_ Transient_HX1	1.5	10.6	6.3	0.208	11.361	0.830	10.6	6.35	0.472	15.313	0.841	290.7	30000	19376
		1.608	10.6	6.35	0.1	0.9	0.83	10.6	6.35	0.1	0.9	0.848	**28.8**	30000	30000
	Multinode_ Transient_HX2	1.278	10.6	6.3	0.142	1.240	1.524	10.579	6.35	0.319	1.858	0.187	7.88	28610	3577
		0.83	10.6	6.35	0.1	0.9	0.903	10.6	6.35	0.1	0.9	0.142	**3.31**	30000	30000
	VCS/PAO Fuel HX	0.83	10.597	6.3	0.374	3.783	0.83	10.6	6.35	0.466	17.034	0.350	95.75	30000	6794
		0.83	10.6	6.35	0.1	0.9	0.83	10.6	6.35	0.1	0.9	0.312	**16.79**	30000	7038
	VCS/Multinode_ Transient_HX	0.836	10.6	6.299	0.322	14.290	0.83	10.6	6.35	0.462	17.686	0.380	404.3	30000	738
		1.470	10.6	6.35	0.1	0.9	0.83	10.6	6.35	0.1	0.9	0.702	**28.85**	30000	8704
FTMS Heat Exchangers	Multinode_ Transient_HX	0.891	10.6	6.300	0.143	13.987	0.83	10.6	6.35	0.231	7.652	0.336	78.13	29999	4426
		1.491	10.6	6.35	0.1	0.9	0.83	10.6	6.35	0.1	0.9	0.604	**10.71**	30000	30001
	PAO Fuel HX	0.833	10.6	2.722	0.5	1.018	0.832	10.6	6.35	0.112	9.553	0.501	73.75	10341	30000
		0.835	10.6	6.35	0.1	0.9	1.035	10.6	6.35	0.1	0.9	0.675	**28.93**	25615	28227

Table 4.2. Constraints imposed on heat exchanger sizing parameters

	s_1	h_1	l_1	tf_1	t_1	s_2	h_2	l_2	tf_2	t_2	L	ΔP_1	ΔP_2
	mm	*mm*	*mm*	*mm*	*mm*	*mm*	*mm*	*mm*	*mm*	*mm*	*m*	*Pa*	*Pa*
Lower Bound	0.83	1.29	2.4	0.1	0.9	0.83	1.29	2.4	0.1	0.9	0.05	1	1
Upper Bound	2.08	10.6	6.35	0.5	19	2.08	10.6	6.35	0.5	19	1	30000	30000

4.3 Global Tip-to-Tail Optimization Problem

The generic INVENT tip-to-tail model consists of six highly coupled subsystems where changes in one subsystem can provoke changes in other subsystems. The implication of this is that integrating individually optimized subsystems together does not result in an overall optimized system. Therefore, in complex systems such as the tip-to-tail, it becomes necessary to perform optimization at the system level to guarantee an overall optimal solution.

The Design Explorer® algorithm is used due to its demonstrated ability to efficiently converge to a global optimum. Additionally, based on the results shown in Section 4.2.2, a reduced set of decision variables is used to describe each heat exchanger. Two system-level objectives in two separate optimization problems are defined: minimize fuel consumption or the total amount of exergy destroyed. Thus,

Minimize

$$X_{\text{Total Vehicle}} \text{ or } \int_{t_0}^{t_f} \dot{m}_f \, dt \text{ (Total fuel used)} \tag{4.1}$$

with respect to

$$\vec{\mathrm{B}} = \begin{bmatrix} \vec{\beta}_{\text{AVS}} \\ \vec{\beta}_{\text{PS}} \\ \vec{\beta}_{\text{APTMS}} \\ \vec{\beta}_{\text{FTMS}} \\ \vec{\beta}_{\text{REPS}} \\ \vec{\beta}_{\text{HPEAS}} \end{bmatrix} \text{ and } \vec{\Theta} = \begin{bmatrix} \vec{\theta}_{\text{AVS}} \\ \vec{\theta}_{\text{PS}} \\ \vec{\theta}_{\text{APTMS}} \\ \vec{\theta}_{\text{FTMS}} \\ \vec{\theta}_{\text{REPS}} \\ \vec{\theta}_{\text{HPEAS}} \end{bmatrix} \tag{4.2}$$

subject to

$$\vec{H} = \begin{bmatrix} \vec{h}_{\text{AVS}} \\ \vec{h}_{\text{PS}} \\ \vec{h}_{\text{APTMS}} \\ \vec{h}_{\text{FTMS}} \\ \vec{h}_{\text{REPS}} \\ \vec{h}_{\text{HPEAS}} \end{bmatrix} = \vec{0} \text{ and } \vec{G} = \begin{bmatrix} \vec{g}_{\text{AVS}} \\ \vec{g}_{\text{PS}} \\ \vec{g}_{\text{APTMS}} \\ \vec{g}_{\text{FTMS}} \\ \vec{g}_{\text{REPS}} \\ \vec{g}_{\text{HPEAS}} \end{bmatrix} \leq \vec{0} \tag{4.3}$$

where $\vec{B}$ and $\vec{\Theta}$ represent the subsystem synthesis/design and operational decision variables, respectively. The equality constraints defined in $\vec{H}$ represent the geometric and thermodynamic equations for each subsystem. The inequality constraints defined in $\vec{G}$ are the limits imposed on the independent and dependent subsystem variables.

Table 4.3 and Table 4.4 show the design and operational constraints imposed on the heat exchangers used in the optimization of the generic INVENT tip-to-tail model. Valid ranges for design variables s_1, s_2, and L are provided by Kays and London[38] while operational constraints are based on the maximum acceptable pressure drop. Results from the optimization of the tip-to-tail can be found in the ensuing section.

Table 4.3. APTMS design/operational constraints.

	Design Decision Variable Constraints			**Operational Constraints**	
PAO-Air HX	$0.83 \leq s_1 \leq 2.08$ (mm)	$0.83 \leq s_2 \leq 2.08$ (mm)	$0.05 \leq L \leq 2.5$ (m)	$1 \leq \Delta P_1 \leq 30000$ (Pa)	$1 \leq \Delta P_2 \leq 30000$ (Pa)
Cond. Air-Air HX					
Air-Air HX					

Table 4.4. FTMS design/operational constraints.

	Design Decision Variable Constraints			**Operational Constraints**	
PAO-Fuel HX	$0.83 \leq s_1 \leq 2.08$ (mm)	$0.83 \leq s_2 \leq 2.08$ (mm)	$0.05 \leq L \leq 2.5$ (m)	$1 \leq \Delta P_1 \leq 30000$ (Pa)	$1 \leq \Delta P_2 \leq 30000$ (Pa)
PAO-Air HX					
EFTMS PAO-Fuel HX					

Chapter 5 - Results and Discussion

Chapters 3 and 4 are concerned with the transient heat exchanger model development and demonstrating the efficacy of using a global optimization technique when solving for the optimal set of heat exchanger parameter values. Chapter 5 focuses on the results from the simulation of the generic INVENT tip-to-tail model post and prior to integration of the transient heat exchanger models developed as part of this thesis work, as well results obtained from performing mission-integrated synthesis/design optimization on the tip-to-tail using the heat exchanger synthesis/design variables as DOF (i.e., optimization decision variables).

5.1 Integration of the Transient Heat Exchanger Model into the Generic INVENT Tip-to-Tail Model

5.1.1 APTMS Heat Exchanger Integration

The OSF compact heat exchanger model is integrated into the generic INVENT tip-to-tail model replacing six heat exchangers: three within the APTMS and three within the FTMS. The heat exchangers integrated into the APTMS replace the PAO-air, air-air, and conditioning air-air heat exchangers. The locations of these heat exchangers are shown schematically in Figure 5.1. The PAO-air heat exchanger maintains the liquid-cooled avionics at an acceptable temperature. A closed PAO loop captures heat from the liquid-cooled avionics and rejects heat, via the heat exchanger, to a bleed-air stream.

The conditioning air-air heat exchanger is used to ensure that there is enough cooling capacity in the bleed-air streams sent to the PAO-air heat exchanger and the cockpit/air-cooled avionics. The stream sent to the PAO-Air heat exchanger originates in the IPP, where it is used to cool the IPP turbine blades. The stream sent to the cockpit/air-cooled avionics originates from a bleed-air stream in the PS and passes through the air-Air heat exchanger. The latter and the conditioning air-air heat exchanger work in tandem with the bleed control valve to regulate the flow rates and temperatures of the fluid streams sent to the PAO-air heat exchanger and the cockpit/air-cooled avionics.

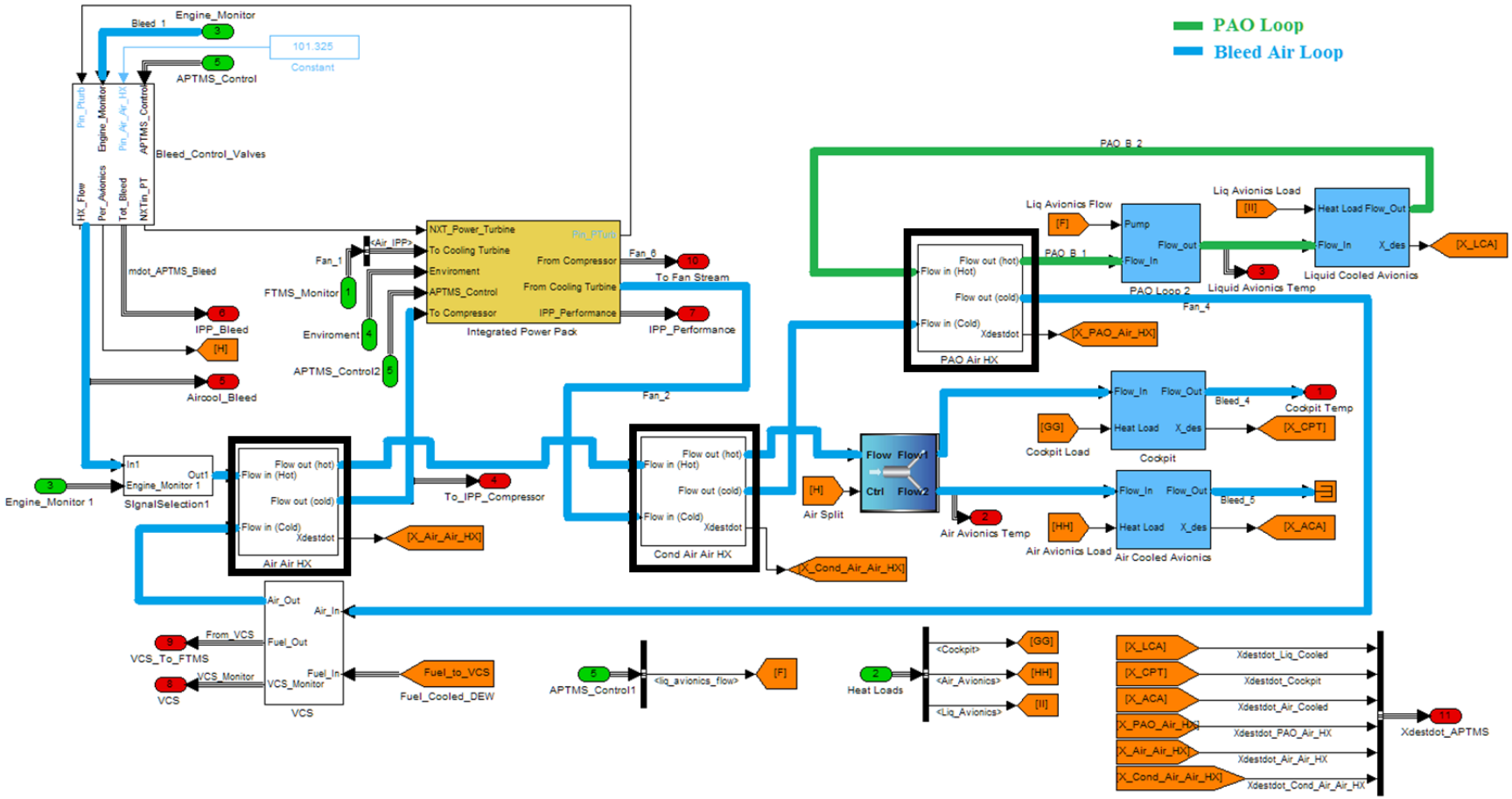

Figure 5.1. Generic INVENT tip-to-tail APTMS with heat exchanger models implemented.

5.1.2 FTMS Heat Exchanger Locations

The heat exchangers integrated into the FTMS replace the PAO-fuel and the PAO-air heat exchangers in the FTMS as well as the PAO-fuel heat exchanger located in the engine FTMS, a subsystem of the FTMS. The locations of these heat exchangers are shown schematically in Figure 5.2 and Figure 5.3.

The PAO-air heat exchanger and the PAO-fuel heat exchanger in the FTMS work with the flow control valve to cool the power thermal management subsystem controller/inverter converter controller (PTMSC/ICC) while ensuring that there is enough capacity in the PAO loop to cool the fuel stream (shown in red in Figure 5.2 and Figure 5.3). The fuel is used in a separate loop to cool several critical components including the hydraulics heat exchanger, ESG heat exchanger, full-authority digital engine controller (FADEC), DEWS, and the engine (in the engine FTMS subsystem).

The PAO-Fuel heat exchanger in the engine FTMS helps cool the bearings in the fan, HPC, HPT, and LPT of the PS. The components are cooled and lubricated by a closed PAO loop which rejects heat to the fuel via PAO-Fuel heat exchanger. Upon exiting the engine FTMS, the fuel stream is split, a portion of the fuel being sent to the engine for combustion and another portion being sent to the VCS (for cooling) before being returned to the fuel tanks.

The transient OSF compact heat exchanger model developed in this thesis work performs considerably better than the heat exchanger models previously implemented. It is expected then, that integrating these new heat exchanger models into the generic INVENT tip-to-tail model will significantly alter the performance of the vehicle. An analysis of vehicle performance post/prior to the integration of the heat exchanger models is found in the subsequent section.

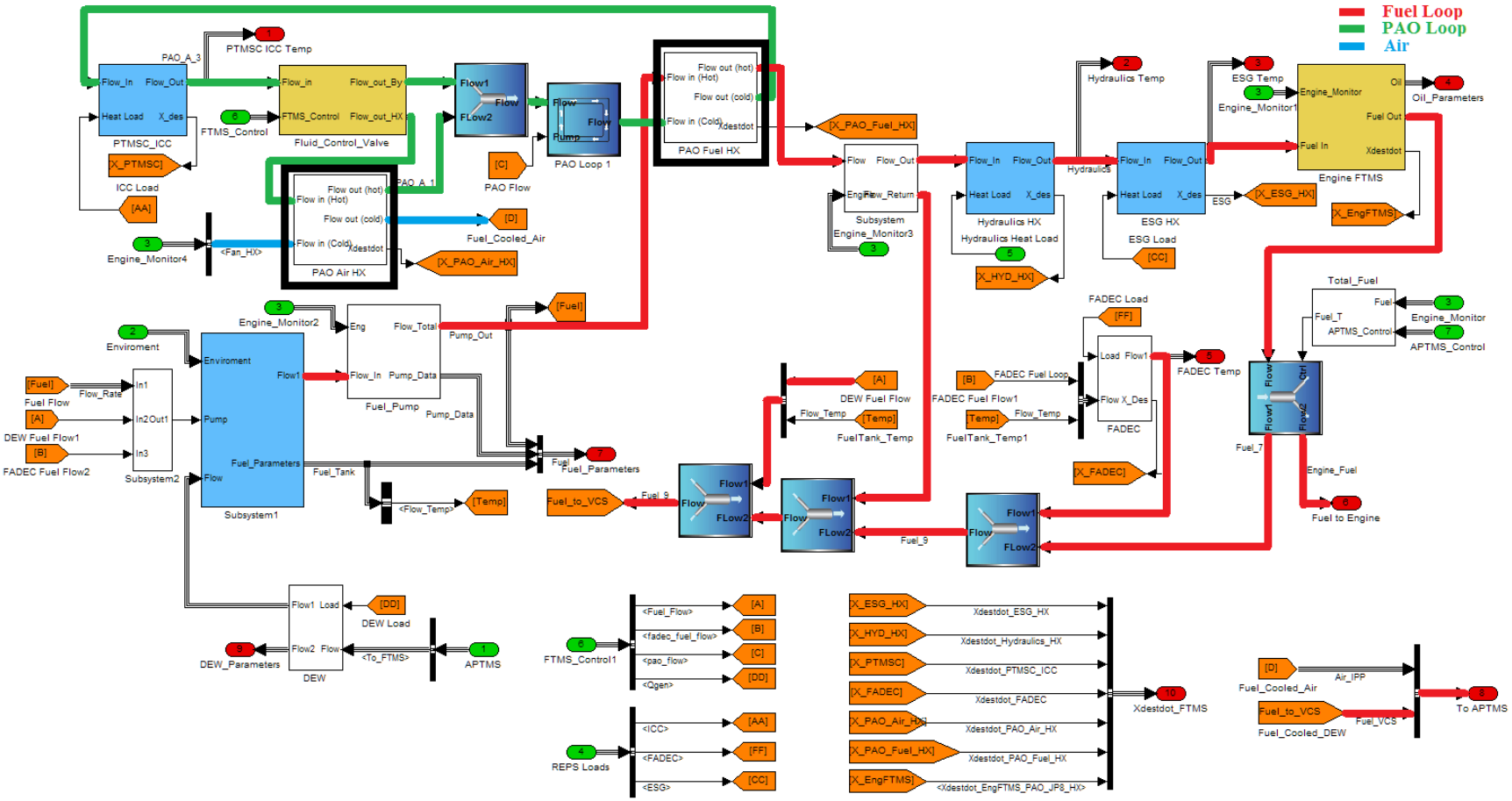

Figure 5.2. Generic INVENT tip-to-tail FTMS with heat exchanger models implemented.

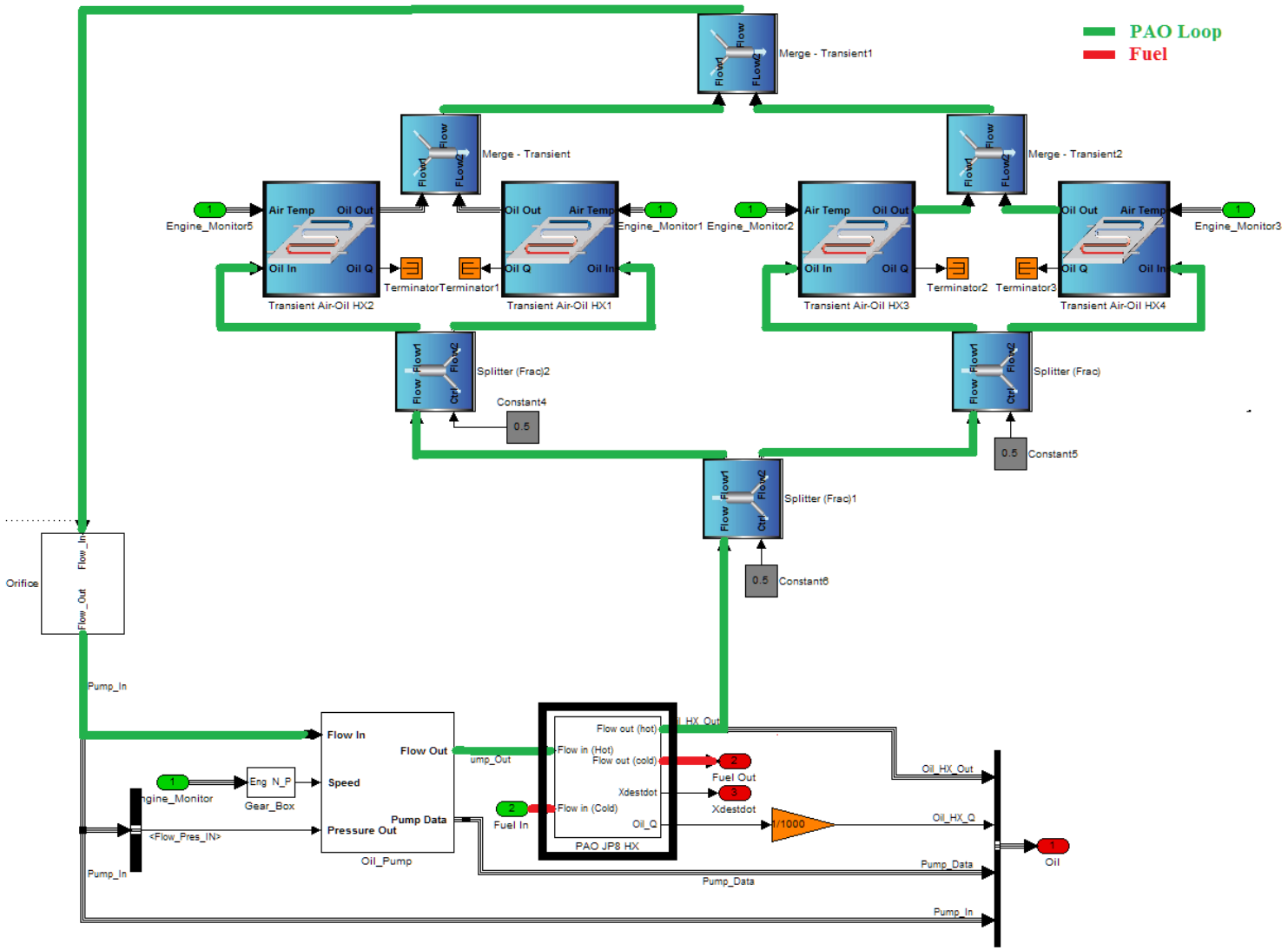

Figure 5.3. Generic INVENT tip-to-tail engine FTMS with heat exchanger model implemented.

5.1.3 Vehicle Performance Post/Prior to Heat Exchanger Model Integration

This section compares the generic INVENT tip-to-tail performance before and after integration of the heat exchanger model. The heat exchanger design values used are tabulated in Table 3.12 through Table 3.16 of Chapter 3. Heat exchanger sizing parameter values are those determined using the methodology described in Chapter 4 and are found in Table 4.1. The mission profile is shown in Figure 1.4 of Chapter 1.

5.1.3.1 Fuel Consumption Post/Prior to Heat Exchanger Integration

This section investigates the effect of integrating the new transient heat exchangers on fuel consumption by the generic INVENT tip-to-tail model. Within this tip-to-tail model, fuel is consumed in only two subsystems, the PS (engine) and the IPP within the APTMS. Fuel consumption of the tip-to-tail model, shown in Figure 5.4, differs greatly before and after integration into the tip-to-tail model. From Figure 5.4 it can be seen that integrating the new heat exchangers into this model has a negative impact on the total fuel consumed. The total fuel consumption over the mission prior to integration (described by the solid blue line) is clearly less that the total fuel consumption after heat exchanger model integration (described by the solid green line). In fact, as shown in Table 5.1, the tip-to-tail model with the new heat exchanger model consumes 11,867 kg as opposed to the original 11,036 kg, a difference of 907 kg or an 8.21% increase. This result is unexpected: Given the increased capability and lower mass of the tip-to-tail's new TMS, it would be expected that total fuel consumption would decline. That it does not is due to the fact that, as shown later, the original heat exchanger model permits certain temperatures of the tip-to-tail model to go unrealistically high at points of the mission, something the new model does not. An additional observation is that while the overall fuel consumption increased upon heat exchanger integration, IPP fuel consumption decreased by nearly 53%.

Table 5.1. Generic INVENT tip-to-tail model total fuel consumed.

	Total Fuel Consumption (kg)	**Engine Fuel Consumption (kg)**	**IPP Fuel Consumption (kg)**
Before Integration	11,036	10,753	283
After Integration	11,943	11,833	110

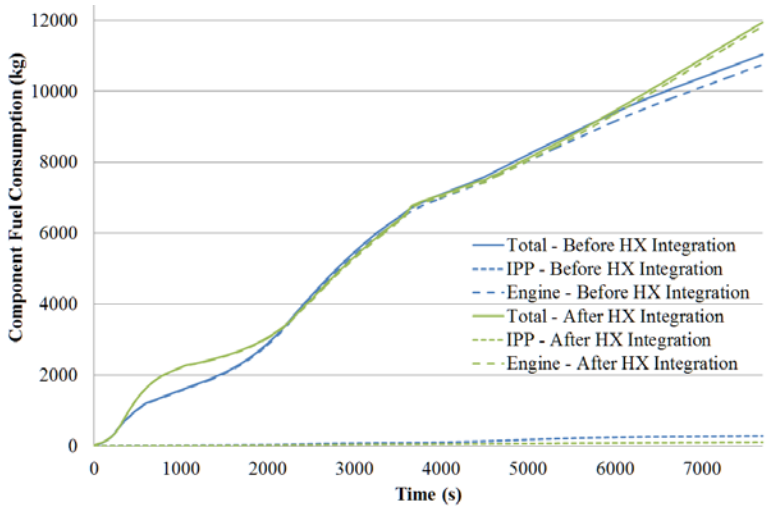

Figure 5.4. Fuel consumption over the entire 7700 s mission before and after integration of the new transient heat exchanger model.

The variation in the rate of fuel consumption in the PS and IPP is shown in Figure 5.5. Upon examination of Figure 5.5 it can be seen that three times during the simulation, (i.e., during mission segments 2-4, 8, and 10-12 as described in Table 1.1) the fuel consumption of the generic INVENT tip-to-tail model, which includes the new heat exchangers, greatly exceeds that of the old model. However, in all other segments, the fuel consumption rate is equal to or less than that of the old model. An explanation for this behavior is given in the following section.

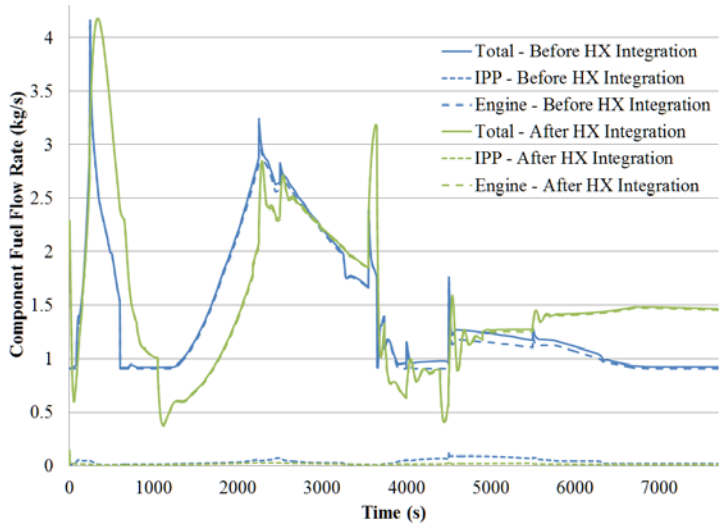

Figure 5.5. Fuel consumption rate over the entire 7700 s mission before and after integration of the new transient heat exchanger model.

5.1.3.2 IPP Performance Post/Prior to Heat Exchanger Integration

The primary component of the IPP is a turbine that combusts fuel with bleed air extracted from the engine to generate the power necessary to cool the APTMS subsystem. As such, the performance of the IPP is critical in the overall performance of the generic INVENT tip-to-tail. As demonstrated in Figure 5.6 and Figure 5.7, before the integration of the new heat exchanger models, the performance of the IPP was very poor for the second half of the mission. Figure 5.6 illustrates how the shaft speed of the IPP increases to its saturation limit [§§§] twice in the mission. An IPP shaft-speed limitation of 60,000 RPM is imposed to prevent excessive wear and premature failure of the IPP power turbine. Obviously, no such limit is exceeded with the newly integrated model since the actual shaft speed falls exactly on the set-point.

Figure 5.6. IPP shaft speed over the entire 7700 s mission before and after the integration of the new transient heat exchanger model.

[§§§] Within the Matlab® Simulink® programming environment, a saturation limit imposes an upper bound on certain model parameters. In the case of the IPP, the saturation limit imposes an upper bound on turbine shaft-speed, not allowing it to exceed 60,000 RPM.

The IPP turbine inlet temperature (TIT) variation throughout the mission is shown in Figure 5.7. Turbine efficiency increases with increased TIT. However, in order to prevent wear and premature blade failure, TITs typically range below 1500 K. Above these temperatures, even utilizing advanced materials and cooling techniques, turbine blades can experience creep and deformation that can cause excessive wear and in extreme cases, catastrophic failure. Thus, it is imperative that reasonable TITs are maintained in the IPP. Figure 5.7 demonstrates that during mission segments 9-12, the TIT vastly exceeds the allowable limit. Note that upon integration of the new heat exchanger model into the generic INVENT tip-to-tail, the TIT over the course of the entire mission is maintained at a reasonable limit. Clearly, this demonstrates that the TMS utilizing the new heat exchanger model is superior to that of the previous TMS. However, because the tip-to-tail TMS now has the capability to maintain reasonable temperatures throughout the entire mission, a price is paid in terms of fuel consumption.

Note that in Figure 5.4, at the beginning of mission segment 10 (4000 s), the amount of fuel consumed by the tip-to-tail using the new heat exchangers is nearly identical to the amount of fuel consumed by the previous model. However, due to the increased capacity of the TMS, after 4000 s the fuel consumption rate of the tip-to-tail model utilizing the new heat exchangers becomes noticeably larger than that of the old model. In summary, the TMS employing the new heat exchanger model allows the tip-to-tail to meet its performance goals, whereas the previous model did not and operated in infeasible ranges.

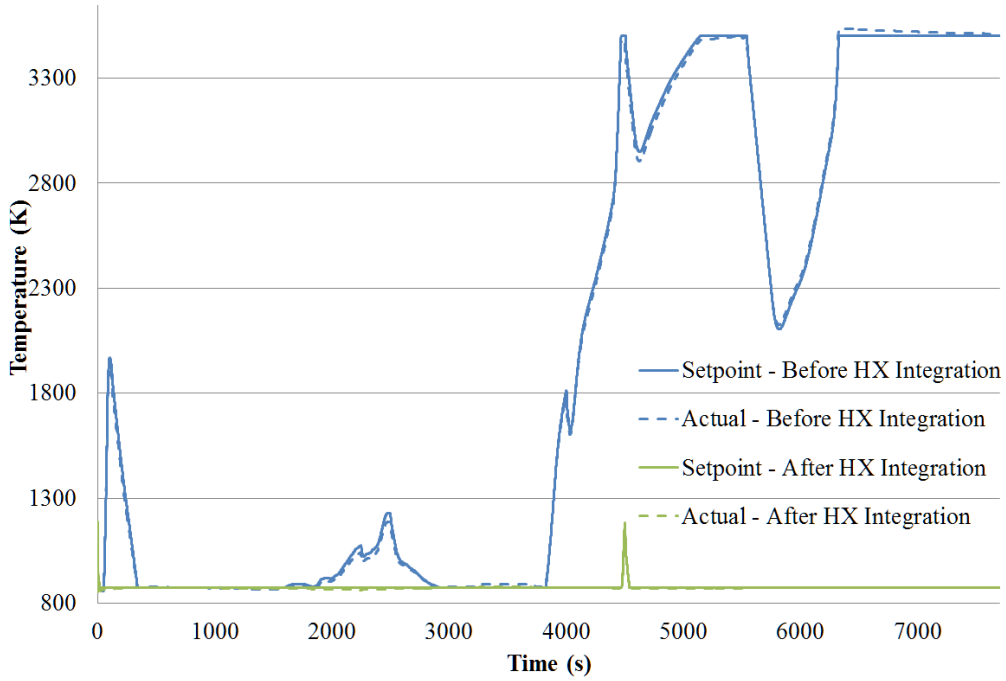

Figure 5.7. IPP turbine inlet temperature over the entire 7700 s mission before and after the integration of the new transient heat exchanger model.

5.1.3.3 APTMS Performance Post/Prior to Heat Exchanger Integration

The IPP described in the previous section produces power used to cool components in the APTMS, mainly the liquid cooled avionics (LCA), air cooled avionics (ACA), and the cockpit. This section describes the performance of the APTMS in terms of the temperatures of these three primary components.

The temperature of the LCA throughout the course of the entire 7700 s mission is shown below in Figure 5.8. The set-point temperature (defined by the blue line in the figure below), describes the desired temperature of the LCA throughout the mission. The figure shows that due to poor IPP performance the temperature of the LCA increases during mission segments 11 and 12 (between 5500 s and 7700 s). Notice that upon integration of the new heat exchanger model, the LCA temperature remains much closer than previously to the set-point throughout the mission.

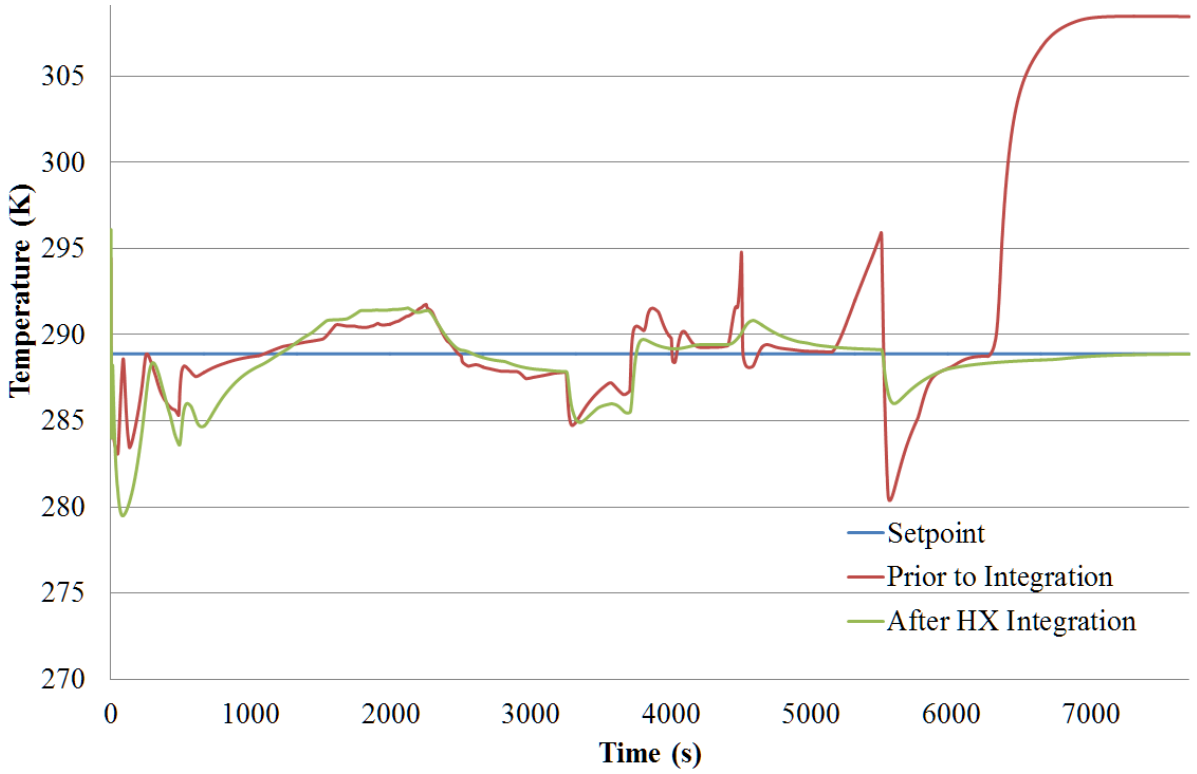

Figure 5.8. LCA temperature over the entire 7700 s mission before and after the integration of the new transient heat exchanger model.

The temperature of the ACA throughout the course of the entire 7700 s mission is shown below in Figure 5.9. Similar to the LCA, the ACA temperature also deviates from the set-point during the mission. However, in this case the tip-to-tail model with the new heat exchanger models performs only marginally better. The increase in temperature during mission segments 11 and 12 is mitigated and on average the temperature is closer to the set-point. However, during mission segment 6 (~2500 s), there is an increase in the magnitude of the temperature spike. Also note the overall poor matching of the set-point curve in both cases. This is likely due to the slow transient response of the system and an inability to react quickly enough to closely match the step change in the temperature set-point.

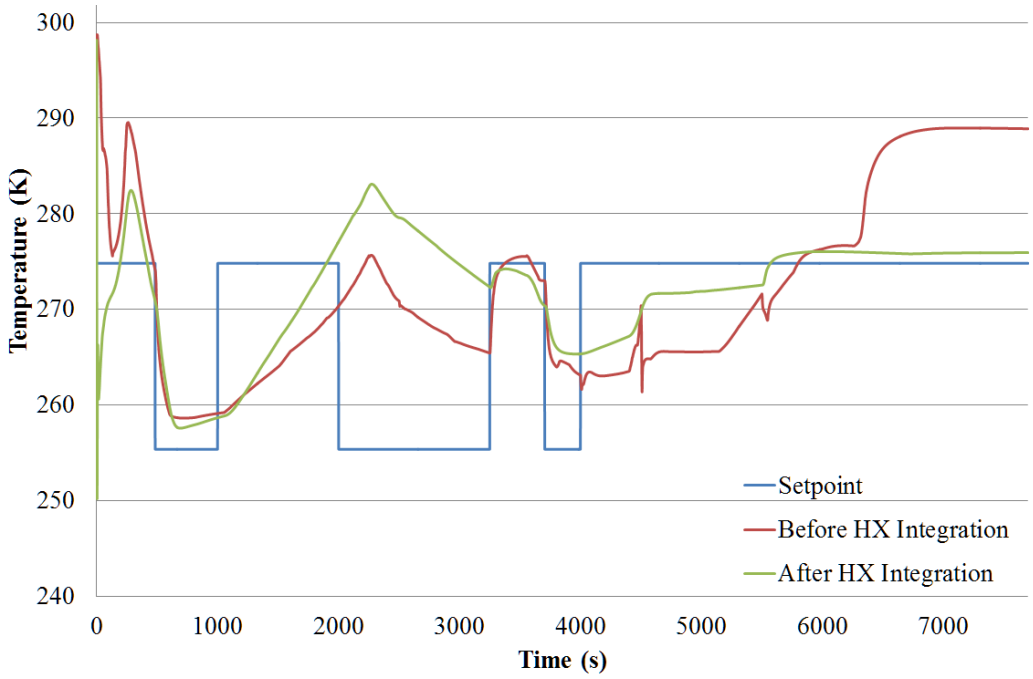

Figure 5.9. ACA temperature over the entire 7700 s mission before and after the integration of the new heat exchanger model.

The cockpit exit temperature over the course of the mission is shown in Figure 5.10. This temperature is important because it reflects the temperature experienced by the pilot. At high speeds, heat generated through friction and viscous effects is conducted through the cockpit enclosure and into the cockpit. These heat loads are proportional to airspeed and air density, and if not effectively mitigated, can cause the pilot to overheat. The figure below shows that during mission segment 3 (~500 s) and segments 11-12 (5500 s to 7700 s) the cockpit exit temperature increases dramatically utilizing the TMS with the previous heat exchanger model. A noticeable improvement is shown utilizing the new heat exchanger model. At no point in the mission, other than at the start of the simulation (due to poor initial conditions), does the cockpit exit temperature deviate from the set-point by more than ±2 K.

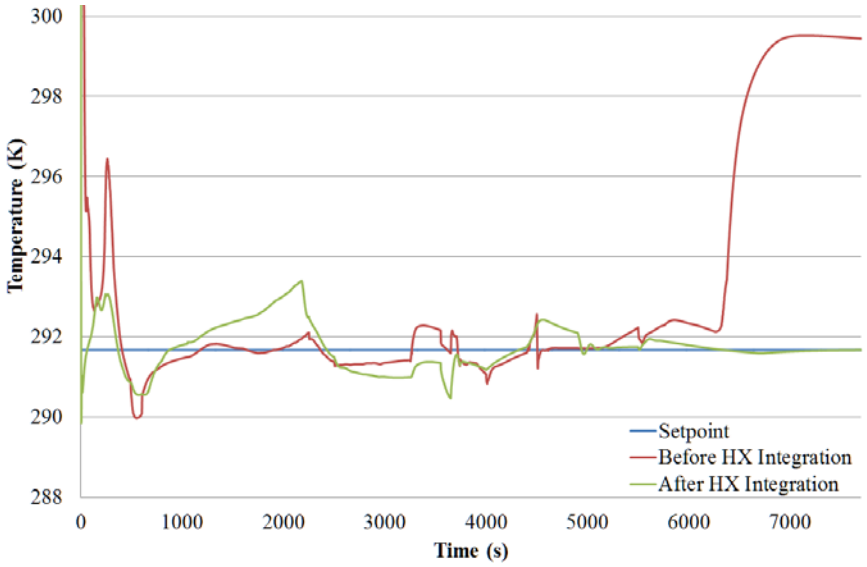

Figure 5.10. Cockpit exit temperature over the entire 7700 s mission before and after the integration of the new transient heat exchanger model.

5.1.3.4 Exergy Destruction Post/Prior to Heat Exchanger Integration

This section describes the exergy destruction associated with running the generic INVENT tip-to-tail model over the entire mission. Figure 5.11 shows the exergy destruction of the tip-to-tail over the course of the entire 7700 s mission for the model with and without the new transient heat exchangers. Similar to the figure describing fuel consumption, the exergy destruction for the tip-to-tail using the new heat exchanger models is greater than that of the previous model. Again, this is due to the fact that the new TMS allows the tip-to-tail to meet its performance requirements and that this increase in performance comes at the cost of increased total exergy destruction. Table 5.2 shows that prior to the integration, the total exergy destruction over the entire mission is 564 GJ, while after the integration the total exergy destruction it is 629 GJ, an increase of 11.5%.

Table 5.2. Generic INVENT tip-to-tail model exergy destruction.

	Total Exergy Destruction (GJ)
Before Integration	564
After Integration	629

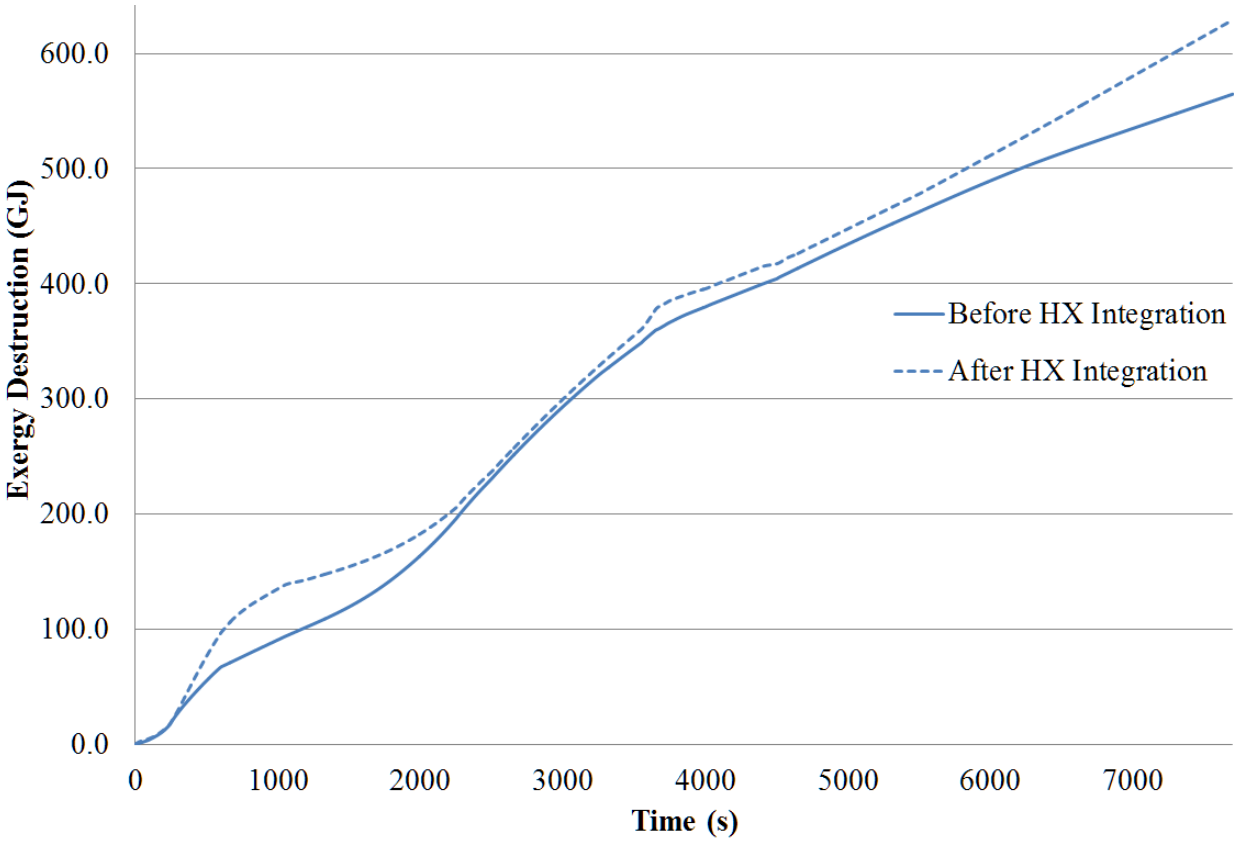

Figure 5.11. Exergy destroyed over the entire 7700 s mission before and after integration of the new transient heat exchanger model.

Figure 5.12 shows the variation in exergy destruction rate over the course of the entire mission for both the tip-to-tail model with and without the new transient heat exchangers integrated. From the figure it is clear that the exergy destruction rate for the new model is greater than that of the old model for a large part of the mission, especially during the initial climb and final cruise. Again, this occurs due to the fact that the new heat exchangers provide the tip-to-tail TMS with the capacity necessary to meet its performance goals.

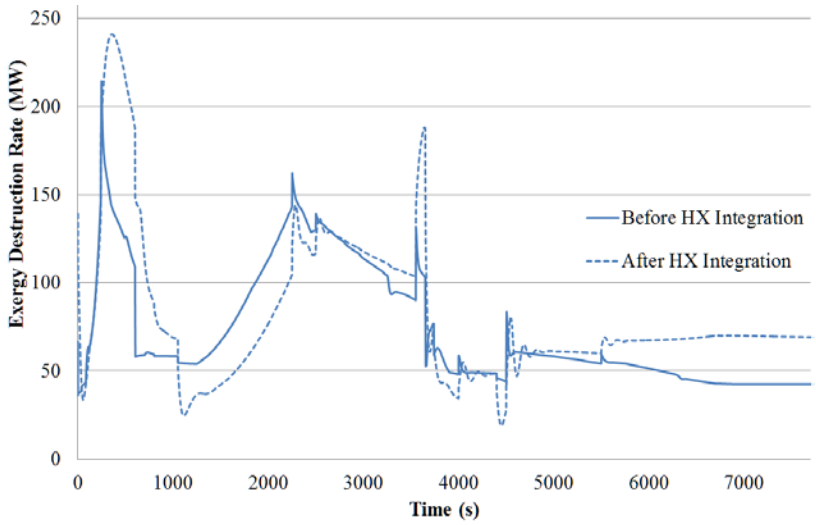

Figure 5.12. Exergy destruction rate over the entire 7700 s mission before and after the integration of the new transient heat exchanger model.

5.2 Large Scale Optimization of the Generic INVENT Tip-to-tail Model Using Fuel Consumption Minimization as an Objective

This section describes the formulation of the generic INVENT tip-to-tail, mission-integrated, synthesis/design optimization problem and shows results and analysis of the results obtained from solving the optimization problem with ModelCenter®'s Design Explorer® algorithm.

5.2.1 Formulation of the Optimization Problem

As described in Chapter 4, due to the fact that the heat exchanger parameters h, l, t_f, and t all converge to either their upper or lower bound in the individual heat exchanger optimizations, it is assumed that only s_1, s_2, and L need to be included in the optimization problem. The other parameters are fixed at their optimum values determined previously. Closer examination of the equations governing heat exchanger sizing shows the validity of this assumption.

The heat exchanger sizing algorithm uses a fixed fin efficiency set at 0.7. However, in a real heat exchanger, the fin efficiency diminishes with increased fin length. If this effect were modeled in the heat exchanger sizing algorithm, it would be expected that the fin height, h, would not always converge to the maximum.

The fin strip length, l, converges to the upper bound in the heat exchanger optimization problem. An analysis of the equations found in Chapter 3 show that as l increases, the friction factor, f, and hydraulic diameter, d_h, both increase. This has a near neutral effect on pressure drop and, as can be seen through examination of Table 3.10, has a positive effect on heat transfer performance.

The fin thickness, t_f, and plate thickness, t, both add resistance to the transfer of heat between the two fluids. Additionally, larger magnitudes of t_f and t correlate to increases in heat exchanger mass. Thus, it is expected and shown in Chapter 4 that the values for t_f and t converge to the lower bound.

For these reasons it can be said with certainty that for purposes of the mission-integrated synthesis/design optimization problem, the only important parameters are s_1, s_2, and L. As such, this optimization problem is formulated without the inclusion of the other heat exchanger sizing parameters. The formulation of two optimization problems, i.e., minimization of fuel consumption and minimization of exergy destruction, using these 18 synthesis/design decision variables (3 from each of the 6 heat exchangers) and no operational decision variables is described in Chapter 4. No operational decision variables are used in this optimization problem due to the fact that the tip-to-tail model is transient. Any tip-to-tail parameters that would be specified as operational decision variables in the optimization of a steady state tip-to-tail model are controlled by the tip-to-tail subsystem controllers.

5.2.2 Results and Analysis

Implementation of the optimization problem in ModelCenter® and allowing the Design Explorer® algorithm to converge to the global optimum yields the results shown in Table 5.3. It should be noted that the computation burden associated with performing this optimization is substantial. The Design Explorer® algorithm required 863 objective function evaluations (i.e., tip-to-tail simulations) to reach the global optimum, a task that the algorithm completed in 12 days. This equates to an average simulation time of 19 min. As mentioned previously, the normal simulation time for the tip-to-tail model is 4.5 min. However, poor heat exchanger designs can cause the tip-to-tail performance to suffer, creating an undesirable situation where the strain placed on the IPP can cause the compressor to surge, which in turn can cause surge in the PS

compressor. Under these conditions, Matlab® Simulink's® ode23s solver can have difficulty converging to a solution, significantly increasing the run time associated with the simulation.

Table 5.3. Optimum set of heat exchanger synthesis/design parameter values determined from the mission-integrated synthesis design optimization of the tip-to-tail (shown in red) compared to the parameter values determined from the individual optimization of each heat exchanger, as performed in Chapter 4 (no shading).

		s_1	s_2	L	W
		mm	***mm***	***m***	***kg***
APTMS Heat Exchangers	**PAO-Air HX**	0.83	0.83	0.08598	3.05
		0.83	**0.83**	**0.05000**	**51.63**
	Cond Air-Air HX	0.88739	0.84452	0.09090	2.66
		0.83	**0.84452**	**0.08537**	**3.23**
	Air-Air HX	0.83	0.862070	0.08336	2.29
		0.83	**0.862070**	**0.05000**	**3.95**
FTMS Heat Exchangers	**PAO-Fuel HX**	0.83	0.98637	2.07879	93.68
		0.83	**0.98637**	**1.05361**	**207.91**
	PAO-Air HX	0.83	0.83	0.09080	273.92
		0.83	**0.83**	**0.05000**	**455.38**
	EFTMS / PAO-Fuel HX	0.83	0.83	0.56284	14.59
		0.83	**0.83**	**0.41200**	**17.47**

Table 5.3 describes the optimal set of heat exchanger synthesis/design parameter values. From the table it can be seen that for each heat exchanger, the value of s_1 converges to the lower bound. Additionally, the length of each heat exchanger determined from the mission-integrated synthesis/design optimization is less than the length determined from the individual optimization of each heat exchanger as performed in Chapter 4. One final observation is that in each case the weight of each heat exchanger increased from the previous values determined in Chapter 4.

In Chapter 4, the heat exchangers are individually optimized for minimum mass. In the tip-to-tail mission-integrated synthesis/design optimization, the tip-to-tail model is optimized for minimum fuel consumption. As has been shown previously elsewhere, minimum fuel usage is proportional to minimum exergy destruction (based on the total-vehicle exergy balance given in Chapter 3). Now, the exergy destruction in a heat exchanger is due to heat transfer through the heat exchanger material and frictional losses accounted for in the pressure drop. Thus, while a

heat exchanger optimized for minimum weight has a longer length and a smaller cross-sectional area, A_c (corresponding to a higher pressure drop) according to equation (5.1) below, a heat exchanger optimized for minimum exergy destruction is shorter and has a higher cross sectional area (corresponding to a lower pressure drop)., i.e.,

$$\Delta P = \frac{1}{2}\rho f\left(\frac{\dot{m}}{A_c}\right)^2 \frac{4L}{D_h} \tag{5.1}$$

Where P is the pressure, ρ the density, f the friction factor, $\dot{m}$ the mass flow rate, A_c the fluid flow cross-sectional area, L the overall heat exchanger length, and D_h the hydraulic diameter.

5.2.2.1 Fuel Consumption Post/Prior to Mission-Integrated Synthesis/Design Optimization

This section investigates the effect of using the heat exchanger parameter values obtained through mission-integrated synthesis/design optimization on fuel consumption of the INVENT tip-to-tail model. As described in 5.1.3.1, within the generic INVENT tip-to-tail model, fuel is consumed in only two subsystems, the PS (engine) and the IPP within the APTMS. Fuel consumption of the tip-to-tail model, shown in Figure 5.13, differs before and after the mission-integrated synthesis/design optimization. From this figure it can be seen that utilizing the values obtained from the optimization have a positive impact on fuel consumption of the tip-to-tail, an expected result given that the optimization's objective is to minimize fuel consumption. While the fuel consumption of the optimized tip-to-tail model (described by the solid red line) is still greater than the original model (i.e., prior to heat exchanger integration, described by the solid blue line), as shown in the following sections, the optimized tip-to-tail, unlike the original tip-to-tail, meets all performance requirements.

Table 5.4 shows that the tip-to-tail model optimized using mission-integrated optimization uses 619 kg less than the tip-to-tail using heat exchanger sizing parameters obtained from the individual heat exchanger optimizations. This difference corresponds to an improvement of 5.2%. With respect to the original tip-to-tail, there is only a 288 kg or 2.6% increase. An additional observation is that in addition to the decrease in overall fuel consumption, the fuel

consumed in the IPP decreased by approximately 35.5% and 74.9%, respectively, over the new model prior to optimization and the original model.

The variation in the rate of fuel consumption in the PS and IPP for each of the three cases is shown in Figure 5.14. Upon examination of this figure, it can be seen that the fuel consumption rate of the optimized tip-to-tail, while following the same usage trends, is lower than or equal to the fuel consumption rate of the tip-to-tail model using heat exchanger parameter values obtained from the individual heat exchanger optimizations.

Table 5.4. Generic INVENT tip-to-tail model total fuel consumed.

	Total Fuel Consumption (kg)	Engine Fuel Consumption (kg)	IPP Fuel Consumption (kg)	Total Difference (kg)	% Difference
Before Integration	11036	10753	283	-	-
After Integration	11943	11833	110	+907	+8.2%
After Optimization	11324	11260	71	+288/-619****	+2.6%/-5.2%

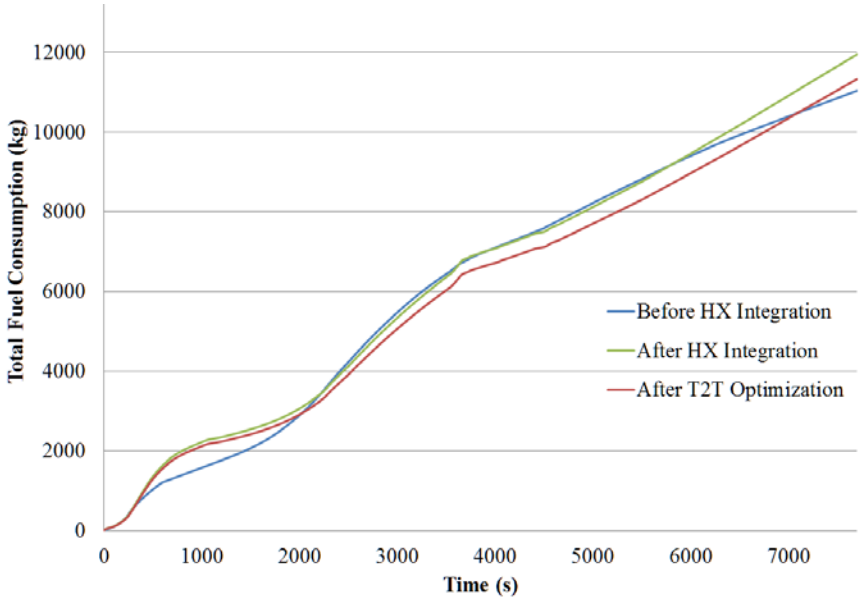

Figure 5.13. Fuel consumption over the entire 7700 s mission before and after mission-integrated synthesis/design optimization of the generic INVENT tip-to-tail model.

**** The first number compares to the first row. The second number compares to the second row.

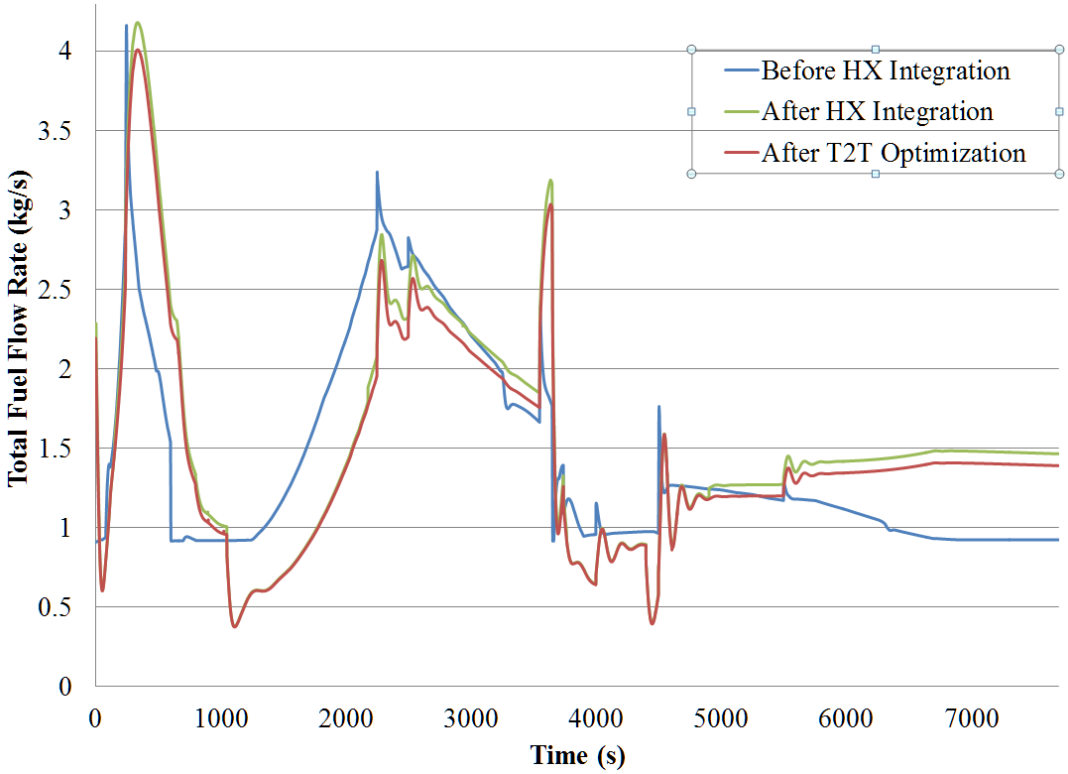

Figure 5.14. Fuel consumption rate over the entire 7700 s mission before and after mission-integrated synthesis/design optimization of the generic INVENT tip-to-tail model.

5.2.2.2 IPP Performance Post/Prior to Mission-Integrated Synthesis/Design Optimization

IPP performance is critical to the overall performance of the generic INVENT tip-to-tail model. As shown in the previous section, the original tip-to-tail model (without the new transient heat exchanger models integrated) performed very poorly. In fact, during several portions of the mission, the IPP TIT greatly exceeded the maximum TIT and the IPP shaft speed hit the saturation limit. Upon integration of the new heat exchanger models, the maximum IPP TIT experienced decreased dramatically. In fact, at only one point in the mission does the TIT go above 1000 K. Using the set of heat exchanger synthesis/design parameter values determined from the mission-integrated optimization increases the performance of the IPP even further. As demonstrated in Figure 5.16, the IPP TIT never goes above 870 K. Figure 5.15 shows the

variation in IPP shaft speed for all three cases. It can be seen from the figure that using the heat exchanger synthesis/design parameter values obtained from the mission-integrated optimization had little impact on the profile of the IPP shaft speed, as it closely follows the profile of the model using heat exchanger synthesis/design parameter values obtained from the individual heat exchanger optimizations.

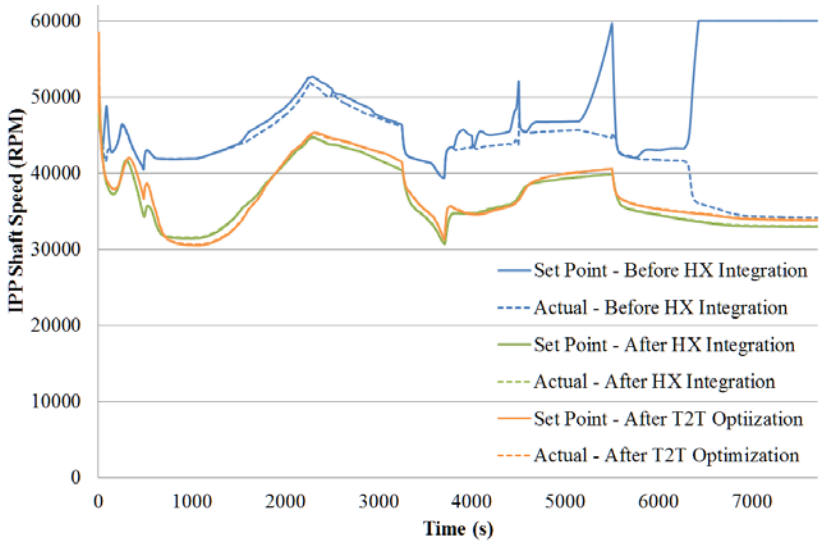

Figure 5.15. IPP shaft speed over the entire 7700 s mission before and after mission-integrated synthesis/design optimization of the generic INVENT tip-to-tail model.

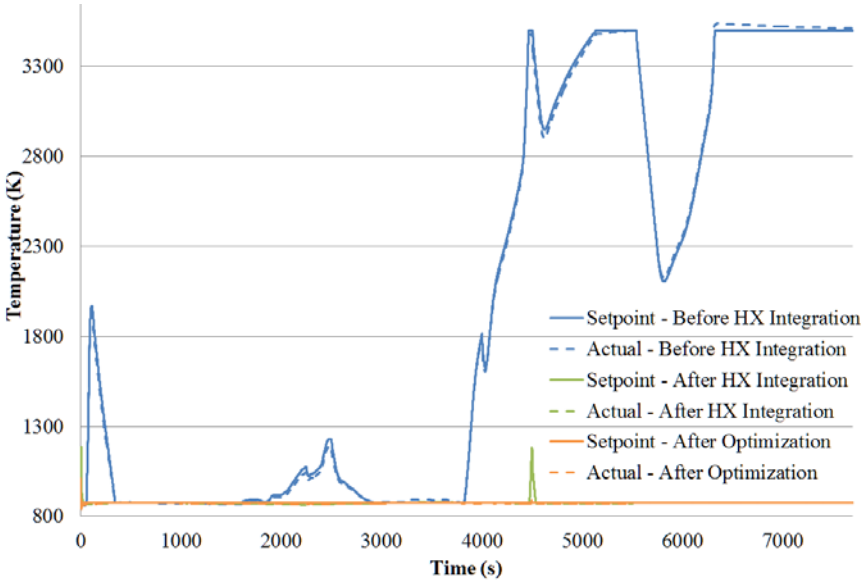

Figure 5.16. IPP TIT over the entire 7700 s mission before and after mission-integrated synthesis/design optimization of the generic INVENT tip-to-tail.

5.2.2.3 APTMS Performance Post/Prior to Mission-Integrated Synthesis/Design Optimization

The IPP described in the previous section produces power used to cool components in the APTMS, mainly the LCA, ACA, and the cockpit. This section describes the changes in performance of the APTMS due to the mission-integrated synthesis/design optimization in terms of the temperatures of these three primary components.

Figure 5.17 shows the temperature of the LCA throughout the course of the entire 7700 s mission for the tip-to-tail model. The primary measure of APTMS performance relative to the LCA is the magnitude of the deviation from the set-point temperature. As shown in the figure, the original tip-to-tail model with the old heat exchanger models has very poor performance. Integrating the new heat exchanger models into the tip-to-tail incurs major improvements in adherence to the set-point temperature. It can be seen from the figure that using heat exchanger synthesis/design parameter values obtained from the mission-integrated optimization result in only marginal performance gains. At nearly every time step in the mission, the optimized vehicle has LCA temperatures that are closer to the set-point. Additionally, the maximum deviation from the set-point is reduced, although only marginally so.

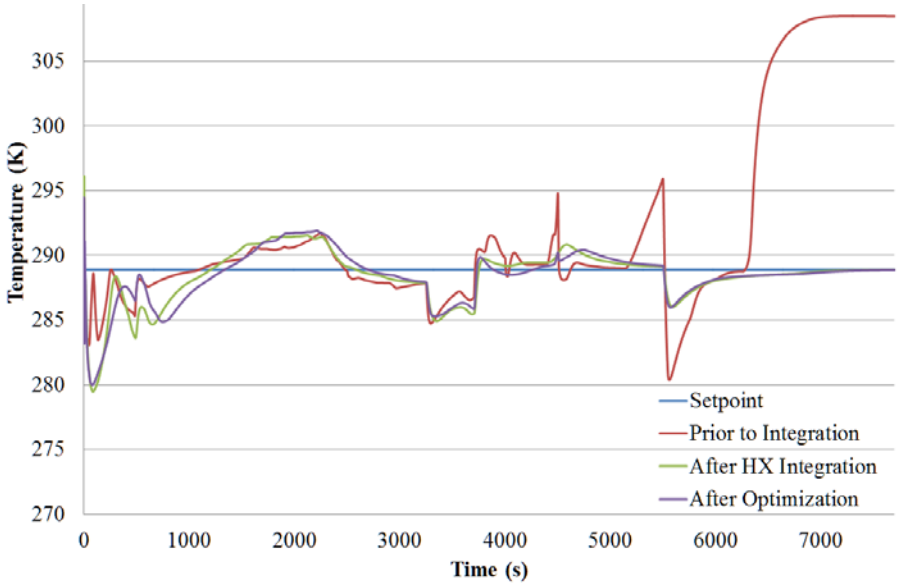

Figure 5.17. LCA temperature over the entire 7700 s mission before and after mission-integrated synthesis/design optimization of the generic INVENT tip-to-tail.

Figure 5.18 shows the temperature of the ACA throughout the course of the entire 7700 s mission for the tip-to-tail model. The primary measure of APTMS performance relative to the ACA is the magnitude of the deviation from the set-point temperature. As shown in the figure, the initial tip-to-tail model with the old heat exchanger models has very poor performance, experiencing large deviations from the set-point, especially during the last two segments of the mission. Integrating the new heat exchanger models into the tip-to-tail incurs improvements in adherence to the set-point temperature, especially in mission segments 10-12. However, due to the step change in the set-point , if there is any improvement in terms of performance it is only marginal.

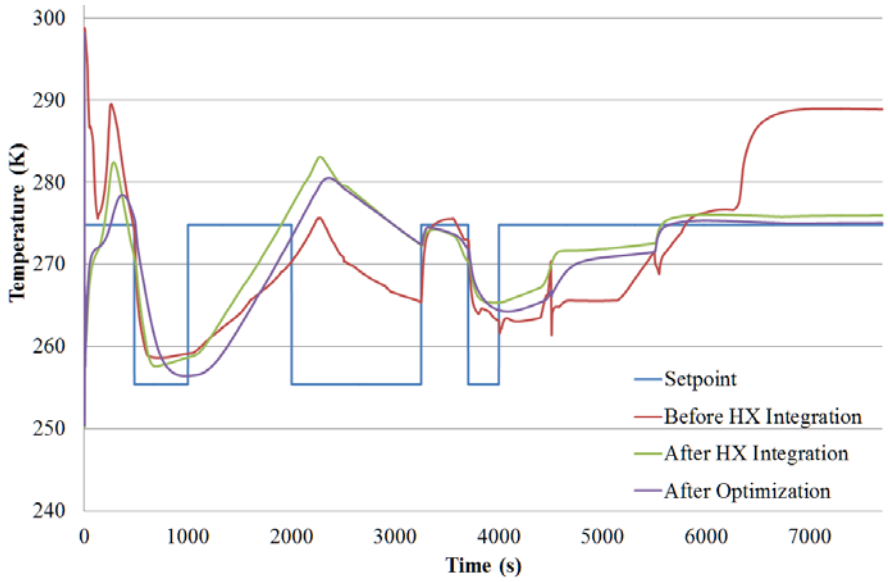

Figure 5.18. ACA temperature over the entire 7700 s mission before and after mission-integrated synthesis/design optimization of the generic INVENT tip-to-tail.

The cockpit exit temperature over the course of the mission for each of the three cases is shown in Figure 5.19 below. As mentioned previously, the cockpit exit temperature of tip-to-tail model without the new transient heat exchanger models deviates from the set-point considerably during mission segments 10-12. After integration, this deviation from the set-point is significantly reduced. Using the heat exchanger synthesis/design variables obtained through mission-integrated synthesis design optimization improves the adherence to the set-point even further. As shown in the figure below, at nearly every point in the 7700 s mission, the exit

temperature of the air in the cockpit stays within ±1 K of the set-point. This is a marked improvement over the tip-to-tail that uses heat exchanger synthesis/design parameter values obtained from the individually optimization each heat exchangers.

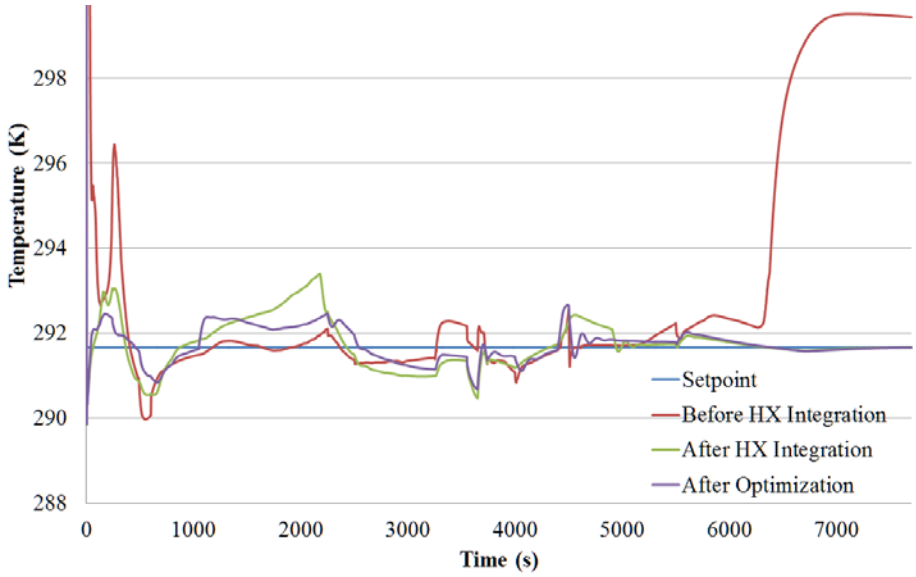

Figure 5.19. Cockpit exit temperature over the entire 7700 s mission before and after mission-integrated synthesis/design optimization of the generic INVENT tip-to-tail model.

5.2.2.4 Exergy Destruction Post/Prior to Mission-Integrated Synthesis/Design Optimization

This section describes the exergy destruction associated with running the tip-to-tail over the entire 7700 s mission for all three cases. Figure 5.20 shows the exergy destruction for the original model, the model using heat exchanger synthesis/design parameter values obtained through the individual heat exchanger optimizations, and the model using heat exchanger synthesis/design parameter values obtained by performing mission-integrated synthesis/design optimization. Table 5.5 shows the total exergy destruction associated with each case. The original model destroys 564 GJ of exergy. After integration of the individually optimized heat exchanger models, the tip-to-tail model destroys 629 GJ of exergy, an increase in exergy destruction of 65 GJ or 11.5%. After the mission-integrated optimization, the tip-to-tail destroys

598 GJ of exergy, an increase of 6.0% over the original tip-to-tail and a decrease of 4.9% over the model with the individually optimized heat exchangers.

Table 5.5. INVENT tip-to-tail model exergy destruction after performing mission-integrated synthesis/design optimization.

	Total Exergy Destruction (GJ)	Difference in Exergy Destruction (kg)	Relative Change
Before Integration	564		
After Integration	629	+65	+11.5%
After Optimization	598	+34/-31[††††]	+6.0%-4.9%

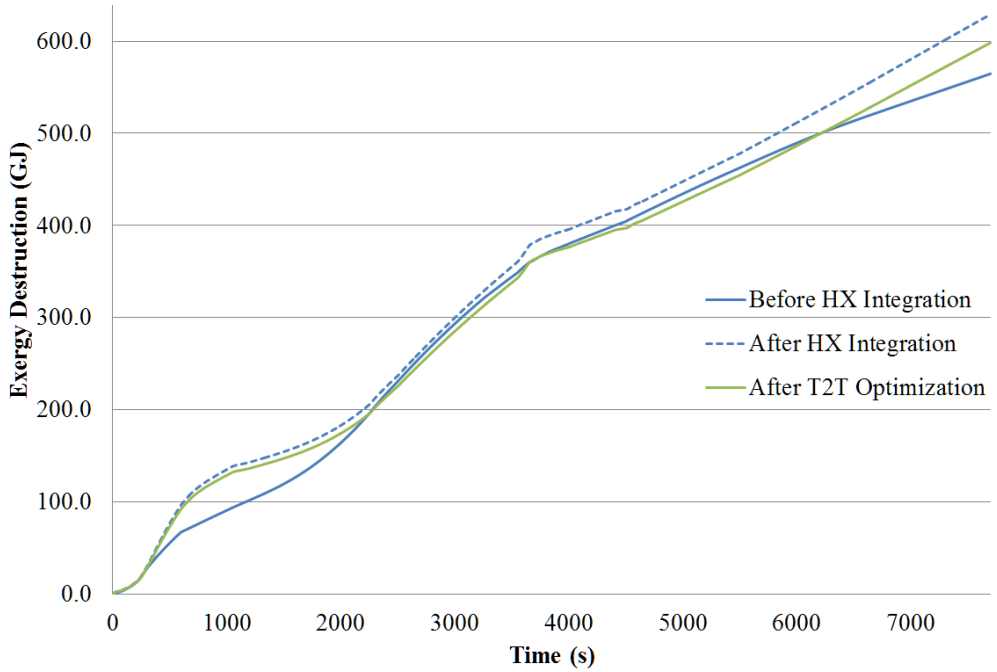

Figure 5.20. Exergy destroyed over the entire 7700s mission before and after mission-integrated synthesis/design optimization of the INVENT tip-to-tail model.

Figure 5.21 shows the variation in exergy destruction rate over the course of the entire mission for the original model, the model using heat exchanger synthesis/design parameter values obtained through the individual heat exchanger optimizations, and the model using heat exchanger synthesis/design parameter values obtained by performing mission-integrated synthesis/design optimization. From the figure, it is clear that the exergy destruction rate for the

[††††] The first number compares to the first row. The second number compares to the second row.

vehicle optimized using mission-integrated synthesis/design optimization performs very similarly to the vehicle using the individually optimized heat exchangers. However, at every point in the mission, the former has a smaller exergy destruction rate.

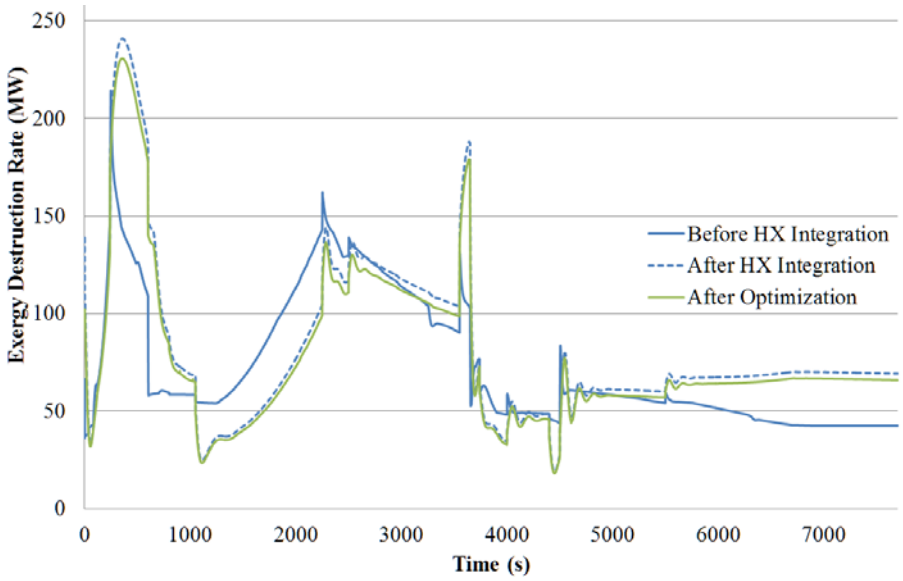

Figure 5.21. Exergy destruction rate over the entire 7700 s mission before and after mission-integrated synthesis/design optimization of the generic INVENT tip-to-tail model.

5.2.2.5 INVENT Tip-to-Tail Subsystem Exergy Analysis

Figure 5.22 describes the exergy destruction of the total vehicle, AVS, and PS before and after performing mission-integrated synthesis/design optimization on the generic INVENT tip-to-tail model. Additionally, the exergy destruction associated with the wake of the vehicle as well as the exergy destruction associated with any subsystems that do not have exergy balances implemented is shown in the figure (represented by the orange line). As described in Chapter 3, the exergy destruction associated with the wake/unmodeled subsystems is calculated as the difference between the total vehicle exergy destruction and the summation of the exergy destruction associated with each subsystem (i.e., the AVS, PS, APTMS, and FTMS).

Table 5.6 describes the exergy destruction associated with each subsystem within the generic INVENT tip-to-tail model. It can be seen from the table that the exergy destruction associated with each tip-to-tail subsystem decreased upon performing mission-integrated

synthesis design optimization. The most notable improvement, although not as large (in absolute magnitude) as the other improvements, is the change in APTMS performance. The exergy destruction associated with the APTMS decreased by 82.5%, although the magnitude of the change was relatively small. Additionally, notice that the exergy destruction associated with the AVS subsystem does not change. This occurs due to the fact that the exergy destruction due to the AVS is associated with the drag coefficient, ambient temperature, and vehicle velocity (as described by the equations in Table 3.2 of Chapter 3). These parameters are determined by the vehicle's altitude and Mach number (i.e., the mission profile) and, thus, do not change regardless of performance of the vehicle subsystems.

Table 5.6. Exergy destruction associated with each INVENT tip-to-tail subsystems before and after mission-integrated synthesis/design optimization of the INVENT tip-to-tail model.

	Exergy Destruction (GJ)			
	After Integration	**After Optimization**	**Difference**	**Relative Change**
Total	629	598	-31	-4.9%
PS	193	178	-15	-7.8%
AVS	48.7	48.7	~	~
FTMS	0.0754	0 .0744	-0.001	-1.3%
APTMS	0.715	0.125	-0.59	-82.5%
Wake/Unmodeled Subsystems	386	371	-15	3.9%

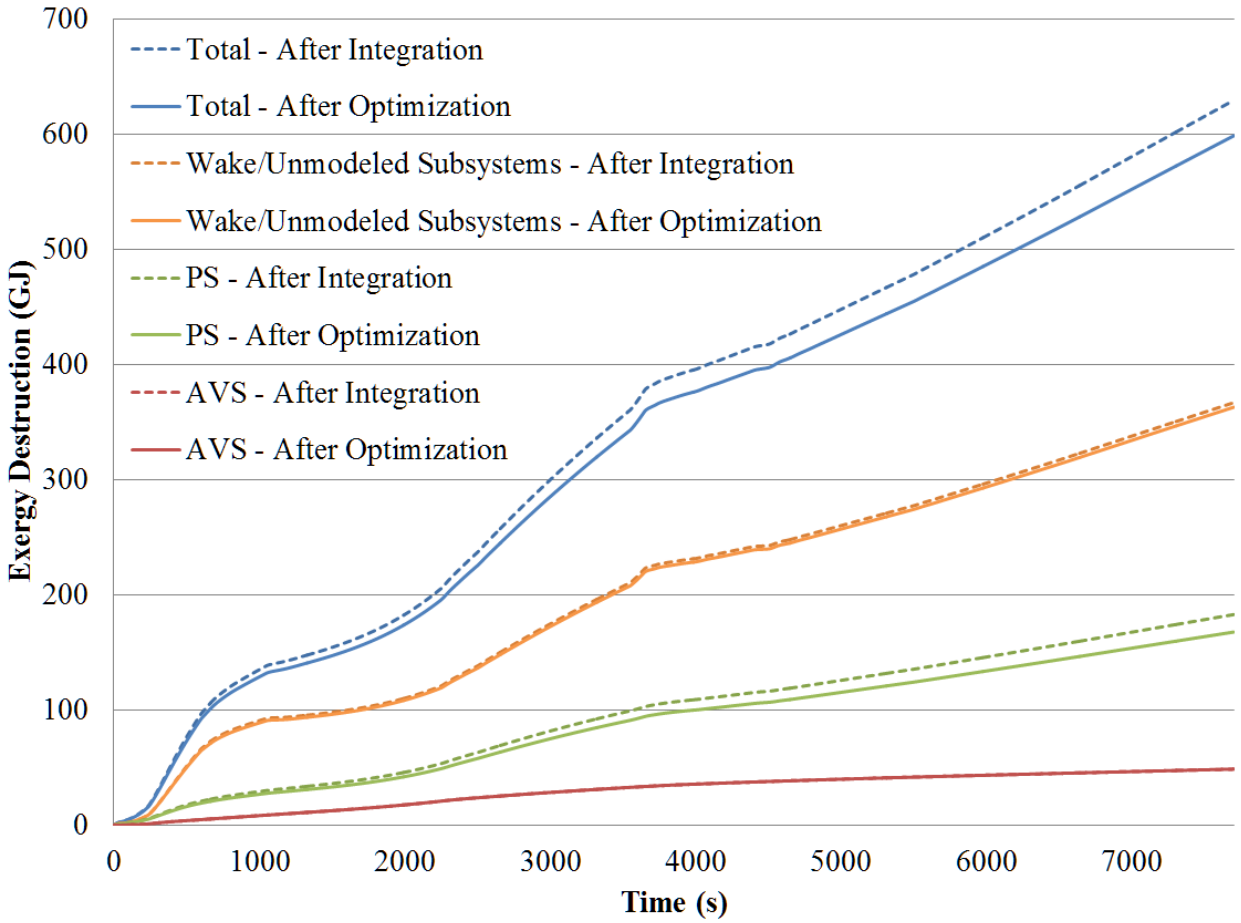

Figure 5.22. Exergy destruction of the most significant generic INVENT tip-to-tail subsystems before and after mission-integrated synthesis/design optimization.

Figure 5.23 describes the exergy destruction associated with the APTMS and FTMS subsystems of the generic INVENT tip-to-tail model. As can be seen from the figure, although the FTMS exergy destruction does not improve by a significant margin due to the mission-integrated optimization, the performance of the APTMS improves greatly.

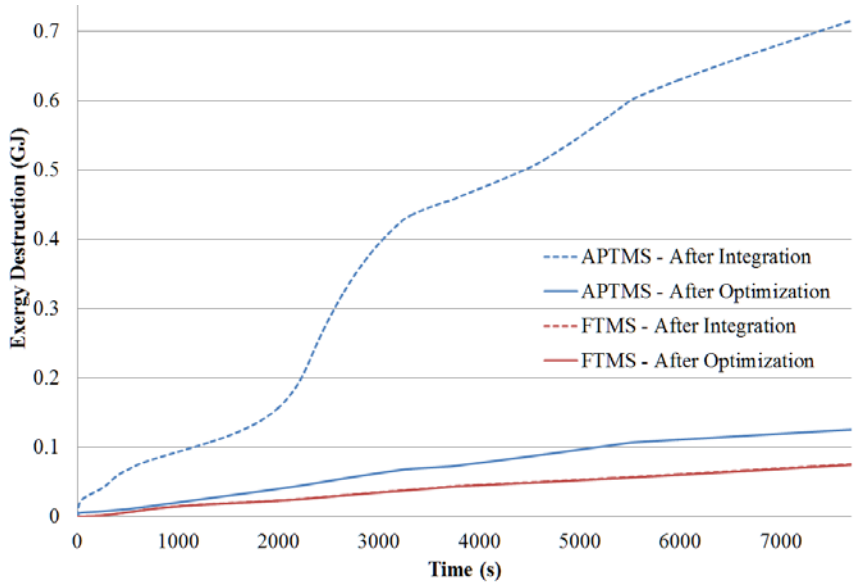

Figure 5.23. Exergy destruction of the APTMS and FTMS subsystems before and after mission-integrated synthesis/design optimization of the generic INVENT tip-to-tail model.

5.3 Comparison of Fuel Consumption Minimization and Exergy Destruction Minimization Objectives

This section describes the formulation of the generic INVENT tip-to-tail, mission-integrated, synthesis/design optimization problem to minimize exergy destruction and shows results and an analysis of the results obtained from solving the optimization problem with ModelCenter®'s Design Explorer® algorithm. The formulation of the two optimization problems, i.e., minimization of fuel consumption and minimization of exergy destruction, using 18 synthesis/design decision variables (3 from each of the 6 heat exchangers) and no operational decision variables is described in Chapter 4.

5.3.1 Results and Analysis

As noted in Section 5.2, the computational burden associated with performing this optimization is substantial. It is desirable, therefore, to minimize the number of objective function evaluations required to converge to the global optimum and to constrain the synthesis/design decision variables in such a way that the instability of the tip-to-tail model exhibited in Section 5.2 is not encountered. Based on equation (2.3) of Chapter 2, it can be

shown that when the vehicle is optimized for minimum fuel consumption it is simultaneously optimized for minimum exergy destruction. Thus, it is a valid assumption to say that the optimal synthesis/design decision variable values obtained by minimizing fuel consumption will be the same or very similar to those obtained by minimizing exergy destruction, at least as long as there are no AVS DOF (see Chapter 2, Section 2.1.3), which is the case here. Making this assumption allows for the imposition of tighter constraints on each synthesis/design decision variable used in the exergy destruction minimization optimization problem, which corresponds to fewer required objective function evaluations and increased tip-to-tail model stability. A comparison of the synthesis/design decision variable constraints used in the fuel minimization problem with those used in the exergy destruction minimization problem is shown in Table 5.7.

Table 5.7. Heat exchanger design/operational decision variable constraints.

	Design Decision Variable Constraints			**Operational Constraints**	
Fuel Consumption Minimization Constraints	$0.83 \leq s_1 \leq 2.08$ (mm)	$0.83 \leq s_2 \leq 2.08$ (mm)	$0.05 \leq L \leq 2.5$ (m)	$1 \leq \Delta P_1 \leq 30$ (kPa)	$1 \leq \Delta P_2 \leq 30$ (kPa)
Exergy Destruction Minimization Constraints	$0.83 \leq s_1 \leq 1.0$ (mm)	$0.83 \leq s_2 \leq 1.0$ (mm)	$0.05 \leq L \leq 1.5$ (m)	$1 \leq \Delta P_1 \leq 30$ (kPa)	$1 \leq \Delta P_2 \leq 30$ (kPa)

Implementation of the optimization problem in ModelCenter® and allowing the Design Explorer® algorithm to converge to the global optimum yields the results shown in Table 5.8. The Design Explorer® algorithm required 422 objective function evaluations (i.e., tip-to-tail simulations) to reach the global optimum, a task that the algorithm completed in 3 days. This equates to an average simulation time of 10.2 min. As mentioned previously, the normal simulation time for the tip-to-tail model is 4.5 min. This is a marked improvement in both the number of objective function evaluations (441 fewer evaluations) and the average simulation time (a decrease of 8.8 minutes per simulation), which were required by the fuel minimization problem.

Table 5.8. Optimal set of heat exchanger synthesis/design decision variable values determined from using fuel minimization as an objective (shown in red) compared to the optimal values obtained from using exergy destruction minimization as an objective (shown in green).

		s_1	s_2	L	W
		mm	*mm*	*m*	*kg*
APTMS Heat Exchangers	**PAO-Air HX**	0.83	0.83	0.05000	51.63
		0.83	0.83	0.05000	51.63
	Cond Air-Air HX	0.88739	0.84452	0.08534	3.26
		0.83	0.84452	0.08537	3.23
	Air-Air HX	0.83	0.862070	0.05000	3.95
		0.83	0.862070	0.05000	3.95
FTMS Heat Exchangers	**PAO-Fuel HX**	0.83	0.98637	1.05360	207.97
		0.83	0.98637	1.05361	207.91
	PAO-Air HX	0.83	0.83	0.05000	455.38
		0.83	0.83	0.05000	455.38
	EFTMS / PAO-Fuel HX	0.83	0.83	0.41200	17.47
		0.83	0.83	0.41200	17.47

Table 5.9 shows a comparison of the total exergy destruction determined from the fuel consumption minimization problem with that determined from the exergy destruction minimization problem. As can be seen from the table, the exergy destruction is nearly identical for both methods. In fact, the relative difference between the exergy destruction obtained from minimizing exergy destruction and from minimizing fuel consumption is less that 0.02% This result validates the previous assumption that when a vehicle is optimized for minimum fuel consumption, it is simultaneously optimized for minimum exergy destruction provided, of course, that there are as was noted earlier no AVS DOF.

Table 5.9. Comparison of the generic INVENT tip-to-tail model exergy destruction determined from the fuel consumption minimization and the exergy destruction minimization problems.

	Total Exergy Destruction (GJ)
Fuel Consumption Minimization	598
Exergy Destruction Minimization	597.9

Chapter 6 - Conclusions and Recommendations

The results obtained from this thesis work led to a number of conclusions and recommendations related to the integration of the new transient heat exchanger model and the mission-integrated synthesis/design optimization of the generic INVENT tip-to-tail model. They are as follow:

1. The INVENT tip-to-tail model utilized in this thesis work is generic in nature. As such, any data used to supplement subsystem models is also generic in nature and does not describe any particular aircraft or aircraft subsystem. It is anticipated that the generic INVENT tip-to-tail model, in the future, will be augmented to more accurately reflect an extant aircraft and, at that point, will be set up for use in actual design trade studies and optimization. It is recommended that significant emphasis be placed on individually validating subsystem models with hardware, as well as further supplementing models with experimental data before these trade studies and optimizations are performed. This work is intended purely as a proof of concept, demonstrating that such optimizations are possible and, in addition, are valuable.
2. The integration of the new transient heat exchanger models into the generic INVENT tip-to-tail model allowed the latter to meet all of its performance requirements. This result is significant in that it provides to the INVENT program a significantly more realistic model with which to perform further studies.
3. Performing individual heat exchanger optimizations shows that there are only three important design parameters (s_1, s_2, and L where s is the fin channel width and L is the overall heat exchanger length). However, as described in Chapter 3, the heat exchanger sizing algorithm uses fixed fin efficiency. Thus, no penalty in heat transfer performance is incurred for making fins thinner since thin fins equate to lower mass. Thus, in the heat exchanger mass minimization problem, fin thickness, t_f, converges to the lower bound. Further work is recommended to increase the fidelity of the heat exchanger sizing algorithm by including variable fin efficiency. It would be expected that this would cause several of the fin parameters (i.e., fin height, h, and fin thickness, t_f) to become important design parameters in the optimization problem.

4. Due to the limited data available with regard to the performance of the OSF compact heat exchangers, validation of the heat exchanger model was limited to comparing the temperature profile of the fluids across the heat exchanger to profiles for counter-flow heat exchangers found in the literature. It would be valuable to compare the performance of the heat exchanger model with results from a real heat exchanger of similar characteristics. Additionally, it is recommended that the model be more rigorously validated by comparing results obtained from the model with analytic and empirical models found in the literature.
5. The mission-integrated synthesis/design optimization of the generic INVENT tip-to-tail model produced only small improvements in the fuel consumption and exergy destruction of the vehicle since the APTMS and FTMS subsystems contribute very little to the overall exergy destruction of the vehicle. Thus, it is expected that expanding the optimization problem to include DOF from the PS and AVS subsystems will allow the optimizer to reach a significantly better solution.
6. The exclusion of any operational decision variables from the optimization is due to the fact that within the generic INVENT tip-to-tail model, all operational parameters are determined by subsystem controllers. These controllers are simple proportional-integral (PI) or proportional (P) controllers. These controllers are critical in maintaining adequate flight performance and model stability and, as such, further work is recommended on enhancing the fidelity of the controllers by including them (e.g., their gains) as well as certain operational parameters as decision variables in the optimization.
7. The difficulty in optimizing the generic INVENT tip-to-tail model proved to be overcoming the lengthy simulation time and working with a limited set of computational resources. The average simulation time during the mission-integrated synthesis/design optimization of the generic INVENT tip-to-tail model was approximately 19 min. While it is expected that more robust subsystem controllers would significantly reduce this, expanding the optimization problem is not feasible unless the optimizer has access to a more efficient set of computational resources. Ideally, future optimizations of the tip-to-tail model will be performed on a cluster that allows massive parallelization of the optimizer.
8. The current version of the generic INVENT tip-to-tail model (V_H_3) excludes any high-fidelity electrical models, i.e., the REPS and HPEAS. While it is expected that including

these in the tip-to-tail model would significantly increase simulation time, exergy analyses of a tip-to-tail that includes these subsystems would still be valuable.

9. It is shown that an optimization problem formulated to minimize fuel consumption yields the same results as an optimization problem formulated to minimize exergy destruction provided no AVS DOF are present. However, since exergy analysis has the additional benefit of providing the location and magnitudes of all internal system losses, exergy destruction as a common metric is a useful addition to any optimization. In the case when there are AVS DOF, its direct minimization may also prove to be a superior objective.

Appendix A: Total Vehicle Exergy Balance Derivation to Accommodate Arbitrary Reference Conditions

Given the following identity originally presented by Riggins, i.e.,

$$\dot{m}_f H^* = \dot{m}_f \left\{ h_{0(f)} + \int_{T_{ref}}^{T_f} C_{p(f)}(T')dT' \right\} - T_i \dot{S}_{fuel} - \dot{m}_w \sum_{l=1}^{NS} \alpha_{l,w} \left[h_{l,w} - T_i s_{l,i\backslash w}(T_i, P_i, y_{lw}) \right] + \dot{m}_i \sum_{l=1}^{NS} \alpha_{l,i} \left[h_{l,i} - T_i s_{l,i}(T_i, P_i, y_{li}) \right] \quad \text{(A-1)}$$

it is converted from a mass to a molar basis yielding

$$\dot{n}_f H^* = \dot{n}_f \left\{ h_{0(f)} + \int_{T_{ref}}^{T_f} C_{p(f)}(T')dT' \right\} - T_i \dot{S}_{fuel} - \dot{n}_w \sum_{l=1}^{NS} y_{l,w} \left[h_{l,w} - T_i s_{l,i\backslash w}(T_i, P_i, y_{lw}) \right] + \dot{n}_i \sum_{l=1}^{NS} y_{l,i} \left[h_{l,i} - T_i s_{l,i}(T_i, P_i, y_{li}) \right] \quad \text{(A-2)}$$

Noting that for the fuel,

$$h_{fuel} = h_{0(f)} + \int_{T_{ref}}^{T_f} c_{p(f)_i}(T')dT' \quad \text{(A-3)}$$

equation (A-2) can be rewritten as

$$\dot{n}_f H^* = \dot{n}_f \left(h_{fuel} - T_i s_{fuel} \right) - \dot{n}_w \sum_{l=1}^{NS} y_{l,w} \left[h_{l,w} - T_i s_{l,i\backslash w}(T_i, P_i, y_{lw}) \right] + \dot{n}_i \sum_{l=1}^{NS} y_{l,i} \left[h_{l,i} - T_i s_{l,i}(T_i, P_i, y_{li}) \right] \quad \text{(A-4)}$$

Now, the Gibbs relation for a simple system is given by

$$du = Tds - pdv . \quad \text{(A-5)}$$

From the definition of enthalpy, *h*, one finds that

$$u = h - pv . \quad \text{(A-6)}$$

Taking the total derivative of internal energy, *u*, yields

$$du = dh - pdv - vdp \tag{A-7}$$

Substituting the Gibbs relation results in

$$dh = Tds + vdP \tag{A-8}$$

Integrating this expression gives

$$h - h_{ref} = \int_{s_{ref}}^{s} Tds + v\left(P - P_{ref}\right) \tag{A-9}$$

For an incompressible liquid, the Mayer relation states:

$$c_p = c_v + \frac{T\alpha_p^2 \upsilon}{\kappa_T} \approx c_v \tag{A-10}$$

Furthermore knowing that

$$c_v = T\left(\frac{\partial s}{\partial T}\right)_{V,n} \tag{A-11}$$

one arrives at the following for an incompressible liquid

$$ds = \frac{c_v}{T}\,dT \approx \frac{c_p}{T}\,dT \tag{A-12}$$

Thus, equations (A-9) and (A-10) are rewritten as

$$h - h_{ref} = \int_{T_{ref}}^{T} c_p(T')dT' + v\left(P - P_{ref}\right) \tag{A-13}$$

$$h_{fuel} - h_{0(f)} = \int_{T_{ref}}^{T_f} c_{p(f)_i}(T')dT' + v\left(P_f - P_{ref}\right) \tag{A-14}$$

Assuming $v\left(P_f - P_{ref}\right)$ to be insignificant, the latter equation reduces to

$$\boxed{h_{fuel} = h_{0(f)} + \int_{T_{ref}}^{T_f} c_{p(f)_i}(T')dT'} \tag{A-15}$$

Making the following substitutions into (A-2):

$$
\begin{aligned}
h_{l,w} &= h_{l,w} - h_{ll}^{0}(T_i) + h_{ll}^{0}(T_i) \\
s_{l,w} &= s_{l,w} - s_{ll}^{0}(T_i) + s_{ll}^{0}(T_i) \\
h_{l,i} &= h_{l,i} - h_{ll}^{0}(T_i) + h_{ll}^{0}(T_i) \\
s_{l,i} &= s_{l,i} - s_{ll}^{0}(T_i) + s_{ll}^{0}(T_i) \\
h_{fuel} &= h_{fuel} - h_{fuel}^{0}(T_i) + h_{fuel}^{0}(T_i) \\
s_{fuel} &= s_{fuel} - s_{fuel}^{0}(T_i) + s_{fuel}^{0}(T_i)
\end{aligned}
\qquad \text{(A-16) though (A-21)}
$$

Yields a new expression for equation (A-2), namely,

$$
\begin{aligned}
\dot{n}_f H^* = {} & \dot{n}_f \left(\left(h_{fuel} - h_{fuel}^{0}(T_i) + h_{fuel}^{0}(T_i) \right) - T_i \left(s_{fuel} - s_{fuel}^{0}(T_i) + s_{fuel}^{0}(T_i) \right) \right) \\
& - \dot{n}_w \sum_{l=1}^{NS} y_{l,w} \left[\left(h_{l,w} - h_{ll}^{0}(T_i) + h_{ll}^{0}(T_i) \right) - T_i \left(s_{l,w} - s_{ll}^{0}(T_i) + s_{ll}^{0}(T_i) \right) \right] \\
& + \dot{n}_i \sum_{l=1}^{NS} y_{l,i} \left[\left(h_{l,i} - h_{ll}^{0}(T_i) + h_{ll}^{0}(T_i) \right) - T_i \left(s_{l,i} - s_{ll}^{0}(T_i) + s_{ll}^{0}(T_i) \right) \right]
\end{aligned}
\qquad \text{(A-22)}
$$

Grouping terms yields

$$
\begin{aligned}
\dot{n}_f H^* = {} & \dot{m}_f \left(\left(h_{fuel} - h_{fuel}^{0}(T_i) \right) - T_i \left(s_{fuel} - s_{fuel}^{0}(T_i) \right) \right) \\
& - \dot{n}_w \sum_{l=1}^{NS} y_{l,w} \left[\left(h_{l,w} - h_{ll}^{0}(T_i) \right) - T_i \left(s_{l,w} - s_{ll}^{0}(T_i) \right) \right] \\
& + \dot{n}_i \sum_{l=1}^{NS} y_{l,i} \left[\left(h_{l,i} - h_{ll}^{0}(T_i) \right) - T_i \left(s_{l,i} - s_{ll}^{0}(T_i) \right) \right] \\
& + \left\{ \begin{array}{l}
\dot{n}_f \left(h_{fuel}^{0}(T_i) - T_i s_{fuel}^{0}(T_i) \right) \\
- \dot{n}_w \sum_{l=1}^{NS} y_{l,w} \left[h_{ll}^{0}(T_i) - T_i s_{ll}^{0}(T_i) \right] \\
+ \dot{n}_i \sum_{l=1}^{NS} y_{l,i} \left[h_{ll}^{0}(T_i) - T_i s_{ll}^{0}(T_i) \right]
\end{array} \right\}
\end{aligned}
\qquad \text{(A-23)}
$$

Assuming that the fuel (e.g., JP-8) behaves as an incompressible liquid, the specific entropy difference can be written as

$$s_{fuel} - s_{ref} = \int_{T_{ref}}^{T_f} \frac{c_{p(f)}(T')}{T'} dT' \tag{A-24}$$

At standard conditions, this difference is written as

$$s_f^0(T_0) - s_{ref} = \int_{T_{ref}}^{T_0} \frac{c_{p(f)}(T')}{T'} dT' \tag{A-25}$$

Taking the difference between these last two expressions results in

$$\boxed{s_{fuel} - s_f^0(T_0) = \int_{T_0}^{T_f} \frac{c_{p(f)}(T')}{T'} dT'} \tag{A-26}$$

A similar development for the specific enthalpy difference yields

$$h_{fuel} - h_{ref} = \int_{T_{ref}}^{T_i} c_{p(f)}(T) dT + v(P_i - P_{ref}) \tag{A-27}$$

$$h_f^0(T_0) - h_{ref} = \int_{T_{ref}}^{T_0} c_{p(f)}(T) dT + v(P_0 - P_{ref}) \tag{A-28}$$

$$h_{fuel} - h_f^0(T_0) = \int_{T_0}^{T_i} c_{p(f)}(T) dT + v(P_i - P_0) \tag{A-29}$$

Assuming that $v(P_0 - P_{ref})$ is insignificant gives

$$\boxed{h_{fuel} - h_f^0(T_0) = \int_{T_0}^{T_f} c_{p(f)}(T) dT} \tag{A-30}$$

Now, for air and products of combustion, ideal gas behavior is assumed. The result is that for the partial entropy difference of each constituent,

$$ds = \frac{c_{p,i}(T)}{T} dT - \frac{R}{P} dP \tag{A-31}$$

$$s_l - s_{ref} = \int_{T_{ref}}^{T_l} \frac{c_{p,l}(T')}{T'} dT' - R \ln\left(\frac{P_l}{P_{ref}}\right) \tag{A-32}$$

$$s_{ll}^{0}(T_0) - s_{ref} = \int_{T_{ref}}^{T_0} \frac{c_{p,l}(T')}{T'} dT' - R\ln\left(\frac{P_0}{P_{ref}}\right) \tag{A-33}$$

$$s_l - s_{ll}^{0}(T_0) = \int_{T_0}^{T_l} \frac{c_{p,l}(T')}{T'} dT' - R\ln\left(\frac{P_{ll}}{P_0}\right) \tag{A-34}$$

and

$$\boxed{s_l - s_{ll}^{0}(T_0) = \int_{T_0}^{T_i} \frac{c_{p,l}(T')}{T'} dT' - R\ln\left(\frac{P}{P_0}\right) - R\ln(y_l)} \tag{A-35}$$

For the partial enthalpy difference of each constituent, the results is

$$dh = c_{p,i}(T)dT \tag{A-36}$$

$$h_l - h_{ref} = \int_{T_{ref}}^{T_i} c_{p,l}(T')dT' \; h_{ll}^{0}(T_0) - h_{ref} = \int_{T_{ref}}^{T_0} c_{p,l}(T')dT' \tag{A-37}$$

and

$$\boxed{h_l - h_{ll}^{0}(T_0) = \int_{T_0}^{T_i} c_{p,l}(T')dT'} \tag{A-38}$$

Substituting these last relations into (A-2) yields

$$\begin{aligned}
\dot{n}_f H^* = {} & \dot{n}_f \left(\int_{T_0}^{T_f} c_{p(f)}(T)dT - T_i \int_{T_0}^{T_f} \frac{c_{p(f)}(T')}{T'} dT' \right) \\
& - \dot{n}_w \sum_{l=1}^{NS} y_{l,w} \left[\int_{T_0}^{T_i} c_{p,l,w}(T')dT' - T_i \left(\int_{T_0}^{T_i} \frac{c_{p,l,w}(T')}{T'} dT' - R\,ln\left(\frac{P_w}{P_0}\right) - R\,ln(y_{l,w}) \right) \right] \\
& + \dot{n}_i \sum_{l=1}^{NS} y_{l,i} \left[\int_{T_0}^{T_i} c_{p,l,i}(T')dT' - T_i \left(\int_{T_0}^{T_i} \frac{c_{p,l,i}(T')}{T'} dT' - R\,ln\left(\frac{P_i}{P_0}\right) - R\,ln(y_{l,i}) \right) \right] \\
& + \left\{ \dot{n}_f h_{fuel}^{0}(T_0) - \dot{n}_f T_i s_{fuel}^{0}(T_0) - \dot{n}_w \sum_{l=1}^{NS} y_{lw} h_{ll}^{0}(T_0) \right. \\
& \left. + \dot{n}_w \sum_{l=1}^{NS} y_{lw} T_i s_{ll}^{0}(T_0) + \dot{n}_i \sum_{l=1}^{NS} y_{li} h_{ll}^{0}(T_0) - \dot{n}_i \sum_{l=1}^{NS} y_{li} T_i s_{ll}^{0}(T_0) \right\}
\end{aligned} \tag{A-39}$$

Working with the last set curled brackets only, we write them as

$$A \equiv \dot{n}_{f\,f} h^0_{fuel}(T_i) - \dot{n}_{f\,f} T_i s^0_{fuel}(T_i) + \sum_{l=1}^{NS} \left(\dot{n}_{f\,l,i} - \dot{n}_{f\,l,w}\right) h^0_{ll}(T_i) - \sum_{l=1}^{NS} \left(\dot{n}_{f\,l,i} - \dot{n}_{f\,l,w}\right) T_i s^0_{ll}(T_i) \tag{A-40}$$

Including terms for fuel within the summation gives

$$A \equiv \sum_{l=1}^{NS} \left(\dot{n}_{l,i} - \dot{n}_{l,w}\right) h^0_{ll}(T_i) - \sum_{l=1}^{NS} \left(\dot{n}_{l,i} - \dot{n}_{l,w}\right) T_i s^0_{ll}(T_i) \tag{A-41}$$

Noting that from the proportionality relations

$$\dot{n}_{l,i} - \dot{n}_{l,w} = -\nu_l \dot{\varepsilon} \tag{A-42}$$

A becomes

$$A \equiv \sum_{l=1}^{NS} \left(-\nu_l \dot{\varepsilon}\right) h^0_{ll}(T_i) - \sum_{l=1}^{NS} \left(-\nu_l \dot{\varepsilon}\right) T_i s^0_{ll}(T_i) \tag{A-43}$$

This last expression assumes complete combustion (i.e., ε = 1). However, if the reaction coordinate for incomplete combustion is known, the equation could easily be altered to account for this case as well.

Now, since the reaction coordinate on a rate basis is needed, the following is done:

$$\frac{\varepsilon}{\dot{\varepsilon}} = \frac{n_l}{\dot{n}_l} = t, \quad \varepsilon = 1 \quad \Rightarrow \quad \dot{\varepsilon} = \frac{1}{t} \tag{A-44}$$

Substituting into (A-44), yields

$$A \equiv \frac{1}{t} \sum_{l=1}^{NS} \left(-\nu_l\right) h^0_{ll}(T_i) - \frac{1}{t} \sum_{l=1}^{NS} \left(-\nu_l\right) T_i s^0_{ll}(T_i) \tag{A-45}$$

$$A \equiv -\frac{1}{t} \sum_{l=1}^{NS} \nu_l h^0_{ll}(T_i) + \frac{1}{t} \sum_{l=1}^{NS} \nu_l T_i s^0_{ll}(T_i) = -\frac{1}{t} \left(\Delta h^0(T_i) - T_i \Delta s^0(T_i)\right) \tag{A-46}$$

where the Hess relations for the enthalpy and entropy of reaction have been used. Writing the enthalpy and entropy of reaction in terms of the standard enthalpy and entropy of reaction transforms equation (A-47) into

$$A \equiv -\frac{1}{t} \left[\left(\Delta h^0(T_0) + \sum_{l=1}^{NS} \nu_l \left[h^0_{ll}(T_i) - h^0_{ll}(T_0) \right] \right) - T_i \left(\Delta s^0(T_0) + \sum_{l=1}^{NS} \nu_l \left[s^0_{ll}(T_i) - s^0_{ll}(T_0) \right] \right) \right] \tag{A-47}$$

or

$$A \equiv -\frac{1}{t}\left[\Delta h^0(T_0) - T_i \Delta s^0(T_0) + \left(\sum_{l=1}^{NS} \nu_l \left[h_{ll}^0(T_i) - h_{ll}^0(T_0)\right]\right) - T_i\left(\sum_{l=1}^{NS} \nu_l \left[s_{ll}^0(T_i) - s_{ll}^0(T_0)\right]\right)\right] \tag{A-48}$$

Now, substituting the Gibbs free energy of raction for the enthalpy and entropy of reaction as well as the Hess relation relating the Gibbs free energy of reaction to the Gibbs free energies of formation results in

$$A \equiv -\frac{1}{t}\left[\Delta g^0(T_0) + \left(\sum_{l=1}^{NS} \nu_l \left[\int_{T_0}^{T_i} c_{p,l}(T')dT'\right]\right) - T_i\left(\sum_{l=1}^{NS} \nu_l \left[\int_{T_0}^{T_i} \frac{c_{p,l}(T')}{T'} dT'\right]\right)\right] \tag{A-49}$$

and

$$A \equiv -\frac{1}{t}\left[\sum_{l=1}^{NS} \nu_l \left(\Delta g_f^0\right)_l + \left(\sum_{l=1}^{NS} \nu_l \left[\int_{T_0}^{T_i} c_{p,l}(T')dT'\right]\right) - T_i\left(\sum_{l=1}^{NS} \nu_l \left[\int_{T_0}^{T_i} \frac{c_{p,l}(T')}{T'} dT'\right]\right)\right] \tag{A-50}$$

Finally, inserting *A* into (A-40) yields the final results, namely,

$$\begin{aligned}
\dot{n}_f H^* = {} & \dot{n}_f \left(\int_{T_0}^{T_f} c_{p(f)}(T)dT - T_i \int_{T_0}^{T_f} \frac{c_{p(f)}(T')}{T'} dT'\right) \\
& - \dot{n}_w \sum_{l=1}^{NS} y_{l,w}\left[\int_{T_0}^{T_i} c_{p,l,w}(T')dT' - T_i\left(\int_{T_0}^{T_i} \frac{c_{p,l,w}(T')}{T'} dT' - R\ln\left(\frac{P_w}{P_0}\right) - R\ln\left(y_{l,w}\right)\right)\right] \\
& + \dot{n}_i \sum_{l=1}^{NS} y_{l,i}\left[\int_{T_0}^{T_i} c_{p,l,i}(T')dT' - T_i\left(\int_{T_0}^{T_i} \frac{c_{p,l,i}(T')}{T'} dT' - R\ln\left(\frac{P_i}{P_0}\right) - R\ln\left(y_{l,i}\right)\right)\right] \\
& + -\frac{1}{t}\left[\sum_{l=1}^{NS} \nu_l \left(\Delta g_f^0\right)_l + \left(\sum_{l=1}^{NS} \nu_l \left[\int_{T_0}^{T_i} c_{p,l}(T')dT'\right]\right) - T_i\left(\sum_{l=1}^{NS} \nu_l \left[\int_{T_0}^{T_i} \frac{c_{p,l}(T')}{T'} dT'\right]\right)\right]
\end{aligned} \tag{A-51}$$

Appendix B: Heat Exchanger Sizing Algorithm

```
function [parameter] = HXsize_v12(params,fluids,params2,mat)

%This function, written by Peter Weise, determines the mass and pressure
%drop of a compact heat exchanger based on its physical parameters and
%heat transfer characteristics.

% Heat exchanger fixed parameters:  The following parameters need to be
% fixed for a given optimization trial.  However, they can be varied.
% For example, the heat load varies from one heat exchanger to another.
% Additionally, the fluids vary from one exchanger to another.

s1 = params(1)/1000;
h1 = params(2)/1000;
l1 = params(3)/1000;
tf1 = params(4)/1000;
t1 = params(5)/1000;
s2 = params(6)/1000;
h2 = params(7)/1000;
l2 = params(8)/1000;
tf2 = params(9)/1000;
t2 = params(10)/1000;
L = params (11);

fluid1 = fluids.ctype;
fluid2 = fluids.htype;

m_dot1 = params2(1);      %(kg/s) flow rate
m_dot2 = params2(2);      %(kg/s) flow rate
T_in1 = params2(3);       %(K) inlet temperature. In the actual T2T model,
the inlet temperature will be based on downstream conditions and accepted as
an input.
T_in2 = params2(4);       %(K) inlet temperature. See note above
Q_dot = params2(5);       %(kW) heat load

eta = 0.7;                %(N) fin efficiency

b1=h1+tf1;
b2=h2+tf2;
%% Material density,
material = mat;
%rho_m = (kg/m^3) material density
switch material
    case {'Stainless steel - 316'}
        rho_m = 8027;
    case {'Aluminum'}
        rho_m = 2707;
    case {'Copper'}
        rho_m = 8954;
end
```

```
%%  Solves for the properties of each fluid based on inlet temperatures,
steady state outlet temperatures and fluid property correlations.
    [f1.cp, f1.rho, f1.k, f1.mu, f1.muT] = fluidproperties(fluid1);
    [f2.cp, f2.rho, f2.k, f2.mu, f2.muT] = fluidproperties(fluid2);

    %%% Specific heat
    cp1 = polyval(f1.cp,T_in1);
    cp2 = polyval(f2.cp,T_in2);

    %%% Density
    rho1 = polyval(f1.rho,T_in1);
    rho2 = polyval(f2.rho,T_in2);

    %%% Thermal Conductivity
    k1 = polyval(f1.k,T_in1);
    k2 = polyval(f2.k,T_in2);

    %%% Approximate outlet temperature
    T_out1 = T_in1 + Q_dot/(m_dot1*cp1);
    T_out2 = T_in2 - Q_dot/(m_dot2*cp2);

    %%% Dynamic Viscocity
    mu1 = interp1(f1.muT,f1.mu,(T_in1+T_out1)/2);
    mu2 = interp1(f2.muT,f2.mu,(T_in2+T_out2)/2);

 %%  Calculate important heat exchanger physical parameters
    parameter.dh1=(4*s1*h1*l1)/(2*(s1*l1+h1*l1+tf1*h1)+tf1*s1);
    parameter.dh2=(4*s2*h2*l2)/(2*(s2*l2+h2*l2+tf2*h2)+tf2*s2);

    sigma1=s1*(b1-tf1)/(s1+tf1)/(b1+t1);    %porosity of side 1
    sigma2=s2*(b2-tf2)/(s2+tf2)/(b2+t2);    %porosity of side 2

    alpha1=s1/h1;  %various aspect ratios used in calculating j and f
    delta1=tf1/l1;
    gamma1=tf1/s1;

    alpha2=s2/h2;
    delta2=tf2/l2;
    gamma2=tf2/s2;

    %%% Initialize Ac1 and Ac2.  Correct values will be solved for in an
    %%% iterative process.

    parameter.Ac1 = 0.01;
    parameter.Ac2 = 0.01;
    difference1 = inf;
    difference2= inf;
    count = 0;

    %% This iterative while loop solves for Ac1 and Ac2.
    while count<=100 && abs(difference1)>=1e-5  && abs(difference2)>=1e-5
```

```
        %%% parameter.Reynolds' number
        Re1=m_dot1*parameter.dh1/mu1/parameter.Ac1;
        Re2=m_dot2*parameter.dh2/mu2/parameter.Ac2;

        %%% Fanning friction factor
        parameter.f1=9.6243*(Re1^-0.7422)*(alpha1^-
0.1856)*(delta1^0.3053)*(gamma1^-0.2659)*((1+7.669E-
8*(Re1^4.429)*(alpha1^0.92)*(delta1^3.767)*(gamma1^0.236))^0.1);
        parameter.f2=9.6243*(Re2^-0.7422)*(alpha2^-
0.1856)*(delta2^0.3053)*(gamma2^-0.2659)*((1+7.669E-
8*(Re2^4.429)*(alpha2^0.92)*(delta2^3.767)*(gamma2^0.236))^0.1);

        %%% Colburn coefficient
        j1=0.6522*(Re1^-0.5403)*(alpha1^-0.1541)*(delta1^-0.1409)*(gamma1^-
0.0678)*((1+5.269E-5*(Re1^1.34)*(alpha1^0.504)*(delta1^0.456)*(gamma1^-
1.055))^0.1);
        j2=0.6522*(Re2^-0.5403)*(alpha2^-0.1541)*(delta2^-0.1409)*(gamma2^-
0.0678)*((1+5.269E-5*(Re2^1.34)*(alpha2^0.504)*(delta2^0.456)*(gamma2^-
1.055))^0.1);

        %%% Effectiveness-Ntu method
        T_h1=max(T_in1,T_in2);
        T_c1=min(T_in1,T_in2);
        Cmax=max(m_dot1*cp1,m_dot2*cp2);
        Cmin=min(m_dot1*cp1,m_dot2*cp2);
        Cstar=Cmin/Cmax;
        epsilon = Q_dot/(Cmin*(T_h1-T_c1));

        if 0.99<=Cstar<=1.01
            Ntu=epsilon/(1-epsilon);
        else
            Ntu=Log((epsilon-1)/(Cstar*epsilon-1))/(Cstar-1);
        end

        N=2*Ntu/eta;

        %%% Pressure drop
        parameter.del_P1=…
            ((m_dot1/parameter.Ac1)^2)*4*L*parameter.f1/2/rho1/parameter.dh1;
        parameter.del_P2=…
            ((m_dot2/parameter.Ac2)^2)*4*L*parameter.f2/2/rho2/parameter.dh2;

        %%% Prandtl number
        Pr1=cp1*mu1/k1*1000;
        Pr2=cp2*mu2/k2*1000;

        %%% Flow velocity
        G1=sqrt(2*rho1*parameter.del_P1*j1/parameter.f1/(Pr1^(2/3))/N);
        G2=sqrt(2*rho2*parameter.del_P2*j2/parameter.f2/(Pr2^(2/3))/N);

        %%% Flow area
        Ac1_0=m_dot1/G1;
        Ac2_0=m_dot2/G2;
```

```
        difference1=parameter.Ac1-Ac1_0;
        difference2=parameter.Ac2-Ac2_0;

        parameter.Ac1=Ac1_0;
        parameter.Ac2=Ac2_0;

        count = count + 1;
    end

%%% Calculate volume and mass
    parameter.mass_kg=rho_m*L*(parameter.Ac1/sigma1*(1-…
       sigma1)+parameter.Ac2/sigma2*(1-sigma2));
    parameter.mass_f1 = (parameter.Ac1*rho1*L);
    parameter.mass_f2 = parameter.Ac2*rho2*L;
    parameter.vol_HX = L*(parameter.Ac1/sigma1*(1-…
       sigma1)+parameter.Ac2/sigma2*(1-sigma2));
    parameter.vol_f = (parameter.Ac1+parameter.Ac2)*L;
    Beta = [4*sigma1/parameter.dh1 4*sigma2/parameter.dh2];
    parameter.vol1 = L*parameter.Ac1;
    parameter.vol2 = L*parameter.Ac2;
    parameter.As1 =Beta(1) * (L*(parameter.Ac1/sigma1*(1-sigma1)) +
parameter.Ac1);
    parameter.As2 =Beta(2) * (L*(parameter.Ac2/sigma2*(1-sigma2)) +
parameter.Ac2);
    parameter.L = L;

%%% Additional outputs,
    parameter.ratios1 = [alpha1 delta1 gamma1];
    parameter.ratios2 = [alpha2 delta2 gamma2];
    parameter.Achx = (sqrt(parameter.Ac1)+sqrt(parameter.Ac2))/2*parameter.L;
    parameter.Aht1 = parameter.Ac1*(s1 + tf1)/(s1*h1)*L;
    parameter.Aht2 = parameter.Ac2*(s2 + tf2)/(s2*h2)*L;
```

References

1. Cloyd, J., *Status of the United States Air Force's More Electric Aircraft Initiative*, IEEE AES Systems Magazine, April 1998.
2. Gandolfi, R., Pellegrini, L. F., de Olviera Jr., S., 2010, *More Electric Aircraft Analysis Using Exergy as a Design Comparison Tool*, 48th AIAA Aerospace Sciences Meeting, paper no. AIAA 2010-809, Orlando, FL, Jan. 4-7.
3. Roberts, R., Eastbourn, S., Maser, A., *General Aircraft Thermal Tip-to-Tail Modeling and Simulation*, 2011, 47th AIAA/ASME/SAE/ASEE Joint Propulsion Conference and Exhibit, San Diego, CA, Jul. 21-Aug. 3. AIAA 2011-5971.
4. Gvozdich, G., *Modeling the Effects of Transient High Energy Weapon Subsystems on High-performance Aerospace Systems*, M.S. Thesis, adviser: M. R. von Spakovsky, Department of Mechanical Engineering, Virginia Tech, Blacksburg, Virginia, 2011.
5. Walia, P., Canto, G., Roe, G., Erdman, T., *Integrated Vehicle and Energy Technology (INVENT) Modeling Requirements and Implementation Plan (MRIP)*, 15 March 2010, v3.1, Case Number 88ABW-2010-1758; Distribution A.
6. Walters, E. A. and Iden, S., 2010, *INVENT Modeling, Simulation, Analysis and Optimization*, 48th AIAA Aerospace Sciences Meeting, Orlando, Fl, 2010.
7. Eastbourn, S. M., *Modeling and Simulation of a Dynamic Turbofan Engine Using Matlab/Simulink*, M.S. Thesis, adviser: R. Roberts, Department of Engineering, Wright State University, Dayton, Ohio, 2012.
8. Bodie, M., Russell, G., McCarthy, K., Lucus, E., Zumberge, J., Wolff, M., 2010, *Thermal Analysis of an Integrated Aircraft Model*, 48th AIAA Aerospace Sciences Meeting, paper no. AIAA 2010-288 Orlando, FL, Jan 4-7.
9. Gyftopoulos, E. P., Beretta, G. P., Thermodynamics: Foundations and Applications, (2^{nd} ed.), Dover Publications, Mineola, New York, 2005.
10. Muñoz, J. R., *Optimization Strategies for the Synthesis / Design of Highly Coupled, Highly Dynamic Energy Systems*, Ph. D. Dissertation, adviser: M. R. von Spakovsky, Department of Mechanical Engineering, Virginia Tech, Blacksburg, Virginia, 2000.

11. Muñoz, J.R., von Spakovsky, M.R., 2003, *Decomposition in Energy System Synthesis /Design Optimization for Stationary and Aerospace Applications*, AIAA Journal of Aircraft, special issue, Vol. 40, No. 1, pp. 35-42.
12. Muñoz, J.R., von Spakovsky, M.R., 2001, *The Application of Decomposition to the Large Scale Synthesis/Design Optimization of Aircraft Energy Systems*, International Journal of Applied Thermodynamics, June, vol. 4, no.2.
13. Muñoz, J.R., von Spakovsky, M.R., 2001, *A Decomposition Approach for the Large Scale Synthesis/Design Optimization of Highly Coupled, Highly Dynamic Energy Systems*, International Journal of Applied Thermodynamics, March, vol. 4, no. 1.
14. von Spakovsky, M. R., 2011, *Chapter 9 - Mission-Integrated Synthesis and Design Optimization (MIS/DO) of Aerospace Vehicles*, Exergy Analysis and Design Optimization for Aerospace Vehicles and Systems, editors: Camberos J. and Moorhouse D., AIAA book series.
15. von Spakovsky, M. R., 2011, *Chapter 10 - MIS/DO Applied to High Performance Aerospace Vehicles*, Exergy Analysis and Design Optimization for Aerospace Vehicles and Systems, editors: Camberos J. and Moorhouse D., AIAA book series.
16. Sobieszczanski-Sobieski, J, *Optimization by Decomposition: A step from Hierarchic to Non-hierarchic Systems*, NASA CP-3031, Part 1, 1989.
17. Sobieszczanski-Sobieski, J, 1990, *Sensitivity of Complex, Internally Coupled Systems*, AIAA Journal, Vol. 28, pp.153-161.
18. Mattingly, J. D., Heiser,W.H. and Daley, D.H., 1987, Aircraft Engine Design, AIAA Education Series, New York, New York.
19. Mattingly, J. D., 1996, Elements of Propulsion, AIAA Education Series, New York, New York.
20. Rancruel, D. F., *A Decomposition Strategy Based on Thermoeconomic Isolation Applied to the Optimal Synthesis/Design and Operation of an Advanced Fighter Aircraft System*, M.S. Thesis: adviser: M. R. von Spakovsky, Department of Mechanical Engineering, Virginia Polytechnic Institute and State University, Blacksburg, VA, 2003.

21. Rancruel, D. F., von Spakovsky, M. R., 2006, A Decomposition Strategy based on Thermoeconomic Isolation Applied to the Optimal Synthesis/Design and Operation of an Advanced Tactical Aircraft System, Energy: The International Journal, Elsevier, available on-line at http://dx.doi.org/10.1016/j.energy.2006.03.004, vol. 31, no. 15, December, p 3327-3341.

22. Rancruel, D. F., von Spakovsky, M. R., 2003, *Decomposition with Thermoeconomic Isolation Applied to the Optimal Synthesis/Design of an Advanced Fighter Aircraft System*, International Journal of Thermodynamics, ICAT, Istanbul, Turkey, September, vol. 6, no. 3.

23. Rancruel, D. F., von Spakovsky, M. R., 2004, *Advanced Fighter Aircraft Sub-systems Optimal Synthesis/Design and Operation: Airframe Integration Using a Thermoeconomic Approach*, 10th AIAA/ISSMO Multi-disciplinary Analysis and Optimization Conference, Aug. 30 - Sept. 1, Albany, New York, vol. 6: pp. 3403-3415.

24. Markel, K. C., *Exergy Methods for the Generic Analysis and Optimization of Hypersonic Vehicle Concepts*, M.S. Thesis, adviser: M. R. von Spakovsky, Department of Mechanical Engineering, Virginia Tech, Blacksburg, VA, 2005.

25. Brewer, K. M., *Exergy Methods for the Mission-Level Analysis and Optimization of Generic Hypersonic Vehicles*, M.S. Thesis, adviser: M. R. von Spakovsky, Department of Mechanical Engineering, Virginia Polytechnic Institute and State University, Blacksburg, VA, 2006.

26. Markell, K. C., Brewer, K.M., and von Spakovsky, M. R., *Exergy Methods for Mission Level Integrated Analysis and Optimization of Hypersonic Vehicle Concepts*, Summer Research Presentation at Air Force Research Laboratories, Dayton, OH. July 2004.

27. Periannan, V., *Investigation of the Effects of Various Energy and Exergy-Based Objectives/Figures of Merit on the Optimal Design of High Performance Aircraft System*, M.S. Thesis, adviser: M. R. von Spakovsky, Department of Mechanical Engineering, Virginia Tech, Blacksburg, VA, 2005.

28. Periannan, V., von Spakovsky, M.R., Moorhouse, D., 2008, *Energy versus Exergy-Based Figures of Merit for the Optimal Synthesis/Design of High Performance Aircraft Systems*,

The Aeronautical Journal, Royal Aeronautical Society, London, England, vol. 112, no. 1134, pp 449-458.

29. Butt, J. R., *A Study of Morphing Wing Effectiveness in Fighter Aircraft using Exergy Analysis and Global Optimization Techniques*, M.S. Thesis, adviser: M. R. von Spakovsky, Department of Mechanical Engineering, Virginia Tech, Blacksburg, VA, 2005.
30. Moorhouse, D. J., Sanders B., von Spakovsky, M.R., and Butt, J., 2006, *Benefits and Design Challenges of Adaptive Structures for Morphing Aircraft*, The Aeronautical Journal, Royal Aeronautical Society, London, England, vol. 110, no. 1105, March, 2006, p 157-162.
31. Smith, K. W., *Morphing Wing Fighter Aircraft Synthesis/Design Optimization*, M.S. Thesis, adviser: M. R. von Spakovsky, Department of Mechanical Engineering, Virginia Tech, Blacksburg, VA, 2009.
32. Smith, K., Butt, J., von Spakovsky, M. R., Moorhouse, D., 2007, *A Study of the Benefits of Using Morphing Wing Technology in Fighter Aircraft Systems*, 39th AIAA Thermophysics Conference, Miami, FL, June 25-28.
33. Leyland, G.B., 2002, *Multi-Objective Optimization Applied to Industrial Energy Problems*, Department of Mechanical Engineering, University of Auckland, doctoral thesis.
34. Anderson, J. D., 1984, Aircraft Performance and Design, New York: McGraw-Hill.
35. Riggins, D. W., Moorhouse, D. J., Camberos, J. A., 2011, Exergy Analysis and Design Optimization for Aerospace Vehicles and Systems: Entropy Generation and Aerospace Vehicle Performance, Progress in Astronautics and Aeronautics, Vol. 238.
36. Gvozdich, G., Weise, P., von Spakovsky, M. R., 2012, *INVENT: Study of Issues Involved in Integrating a Directed Energy Weapon Subsystem into a High Performance Aircraft System*, 50th AIAA Aerospace Science Meeting, paper no. AIAA-1132278, Nashville, TN, Jan. 9-12.
37. Hesselgreves, J. E., 2001, Compact Heat Exchangers: Selection, Design and Operation (1st ed.). Oxford: Elsevier.
38. Kays, W. M., London, A. L., 1998, Compact Heat Exchangers, McGraw-Hill Series in Mechanical Engineering, New York, New York.
39. Shah, R. K., Sekulic, D. P., 2003, Fundamentals of Heat Exchanger Design, John Wiley & Sons, Inc., Hoboken, New Jersey.

40. Kakaç, S., Liu, H., Pramuanjaroenkij, A., 2012, Heat Exchangers: Selection, Rating, and Thermal Design, CRC Press, Boca Raton, Florida.
41. Queipo, N. V., Haftka, R. T., Shyy, W., Goel, T., Vaidyanathan, R., Tucker, P. K., *Surrogate-Based Analysis and Optimization*, Progress in Aerospace Sciences 41 (2005), p. 1-28, Oxford: Elsevier.
42. Gorissen, D., Couckuyt, I., Laermans, E., Dhaene, T., *Multiobjective Global Surrogate Modeling, Dealing With the 5-percent Problem*, Engineering with Computers (2010) 26:81-98.
43. Rowland, T., E. W. Weisstein. Genetic Algorithm. http://mathworld.wolfram.com/GeneticAlgorithm.html (accessed January 2, 2011).
44. Zoutendijk, G., (1960) Methods of Feasible Directions: A Study of Linear and Nonlinear Programming, Elsevier.
45. Cottle, R. W., Pang, J., Stone, R. E., (1992) *The Linear Complementary Problem*. Computer Science and Scientific Computing. Academic Press, Boston, MA.
46. Gorissen, D., Crombecq, K., Couckuyt, I., Dhaene, T., Demeester, P., *A Surrogate Modeling and Adaptive Sampling Toolbox for Computer Based Design*, Journal of Machine Learning Research, Vol. 11, pp. 2051-2055, Jul. 2010.
47. Vetrovec, J., Copeland, D., Du, D., and Schmidt, B., *Ytterbium–Based Disk Amplifier for an Ultra–Short Pulse Laser*, SPIE, vol. 7578, 2010.
48. Manglik, R. M., Bergles, A. E., *Heat Transfer and Pressure Drop Correlations for the Rectangular Offset Strip Fin Compact Heat Exchanger*, Experimental Thermal and Fluid Science, Volume 10, Number 2, pp. 171-180, Feb. 1995.
49. Incropera, F. P., David, D. P., (2000). Fundamentals of Heat and Mass Transfer (4th ed.). John Wiley & Sons, Inc., New York, New York.
50. Gnielinski, V., 1983, *Forced Convection in Ducts, Section 2.5.1*, Heat Exchanger Design Handbook, Hemisphere.
51. Matlab® 2011b Documentation: Optimization Toolbox. 2011. MathWorks. 11 Nov. 2011. <http://www.mathworks.com/help/toolbox/optim/ug/fmincon.html>.

52. Boggs, P. T. and Tolle, J. W., *Sequential Quadratic Programming*, Acta Numerica, Volume 4, pp. 1-51, Jan. 1995.
53. Woodburn, D., "Implementation of Exergy Balance Equations in the Tip-to-Tail Engine Model," AFRL Summer 2012 Final Report.
54. Riggins, D. W., Moorhouse, D. J., Camberos, J. A., *Exergy Analysis and Design Optimization for Aerospace Vehicles and Systems: Entropy Generation and Aerospace Vehicle Performance*, Progress in Astronautics and Aeronautics, Vol. 238, 2011.